ESTIMATION OF FULL MOMENT TENSORS, INCLUDING UNCERTAINTIES, FOR EARTHQUAKES, VOLCANIC EVENTS, AND NUCLEAR EXPLOSIONS

By

Celso R. Alvizuri, M.S.

A Dissertation Submitted in Partial Fulfillment of the Requirements

for the Degree of

Doctor of Philosophy

in

Geophysics

University of Alaska Fairbanks

December 2016

APPROVED:

Dr. Carl Tape, Committee Chair
Dr. Douglas Christensen, Committee Member
Dr. Michael West, Committee Member
Dr. Jeffrey Freymueller, Committee Member
Dr. Paul McCarthy, Chair
Department of Geosciences
Dr. Paul Layer, Dean
College of Natural Science and Mathematics
Dr. Michael Castellini, *Dean of the Graduate School*

Abstract

We present a catalog of full seismic moment tensors for 63 events from Uturuncu volcano in Bolivia. The events were recorded during 2011-2012 in the PLUTONS seismic array of 24 broadband stations. Most events had magnitudes between 0.5 and 2.0 and did not generate discernible surface waves; the largest event was M_w 2.8. For each event we computed the misfit between observed and synthetic waveforms, and we used first-motion polarity measurements to reduce the number of possible solutions. Each moment tensor solution was obtained using a grid search over the six-dimensional space of moment tensors. For each event we show the misfit function in eigenvalue space, represented by a lune. We identify three subsets of the catalog: (1) 6 isotropic events, (2) 5 tensional crack events, and (3) a swarm of 14 events southeast of the volcanic center that appear to be double couples. The occurrence of positively isotropic events is consistent with other published results from volcanic and geothermal regions. Several of these previous results, as well as our results, cannot be interpreted within the context of either an oblique opening crack or a crack-plus-double-couple model. Proper characterization of uncertainties for full moment tensors is critical for distinguishing among physical models of source processes.

A seismic moment tensor is a 3×3 symmetric matrix that provides a compact representation of a seismic source. We develop an algorithm to estimate moment tensors and their uncertainties from observed seismic data. For a given event, the algorithm performs a grid search over the six-dimensional space of moment tensors by generating synthetic waveforms for each moment tensor and then evaluating a misfit function between the observed and synthetic waveforms. 'The' moment tensor M_0 for the event is then the moment tensor with minimum misfit. To describe the uncertainty associated with M_0, we first convert the misfit function to a probability function. The uncertainty, or rather the confidence, is then given by the 'confidence curve' $\mathscr{P}(V)$, where $\mathscr{P}(V)$ is the probability that the true moment tensor for the event lies within the neighborhood of M that has fractional volume V. The area under the confidence curve provides a single, abbreviated 'confidence parameter' for M_0. We apply the method to data from events in different regions and tectonic settings: 63 small ($M_w < 2.5$) events at Uturuncu volcano in Bolivia, 21 moderate ($M_w > 4$) earthquakes in the southern Alaska subduction zone, and 12 earthquakes and 17 nuclear explosions at the Nevada Test Site. Characterization of moment tensor uncertainties puts us in better position to discriminate among moment tensor source types and to assign physical processes to the events.

Table of Contents

Page

List of Figures

Page

Page

Page

List of Tables

Page

List of Appendices

Page

Acknowledgements

This thesis work was supported by a Research Assistantship at the Geophysical Institute and funded by the National Science Foundation (grants EAR-1215959 and EAR-0909254) and the Air Force Research Laboratory (contract FA9453-15-C-0063). Additional support was provided by the Society for Exploration Geophysicists, the College of Natural Science and Mathematics at the University of Alaska Fairbanks, the University of Alaska Fairbanks Graduate School, and the Geophysical Institute Graduate Student Association.

For both papers in Chapter 2 and Chapter 3, co-author Carl Tape contributed significantly to the writing. Vipul Silwal contributed to the development of the moment tensor code used in both papers. Lion Krischer and Matt Gardine supported the accessing and processing of waveforms from the LLNL database (Walter et al., 2006) used in Chapter 3. In Chapter 2, "we" refers to the authors (myself and Carl Tape); in Chapter 3, "we" refers to the authors (myself, Vipul Silwal, Lion Krischer, and Carl Tape).

Chapter 1
Introduction

1.1 General introduction

The seismic moment tensor was first introduced in an article by Gilbert (1970) to calculate the excitation of normal modes in the Earth. That article noted that the response of the Earth to a seismic source can be expressed in terms of normal modes, and in turn the analysis of normal modes can be used to infer the seismic source and its magnitude.

Gilbert (1973) demonstrated the possibility of estimating the moment tensor from amplitudes in long-period wavelengths, then Gilbert & Dziewonski (1975) utilized observations of normal mode amplitudes to estimate the moment tensors for two deep earthquakes in Colombia and Peru-Bolivia. A later study by Dziewonski et al. (1981) presented a numerically efficient method to estimate seismic source parameters, including hypocentral coordinates, from waveform data. This method allowed for imperfect knowledge of an Earth model, and was applicable for earthquakes of magnitudes $M > 5$. These works represent the first discussions of moment tensors and their usefulness to estimate seismic source mechanisms from seismic waveforms.

Nowadays seismic moment tensors are routinely estimated (e.g., Dziewonski et al., 1981; Sipkin, 1982; Kawakatsu, 1995) for seismic events anywhere on Earth, and for a variety of sources, from geothermal and volcanic, to mining, hydraulic fracturing, landslides, glaciers, explosions, and earthquakes (see Alvizuri & Tape (2016) for a comprehensive list and references for these studies). Moment tensors, however, only provide a phenomenological description of the seismic source (Backus & Mulcahy, 1976a,b); they do not provide an explanation of the physical process that generated the source.

The moment tensor elements by themselves are usually not easy to interpret in terms of physical parameters. This observation led Hudson et al. (1989) to develop a way to represent the moment tensor elements in terms of physically identifiable parameters, and where the terms of a seismic source can be described in terms of a combination of physical processes. In this representation, the moment tensor eigenvalues are mapped onto a two-dimensional 'source-type' plot. This source-type plot represents a description of equivalent force system.

Moment tensor uncertainty estimates are a first step towards discussing moment tensors and the seismic source mechanisms that they represent. The work in this thesis deals with three primary goals: (1) develop a method for efficiently estimating seismic full moment tensors, and that utilizes as much as possible from seismic waveform records; (2) develop a method for estimating full moment tensor uncertainties; (3) develop a way to display source-types and their uncertainties on moment tensor space.

1.1.1 The seismic moment tensor

The moment tensor can be thought of as a vector field. A moment tensor M is a 3×3 symmetric matrix that operates on any given point $\mathbf{e}$ and assigns a vector $M(\mathbf{e})$ at that point. The moment tensor has three orthogonal eigenvectors, three associated principal axes aligned along the eigenvectors (though the axes are without direction), and three eigenvalues. In seismology, the vector field from the moment tensor is visualized in terms of a 'beachball', where colored regions typically indicate vectors pointing out from a source origin, and white regions indicate vectors pointing inward toward the source origin. The patterns on the beachball are determined by the eigenvalues of the moment tensor. The orientation of the patterns are determined by the eigenvectors of the moment tensor.

In compact notation, a moment tensor $\mathbf{M}$ can be represented in terms of its eigenvalues $[\Lambda]$ and a rotation matrix U

$$\mathbf{M} = U\,[\Lambda]\,U^{-1} \tag{1.1}$$

where $[\Lambda]$ describes the pattern of the beachball

$$[\Lambda] = \begin{pmatrix} \lambda_1 & 0 & 0 \\ 0 & \lambda_2 & 0 \\ 0 & 0 & \lambda_3 \end{pmatrix} \tag{1.2}$$

and U describes its orientation in space.

1.1.2 A moment tensor parameterization

The elements of the moment tensor can be generated and manipulated directly; they can also be parameterized in terms of other quantities, which can simplify the analysis of moment tensors. The work in this thesis uses the moment tensor parameterization of Tape & Tape (2012). In this parameterization, the eigenvalues of the moment tensor are organized on a section of a sphere, a lune. The set of all beachball patterns on the lune $\mathbb{L}$ can be represented as

$$\mathbb{L} = \{\Lambda \in \mathbb{R}^3 \,|\, \lambda_1 \geq \lambda_2 \geq \lambda_3\} \tag{1.3}$$

A point Λ in $\mathbb{L}$ can be described in terms of its longitude γ and latitude β as $\Lambda(\gamma, \beta)$, where

$$\Lambda = \frac{1}{\sqrt{6}} \begin{pmatrix} \sqrt{3} & -1 & \sqrt{2} \\ 0 & 2 & \sqrt{2} \\ -\sqrt{3} & -1 & \sqrt{2} \end{pmatrix} \cdot (\sin\beta\cos\gamma,\, \sin\beta\sin\gamma,\, \cos\beta)^{\top} \tag{1.4}$$

Equation 1.1 shows that the eigenvalues Λ can be rotated by a matrix U to obtain a moment tensor in any direction. The matrix U is

$$U = VY_{-\pi/4} \tag{1.5}$$

where $Y_{-\pi/4}$ is required to rotate U so that it is directly related to the familiar strike, dip, and slip angles. In turn, V in Equation 1.5 is obtained from the column vectors for slip $\mathbf{S}$, the fault plane normal vector $\mathbf{N}$, and the nodal vector $\mathbf{N} \times \mathbf{S}$, as

$$V = [\mathbf{N}, \mathbf{N} \times \mathbf{S}, \mathbf{S}] \tag{1.6}$$

More explicitly, a moment tensor M with eigenvalues Λ, and orientation U, can be expressed as

$$M = ([\mathbf{N}, \mathbf{N} \times \mathbf{S}, \mathbf{S}] \cdot Y_{-\pi/4}) \cdot \Lambda \cdot ([\mathbf{N}, \mathbf{N} \times \mathbf{S}, \mathbf{S}] \cdot Y_{-\pi/4})^T \tag{1.7}$$

A compact notation of Equation 1.7 shows the main elements of the parameterization

$$M(\gamma, \beta, \kappa, \theta, \sigma) = [\Lambda(\gamma, \beta)]_{\widehat{U}(\kappa,\theta,\sigma)} \tag{1.8}$$

Equation 1.8 is the parameterization implemented as part of this thesis. The entries $\Lambda(\gamma, \beta)$ are the eigenvalues, with ranges

$$|\gamma| \leq \pi/6, \ 0 \leq \beta \leq \pi, \tag{1.9}$$

and the entries in the orientation matrix $U(\kappa, \theta, \sigma)$ are the strike, dip, and rake, with ranges

$$0 \leq \kappa \leq 2\pi, \ |\sigma| \leq \pi/2, \ 0 \leq \theta \leq \pi/2 \tag{1.10}$$

In order to estimate seismic full moment tensors, Equation 1.8 was implemented in the C-language, and within an algorithm for estimating seismic full moment tensors. The algorithm is described in the following section. This implementation is at the heart of this algorithm, and is utilized to generate every and any moment tensor within moment tensor space. To illustrate this point: a single inversion for one seismic event, at 5-degree increments for each moment tensor parameter, generates about 3×10^7 moment tensors. If adding magnitude search (say, 10 magnitude increments) and depth search (say, 10 depths), a single inversion may require over 3×10^9 moment tensors.

1.1.3 Seismic moment tensor estimation

The starting point for the inversions presented in this thesis is the Cut-And-Paste (CAP) algorithm for moment tensor inversion (Zhao & Helmberger, 1994; Zhu & Helmberger, 1996). This algorithm utilizes P waves (vertical and radial components), their first motion polarities, surface

waves (Love and Rayleigh), and an Earth model (local or regional) to search for a moment tensor that best matches the observations. The results in this thesis are based on a heavily modified version of CAP. The main modifications to the algorithm, and that are part of this thesis, are:

- a geometric full moment tensor parameterization
- adaptation of waveform processing and filtering routine to utilize short waveform windows
- development of a moment tensor inversion routine that
  - utilizes a uniform moment tensor parameterization
  - utilizes parallelization for efficient estimation
- utilize first motion polarity misfit to outline source-type regions in moment tensor space
- develop routines for estimating moment tensor catalogs and moment tensor uncertainties
- remove dependencies on a commercial license from Numerical Recipes (Press et al., 1988)

1.1.4 A uniform moment tensor parameterization

The parameterization described in Section 1.1.4, when applied directly, oversamples certain regions in moment tensor space. A homogeneous parameterization is a requirement to estimate uncertainties for moment tensors. Another modification in the CAP algorithm is to implement a uniform parameterization. In compact form, the parameterization G is (Tape & Tape, 2015) denoted as

$$G(u,v,\kappa,\sigma,h) = M\big(\gamma(u), \cos\beta(v), \kappa, \sigma, h, 1\big) \tag{1.11}$$

where

$$\begin{aligned} u &= \frac{1}{3}\sin 3\gamma && (|\gamma| \le \pi/6) \\ v &= \frac{3}{4}\beta - \frac{1}{2}\sin 2\beta + \frac{1}{16}\sin 4\beta && (0 \le \beta \le \pi) \\ h &= \cos\theta && (0 \le \theta \le \pi/2) \end{aligned} \tag{1.12}$$

The parameterization G represents a mapping of moment tensors into a space of moment tensors that are uniformly distributed. This parameterization required a new inversion routine within the CAP algorithm, which I implemented as part of this thesis along with a parallelization method. These changes allow for efficient moment tensor and uncertainty estimations.

1.2 Applications

1.2.1 Uturuncu volcano

Chapter 2 presents a catalog of 63 seismic moment tensors for events at Uturuncu volcano in Bolivia. The moment tensors were estimated from data collected during a seismic array deployment at the volcano between 2010–2013. The catalog represents the complete set of events for which we could obtain reliable moment tensor solutions. Each event in the catalog was estimated using as much of the waveforms as possible, including first motion polarities, P waves and surface waves. The events recorded during deployment of the array are relatively small ($M_w = 0.3 - 2.8$), and their waveforms contain high frequencies ($2 - 10$ Hz). One challenge in working with such small magnitudes is that only two events generated surface waves that were discernible in all seismic stations and that could be used for estimating their moment tensors.

Another challenge in estimating moment tensor at Uturuncu volcano is that the velocity structure in the region is not well known. For this study, catalogs of moment tensors were computed for several velocity models (West et al., 2013; Shen et al., 2016). The moment tensor solutions were analyzed for stability and robustness by comparing solutions among the catalogs. The analysis shows the influence of first motion polarities in obtaining robust moment tensor estimates.

This study utilized polarity and waveform misfits, both represented on a lune, to show the range of permissible source types for each event. The first motion polarities allow to discard solutions that do not agree with observations, and to reduce the range of possible solutions and source types. Within the space of allowable solutions the waveform misfit highlights those solutions that best match the observations. This analysis allowed us to identify three subsets of moment tensors within the catalog. Two subsets are near the volcano, one subset with positive isotropic events, the other with tensional crack events. The third subset, located about 15 km southeast of the volcano, occurred within a time period of 25 hours; for these events the double-couple moment tensor provides a decent fit to the observed waveforms.

The moment tensors estimated in this study provide a starting point for interpreting their physical source models. Two thirds of the events estimated in this study have Poisson ratios within permissible ranges, which suggests that the classical model applies to this portion of events. In terms of the CDC model, on the other hand, many events in this study have similar contributions from the double-couple and the crack moment tensors, which suggests that a multiple-process model is a possibility.

1.2.2 Earthquakes, volcanic events, and nuclear explosions

Chapter 3 examines events from previous studies: 21 earthquakes in southern Alaska (Silwal & Tape, 2016), 63 events at Uturuncu volcano in Bolivia (Alvizuri & Tape, 2016), and 29 earthquakes and nuclear tests at the Nevada Test Site (Ford et al., 2009). The goals of this study are to re-visit these moment tensor estimates, estimate their full moment tensors, and estimate their uncertainties. In comparison with the approach by Ford et al. (2009), this study: utilizes more stations; utilizes more of the waveform, including body waves and a broader frequency spectrum for surface waves; estimates moment tensor uncertainties; and characterizes source types.

A large portion of this study was spent in preparing the waveform data. Several events analyzed in this study occurred in the 1980s when there were a limited number of broadband sensors compared to the present, and when sensor outages seemed common, as is evident in gaps in the waveform records. In many cases the instrument response information which is required to calibrate the sensors, is either not standard format which makes its decoding problematic, or is missing, in which case the data is not usable.

This study presents a catalog of full moment tensors from the Nevada Test Site. This catalog builds on work by Ford et al. (2009), but includes more stations and more waveforms.

The misfit function is used to highlight those solutions that provide the best fit, and is also used to estimate a confidence parameter for source types. The results reveal the importance of evaluating the full space of moment tensors as opposed to a linearized inversion for an optimum solution. An example result for a nuclear explosion shows a global minima in the positive isotropic region, as expected for an explosion, along with local minima away from positive isotropic. The complexities of the misfit function can be distilled into a confidence curve.

The results in this study demonstrate the application of a new methodology to estimate full seismic moment tensors with uncertainties. The results are comparable with those from previous studies, except the results here utilize more stations and as much of the waveform as is possible. The methodology presented in this thesis, and its application allows for discussion of physical mechanisms of seismic sources.

1.3 References

Alvizuri, C. & Tape, C., 2016. Full moment tensors for small events ($M_w < 3$) at Uturuncu volcano, Bolivia, *Geophys. J. Int.*, **206**, 1761–1783, doi:10.1093/gji/ggw247.

Backus, G. & Mulcahy, M., 1976a. Moment tensors and other phenomenological descriptions of seismic sources—I. Continuous displacements, *Geophys. J. R. Astron. Soc.*, **46**, 341–361.

Backus, G. & Mulcahy, M., 1976b. Moment tensors and other phenomenological descriptions of seismic sources—II. Discontinuous displacements, *Geophys. J. R. Astron. Soc.*, **47**, 301–329.

Dziewonski, A., Chou, T.-A., & Woodhouse, J. H., 1981. Determination of earthquake source parameters from waveform data for studies of global and regional seismicity, *J. Geophys. Res.*, **86**(B4), 2825–2852, doi:10.1029/JB086iB04p02825.

Ford, S. R., Dreger, D. S., & Walter, W. R., 2009. Identifying isotropic events using a regional moment tensor inversion, *J. Geophys. Res.*, **114**, B01306, doi:10.1029/2008JB005743.

Gilbert, F., 1970. Excitation of normal modes of the Earth by earthquake sources, *Geophys. J. R. Astron. Soc.*, **22**, 223–226.

Gilbert, F., 1973. Derivation of source parameters from low-frequency spectra, *Phil. Trans. R. Soc. Lond.*, **274**, 369–371.

Gilbert, F. & Dziewonski, A. M., 1975. An application of normal mode theory to the retrieval of structural parameters and source mechanisms from seismic spectra, *Phil. Trans. R. Soc. Lond.*, **278**, 187–269.

Hudson, J. A., Pearce, R. G., & Rogers, R. M., 1989. Source type plot for inversion of the moment tensor, *J. Geophys. Res.*, **94**(B1), 765–774.

Kawakatsu, H., 1995. Automated near-realtime CMT inversion, *Geophys. Res. Lett.*, **22**(19), 2569–2572.

Press, W. H., Flannery, B. P., Teukolsky, S. A., & Vetterling, W. T., 1988. *Numerical Recipes in C*, Cambridge U. Press, New York.

Shen, W., Alvizuri, C., Lin, F.-C., & Tape, C., 2016. A one-dimensional velocity model for Uturuncu volcano, Bolivia, and its impact on full moment tensor inversions, *Geosphere* (in press), doi:10.1130/GES01353.1.

Silwal, V. & Tape, C., 2016. Seismic moment tensors and estimated uncertainties in southern Alaska, *J. Geophys. Res. Solid Earth*, **121**, 2772–2797, doi:10.1002/2015JB012588.

Sipkin, S. A., 1982. Estimation of earthquake source parameters by the inversion of waveform data: synthetic waveforms, *Phys. Earth Planet. Inter.*, **30**, 242–259.

Tape, W. & Tape, C., 2012. A geometric setting for moment tensors, *Geophys. J. Int.*, **190**, 476–498, doi:10.1111/j.1365-246X.2012.05491.x.

Tape, W. & Tape, C., 2015. A uniform parameterization of moment tensors, *Geophys. J. Int.*, **202**, 2074–2081, doi:10.1093/gji/ggv262.

West, M. E., Kukarina, E., & Koulakov, I., 2013. Structure of Uturuncu volcano from seismic tomography, Abstract V13B-2600 presented at 2013 Fall Meeting, AGU, San Francisco, Calif., 9-13 Dec.

Zhao, L.-S. & Helmberger, D. V., 1994. Source estimation from broadband regional seismograms, *Bull. Seis. Soc. Am.*, **84**(1), 91–104.

Zhu, L. & Helmberger, D., 1996. Advancement in source estimation techniques using broadband regional seismograms, *Bull. Seis. Soc. Am.*, **86**(5), 1634–1641.

Chapter 2

Full moment tensors for small events ($M_w < 3$) at Uturuncu volcano, Bolivia[1]

2.1 Abstract

We present a catalog of full seismic moment tensors for 63 events from Uturuncu volcano in Bolivia. The events were recorded during 2011-2012 in the PLUTONS seismic array of 24 broadband stations. Most events had magnitudes between 0.5 and 2.0 and did not generate discernible surface waves; the largest event was M_w 2.8. For each event we computed the misfit between observed and synthetic waveforms, and we used first-motion polarity measurements to reduce the number of possible solutions. Each moment tensor solution was obtained using a grid search over the six-dimensional space of moment tensors. For each event we show the misfit function in eigenvalue space, represented by a lune. We identify three subsets of the catalog: (1) 6 isotropic events, (2) 5 tensional crack events, and (3) a swarm of 14 events southeast of the volcanic center that appear to be double couples. The occurrence of positively isotropic events is consistent with other published results from volcanic and geothermal regions. Several of these previous results, as well as our results, cannot be interpreted within the context of either an oblique opening crack or a crack-plus-double-couple model. Proper characterization of uncertainties for full moment tensors is critical for distinguishing among physical models of source processes.

2.2 Introduction

Seismic waveforms of three-component ground motion contain information about source processes and earth structure. In order to make inferences about the source process, we need to account for how seismic waves propagate through some assumed model of earth structure. In this study we focus on a data set of seismic waveforms recorded at Uturuncu volcano in Bolivia. We examine a catalog of events and estimate seismic moment tensors as a first step toward characterizing the source processes at the volcano.

The seismic moment tensor is a 3×3 symmetric matrix that describes the pattern of radiation from a seismic source. Six numbers are needed to describe the moment tensor: three eigenvalues describing the source type and magnitude, and three angles (strike, slip, and dip) describing the orientation. For $\Lambda = (\lambda_1, \lambda_2, \lambda_3)$ and U a rotation matrix, the moment tensors $[\Lambda]$ and $[\Lambda]_U$ are

[1] Published as Alvizuri, C. and Tape, C. (2016), Full moment tensors for small events (Mw < 3) at Uturuncu volcano, Bolivia, *Geophys. J. Int.*, 206(3), 1761–1783, doi:10.1093/gji/ggw247

defined by

$$[\Lambda] = \begin{pmatrix} \lambda_1 & 0 & 0 \\ 0 & \lambda_2 & 0 \\ 0 & 0 & \lambda_3 \end{pmatrix} \tag{2.1a}$$

$$[\Lambda]_U = U[\Lambda]U^{-1} \tag{2.1b}$$

The notation $M = [\Lambda]_U$ provides an explicit separation between the source type (with Λ) and the orientation (U).

A source type for a moment tensor is its normalized and ordered eigenvalue triple $\Lambda = (\lambda_1, \lambda_2, \lambda_3)$ ($\|\Lambda\| = 1$ and $\lambda_1 \geq \lambda_2 \geq \lambda_3$). Due to the normalization and ordering, the source types make up one-sixth of the unit sphere—the lune shown in Figure 2.1. Each source type Λ can be specified by its longitude γ and latitude δ on the lune. In beachball terms, Λ determines the colored pattern on the beachball, but without some physical model for moment tensors it does not determine the actual source process.

The classical model of Aki & Richards (1980) (see also Dufumier & Rivera, 1997) describes a moment tensor as an oblique (tensional or compressional) crack and a Poisson parameter for the source region. Alternatively the moment tensor can be described as a two-process model that is the sum of a crack tensor and a double couple whose fault plane is aligned with the crack (Minson et al., 2007). A comparison of the classical model and the crack-plus-double-couple (CDC) model is presented in Tape & Tape (2013), who also elaborate on a more generalized CDC model that was introduced by Julian et al. (1998), in which the fault plane of the double is not aligned with the crack plane. Without additional constraints on the source process (e.g., the orientation of a crack plane from microseismicity), it is impossible, in the generalized model, to infer the crack and double couple from seismic waveforms.

The literature summarized in Table 2.1 provides context for our study. These studies estimated full moment tensors in a variety of settings: geothermal and volcanic regions (Guilhem et al., 2014; Pesicek et al., 2012; Julian et al., 2010; Minson et al., 2007; Miller et al., 1998b; Dahm & Brandsdóttir, 1997), mines (Ford et al., 2009; Šilený & Milev, 2008, 2006), hydraulic fracturing (Eisner et al., 2010; Baig & Urbancic, 2010; Šilený et al., 2009; Julian et al., 2010; Foulger et al., 2004), landslides (Nayak & Dreger, 2014), glaciers (Walter et al., 2010, 2009), explosions (Minson & Dreger, 2008; Ford et al., 2009, 2010, 2012; Chiang et al., 2014), and earthquakes (Ross et al., 2015; Stähler & Sigloch, 2014; Stierle et al., 2014; Vavryčuk, 2011; Horálek et al., 2002; Vavryčuk, 2001). See also the review by Julian et al. (1998) and Miller et al. (1998a) for previous studies, and see Chouet & Matoza (2013) for a review of studies specific to volcanic settings.

Table 2.1 also compares the choice of seismic data and the approach to moment tensor inversion in different studies. For larger events (say, $M_w > 3$) we see that lower frequency waveforms

($f < 0.2$ Hz or $T > 5$ s) can be used to estimate moment tensors, whereas smaller events require using higher frequency waveforms or using only the polarity of the first-motion P wave. Once the time windows of waveforms have been selected, one must decide how to compute synthetic seismograms and then how to measure the waveform difference between observations and synthetics. Finally there is a choice of how to estimate the best-fitting moment tensor, either using a linearized inversion or using a grid search over the model parameter space.

We also examine in Table 2.1 how previous studies have addressed uncertainties of moment tensors. We label each study according to: (A) whether formal uncertainties are addressed (e.g., Stähler & Sigloch, 2014), (B) whether the misfit function is represented on the space of moment tensors (e.g., Ford et al., 2010), (C) whether some other approach was used, such as perturbing synthetic seismograms to see the perturbations on estimated moment tensors (e.g., Riedesel & Jordan, 1989; Šilený & Milev, 2006), and (–) whether uncertainties were not addressed or not reported (Table 2.2).

In this study we examined 63 events with magnitudes 0.3–2.8. Such small events produce relatively high frequencies. For most events we were only able to use high-frequency (2–10 Hz) P waveforms; for the largest events we used surface waves (0.25–0.50 Hz). We used a grid-search algorithm to obtain the moment tensor whose synthetic seismograms provide the best fit to observed seismograms (Zhu & Helmberger, 1996; Zhu & Ben-Zion, 2013). We use the source-type representation on the lune (Tape & Tape, 2012) (Figure 2.1) to outline regions of solutions that are allowed by first-motion polarity observations, and we use the waveform misfit to highlight regions of confidence around the best-fitting moment tensor. Our graphical display of misfit in the model parameter space of full moment tensors is a step towards obtaining formal uncertainties. These displays are particularly important for small events where only a limited portion of the seismic wavefield can be used and hence uncertainties are larger. Within our catalog of 63 events are several events requiring non-double couple mechanisms.

2.2.1 Uturuncu volcano

The Altiplano of the central Andes is a broad plateau characterized by substantial relief (elevations 3.5–4.7 km) and overlying a 70-km thick crust (Isacks, 1988). Cerro Uturuncu, within the Altiplano, is a stratovolcano that was last active 270 ka (Sparks et al., 2008). Uturuncu volcano is part of a large regional cluster of volcanoes, nested calderas, and ignimbrite sheets termed the Altiplano-Puna volcanic complex (APVC) (de Silva, 1989). The region experienced extensive magmatism starting 11 Ma (de Silva, 1989) in eruptive episodes, with rates up to 31 km^3/ka, generating over 12,000 km^3 of ignimbrites (Salisbury et al., 2011).

The crust beneath the APVC is characterized by geophysical anomalies such as very low seismic velocities and high seismic attenuation (Zandt et al., 2003), low electrical resistivities (Haberland et al., 2003; Comeau et al., 2015), and negative gravity anomalies and low densities (del Potro et al., 2013). A regional-scale mid-crustal magma reservoir termed Altiplano-Puna Magma Body (APMB) was identified beneath the APVC at depth of about 15 km (19 km below the surface) (Chmielowski et al., 1999). A recent seismic study using surface wave dispersion and receiver functions estimates that the APMB is about 200 km wide, 11 km thick, is at depths 4–25 km, and has a volume of about 500,000 km^3 (Ward et al., 2014).

Geodetic satellite observations in the region have identified ongoing surface uplift centered at Uturuncu volcano at a rate of 10–15 mm/yr (Pritchard & Simons, 2002) and peripheral subsidence (Fialko & Pearse, 2012). These studies have concluded that the deformation may be linked with the APMB, and suggest a mid crust source above a depth of 20 km. Active fumaroles (Sparks et al., 2008) and geothermal fields in the region also suggest active magmatic activity (de Silva, 1989).

Uturuncu volcano was the focus of the second part of a multi-disciplinary project known as PLUTONS, which was active 2009–2015 and was supported by the Continental Dynamics program of the National Science Foundation. [The acronym PLUTONS, with a few extra letters, stands for: Probing Lazufre and Uturuncu TOgether: Nsf (usa), Nerc (uk), Nserc (canada), Sergeotecmin (bolivia), Sernageomin (chile), observatorio San calixto (bolivia), universidad nacional de Salta (argentina), universidad mayor San andres (bolivia), universidad de potoSi (bolivia), Sernap (bolivia), chilean Seismological service, universidad de San juan (argentina).] An array of broadband stations was installed at Uturuncu volcano (West & Christensen, 2010) in order to record the local activity associated with volcanic (and tectonic) deformation.

We use seismic data from the PLUTONS project to estimate moment tensors for events beneath Uturuncu volcano. The goal of our study was to estimate full moment tensors for all possible events at Uturuncu volcano, along with their uncertainties. As far as we can tell, these are the first moment tensors—full or double couple—examined for this volcano. Double couple moment tensors for the larger region are available from, e.g., Chinn & Isacks (1983) and Devlin et al. (2012, see their Table 1).

2.3 Methods

2.3.1 Selection of events

The objective of our study is to estimate full moment tensors using the best available seismic data at Uturuncu volcano. Therefore we focus on shallow events that are inside the station array. We ignore events in the underlying slab, for which the station array forms a much smaller aperture.

Figure 2.2 summarizes the seismicity catalog for the PLUTONS project, and it also highlights our selection of events for analysis.

We focus on events at Uturuncu volcano that are between longitudes -67.4° and -66.9° and latitudes -22.6° and -22.1° and above a depth of 60 km. (All depths listed are with respect to sea level, not the topographic surface, unless explicitly stated.) The PLUTONS seismicity catalog (Keyson & West, 2013) is complete through 2012-03-09 and contains 1433 events within this region, spanning the time period from 2009-04-26 to 2012-03-09 and including stations from both Lazufre volcano (Jay et al., 2011) and Uturuncu volcano. We focus on the time period of the Uturuncu stations only, from 2010-04-12 to 2012-03-09 (Figure 2.2b). Within this time period, there are 421 events, the majority of which occurred at a depth of 4–6 km; since the mean station elevation is 4.6 km, these events occur at about 10 km below the surface.

Uturuncu volcano did not produce many sizable earthquakes during the time period of the PLUTONS project. Based on the frequency-magnitude distribution for the 421 events in our region of interest (Figure 2.2c), we expect one $M > 2.5$ event per two years and about 100 $M > 0$ events per year. The magnitude of the catalog completeness is $M_c = 0.0$.

In order to isolate the most promising events for moment tensor inversion, we reduce the set of 421 to 101 events by forming two subsets. The first is the set of the 21 events with $M \geq 1$. The second is the set of 80 events with $M \geq 0$ and having ≥ 20 recording stations. For the small events we could only use P waveforms and polarities, so we restricted the subset to have the most stations. We chose the large events in order to try to model surface waves, even if only a limited number of stations were recording. The set of 101 events was reduced to 72 using the criterion that an event must have $\geq$5 first-motion polarities that have arrival times that are consistent with a simple velocity model. The set of 72 events was reduced to 63 by excluding outlier events from a scatter plot of P travel time (from the catalog) vs hypocentral distance (Figure A.2). The 63 events that we analyze represent a subset of all events within the PLUTONS catalog that we deem to be suitable for full moment tensor inversions.

2.3.2 First-motion polarity measurements

Given the small size of the events at Uturuncu volcano, we could not rely on waveform-only comparisons to obtain reliable moment tensors, as do studies with regional seismic networks recording large ($M \geq 4$) events (e.g., Tan et al., 2010). First-motion polarity measurements have been used in a number of studies of full moment tensors (Table 2.1), and they proved to be valuable for the small events in our study.

For all seismograms in this study, we deconvolved the instrument response over the frequency range 0.05–20 Hz. First-motion polarity measurements were made on the vertical component

waveforms; in the case of some of the smallest events, we applied an $f > 1$ Hz high-pass filter to enhance the signal-to-noise level. An 'upward' (or 'outward') measurement corresponds to a compression; a 'downward' (or 'inward') measurement corresponds to a dilatation. If a waveform did not have a discernible first motion—either due to poor signal-to-noise or due to a non-abrupt P wave—it was not used in the inversion. Three seismologists picked the first-motion polarities; any discrepancies among the three choices were resolved following collective discussion and analysis.

2.3.3 Grid-search moment tensor inversion

Estimating moment tensors using a grid search requires a choice of model parameter space, a choice of a seismic velocity model, the calculation of synthetic seismograms, a choice for a misfit function to compare observed and synthetic seismograms, and an algorithm to determine the minimum of the misfit function.

Our space of model parameters has six dimensions, consistent with the number of entries in a 3×3 symmetric matrix. Our six parameters, however, are not the matrix entries but rather strike angle, rake angle, dip angle (all for the closest double couple), lune latitude δ, lune longitude γ, and moment magnitude (Table A.3). The strike, rake, and dip angles determine the moment tensor orientation, and δ and γ determine the source type.

Our moment tensor inversion method is the 'cut-and-paste' (CAP) algorithm (Zhao & Helmberger, 1994; Zhu & Helmberger, 1996), which has recently been extended to full moment tensors by Zhu & Ben-Zion (2013). The source time function is assumed to have the simple form of a trapezoid function. Synthetic waveforms are pre-computed in a layered model (or homogeneous model) over a range of distances and event depths using the frequency-wavenumber method (Zhu & Rivera, 2002). The basic premise of the moment tensor inversion algorithm is that P waves (vertical and radial components) and surface waves (Love and Rayleigh) are windowed separately and filtered separately. Within each time window, a time shift is applied to the synthetic waveforms with the intention of correcting for errors due to the user-input velocity model. Then within each time window a direct waveform difference is measured. We force the time shift for the P wave to be the same on the vertical and radial components, and we force the time shift for the Rayleigh wave to be the same on the vertical and radial components.

Our main adaptation to the code of Zhu & Helmberger (1996) is the use of the L1 norm (Eq. 2.2a), as described in Silwal & Tape (2016). The misfit function is

$$\Phi(M) = \sum_{j=1}^{N} \sum_{i=1}^{5} \phi_{ij}(M) \tag{2.2a}$$

$$\phi_{ij}(M) = \left[\left(\mathbf{u}_{ij} - \mathbf{s}_{ij}(M) \right)^T \mathbf{W}_{ij} \left(\mathbf{u}_{ij} - \mathbf{s}_{ij}(M) \right) \right]^{1/2}, \tag{2.2b}$$

where i is the index over 5 possible waveform sections, j is the index over N stations, $\mathbf{u}_{ij}$ is the observed seismogram, $\mathbf{s}_{ij}(M)$ is the discretized seismogram for moment tensor M, $\phi_{ij}(M)$ is the L2-norm waveform difference within each time window, weighted by matrix $\mathbf{W}_{ij} = w_{ij}\mathbf{I}$ (see Section 2.3.4). Variance reduction is a normalized measure that provides a better comparison from one event to the next. This is computed as

$$VR(M) = 100 \times \left(1 - \left(\frac{\Phi(M)}{\|\mathbf{u}\|_{L1}}\right)^2\right) \tag{2.3}$$

where

$$\|\mathbf{u}\|_{L1} = \sum_{j=1}^{N}\sum_{i=1}^{5}\sqrt{\mathbf{u}_{ij}^T\,\mathbf{W}_{ij}\,\mathbf{u}_{ij}} \tag{2.4}$$

is the data normalization factor that is independent of M. Variance reduction can be negative; its range is $VR \leq 100$.

For the small-magnitude events in this study, it was challenging to fit the observed P waveforms with synthetic waveforms. We filtered the P waveforms between 2–10 Hz to provide the best signal-to-noise. Even in cases where the observed and synthetic P waveforms have similar shapes, it is possible for the synthetic waveform to be matched with a different observed waveform that has a higher cross correlation value; this misalignment of waveforms is known as cycle-skipping. To minimize the chances of cycle-skipping we forced the synthetic P waveform to start at the time of the P onset in the catalog (Keyson & West, 2013). We then allowed time shifts to the synthetics of $|\Delta T| \leq 0.05$ s. The variable $\mathbf{s}$ in Equation (2.2b) is taken to be the discretized version of the time shifted synthetic seismogram.

We also use first-motion polarities during the grid search. For each moment tensor M we calculate how many predicted polarities $n(M)$ do not match the observed polarities:

$$n(M) = \tfrac{1}{2}\sum_{j}^{N}\left|k_j^{\text{obs}} - k_j(M)\right| \tag{2.5}$$

where k_j^{obs} is the observed first-motion polarity (1 or -1) at the jth station and $k_j(M)$ is the predicted first-motion polarity (1 or -1). Thus $n(M)$ is at least zero (all measurements match) and at most N (all measurements mismatch).

In our inversions we discard any moment tensor with $n(M) > 0$, that is, any moment tensor whose predicted polarities did not match all of the observed polarities. This is a strong constraint that emphasizes the first-motion polarities. An alternative would be to use a misfit function that combines the waveform misfit $\Phi(M)$ with the polarity misfit $n(M)$. The main reason for using first-motion polarities is due to the challenges of fitting waveforms for small-magnitude events in structurally complex regions. By allowing synthetic waveforms to be time-shifted to match

observed waveforms, there is always a danger of cycle-skipping. The inclusion of first-motion polarities reduces the chance of cycle-skipping for the P waveforms.

2.3.4 Choice of velocity model and weights for misfit function

The seismic velocity structure at Uturuncu volcano is not well known. Regional studies (Zandt et al., 2003; Ward et al., 2014) provide 1D models with layers so thick that most of our events are within the uppermost layer. We performed full moment tensor inversions for 63 events using a local 1D model (Shen et al., 2016) and a homogeneous model. The homogeneous model is described by V_P = 4800 m/s, V_S = 2820 m/s, ρ = 2306 kg/m^3, Q_P = 1000, and Q_S = 500; values for V_P and V_S were obtained from the upper layer of a tomography study by West et al. (2013); values for ρ, Q_S, and Q_P, where $\rho = 0.77 + 0.32 * V_P$, are set by default while computing synthetic waveforms with the frequency-wavenumber method (Zhu & Rivera, 2002). The moment tensor solutions obtained with the homogeneous model provided a better fit to the observed data, as discussed in Section 2.6. However, when using the homogeneous model we needed to adjust the misfit function used in the inversion, as described next.

Ray paths for a homogeneous model are straight lines. The presence of a shallow slow layer will refract the ray with a steeper incident angle at the station. Therefore the synthetic amplitude ratio between the vertical component and radial component of the P wave will increase if a slow uppermost layer is added to a homogeneous model.

For each station and for each event, we calculated the amplitude of the P wave on the vertical and radial components for both the observed and synthetic waveforms. These quantities allowed us to examine two different amplitude ratios: (1) $\ln(A_{obs}/A_{syn})$, the ratio between observed and synthetic P wave amplitudes (either vertical or radial component), (2) $\ln(Z/R)$, the ratio of the vertical component P wave amplitude to the radial component amplitude. We used these amplitude ratios to guide our choice of velocity model and our choice of weights in the inversion.

Whether we assume a homogeneous model or a 1D model, the take-off angles of ray paths from the source are low-angle (with respect to horizontal). Our assumption of a homogeneous model results in predictions of higher amplitude P waves on the radial component compared to the vertical component (Figure A.4). However, our P wave amplitudes are larger on the vertical component, indicating steeper incident angles at the station than would be expected for a homogeneous model. In order for our synthetic amplitudes to better match observed ones, we could have added a shallow slow layer. Instead, we preferred to keep the simpler homogeneous model, and we obtained the better match by adjusting the weights for the waveforms in the inversion.

With equal weights for fitting the vertical and radial components of P waves, we discovered that the amplitude ratios were centered for the radial component but skewed for the vertical com-

ponent (Figure 2.3a). It appears that the artificially high amplitudes of the radial component P waves were leading to moment tensor solutions with worse-than-desired amplitude fits for the vertical component P waves.

Since our first motion polarity measurements were made on the vertical component, we wanted to fit the vertical component waveforms above all. We achieved this by down-weighting the waveform fitting of the radial component P waves within the inversion. The result on the moment tensor inversion is shown in Figure 2.3b, where the amplitude ratios are centered for the vertical component but skewed for the radial component.

2.4 Full analysis for an example event

We display results for one event in Figures 2.4–2.8. This event, with magnitude M_w 2.8, is the largest in the data set and generates large enough surface waves to be compared with synthetic seismograms. Our grid search over six parameters (magnitude, lune longitude, lune latitude, strike, dip, rake) results in the moment tensor M_0 shown at the top of Figure 2.4. (The moment tensor M_0 is not to be confused with the scalar seismic moment, also usually denoted by M_0.) The grid search is limited to moment tensors whose predicted first-motion polarities all match the observations.

The waveform fits for the event in Figure 2.4 have room for improvement, as the waveforms do not match wiggle-for-wiggle. Furthermore, the actual amplitude differences are larger than they appear in Figure 2.4, where we have scaled each waveform in each window in order to best view the waveform shapes (Figure A.8 shows the unscaled waveforms). These differences in waveform fits, especially due to amplitudes, are to be expected for events of this magnitude ($M \leq 3$) and with waveforms filtered at these frequencies: 2–10 Hz for P waves and 0.25–0.50 Hz for surface waves. From our standpoint, what is most important is that we can use more than just the first-motion polarity to estimate the moment tensor. For all events in our study, we try to fit the shapes and amplitudes of the P waveforms—especially on the vertical component—and for this event we are also able to use the surface waves, which have large enough signal.

In Figure 2.5 we show how the moment tensor solution varies as a function of event depth. The optimal depth is at 4.4 km below the surface elevation of 4.6 km, which differs by only 0.8 km from the traveltime-derived depth of 0.6 km. Our choice of optimal depth relies on the accuracy of the amplitude measurements. The depths listed in the catalog are based on P and S traveltimes, which are more reliable (Keyson & West, 2013). Therefore for all other events in our study we chose to use event depths listed in the catalog.

The variation in the misfit function is represented by the plots in Figure 2.6. The locations of the stations relative to the event are plotted in (a), with each station colored according to the observed

first-motion polarity. For each moment tensor M in our grid search we calculate the number of misfitting polarity measurements $n(M)$ (Eq. 2.5). We define $n(\Lambda)$ as the minimum number of misfitting polarity measurements for a given lune point Λ:

$$n(\Lambda) = \min\left(n([\Lambda]_U) \,:\, U \in \mathbb{U}\right) \tag{2.6}$$

where $\mathbb{U}$ is the set of all orientations and where $[\Lambda]_U$ and $n([\Lambda]_U)$ are given by Equations (2.1) and (2.5). Figure 2.6b is a plot of $n(\Lambda)$ for the example event. A blue point ($n(\Lambda) = 0$) indicates that there is at least one orientation U for which the predicted polarities of $[\Lambda]_U$ all match the observed polarities. A green point ($n(\Lambda) = 1$) indicates that there is at least one orientation for which the predicted polarities match all but one of the observed polarities, but there is no orientation whose predicted polarities match all of the observed polarities. In Figure 2.6b (see also Figure 2.1) all points Λ above the arc $\lambda_3 = 0$ are red ($n(\Lambda) = 4$); since $\lambda_1 \geq \lambda_2 \geq \lambda_3 > 0$, then all polarities of $[\Lambda]_U$ are upward, regardless of U, and $n(\Lambda)$ must then be the number of stations with downward polarity, which in this example is four. Similarly, if Λ is below the arc $\lambda_1 = 0$, then $n(\Lambda)$ is the number of stations with upward polarity, which in this example is seven.

The inclusion of polarities in the inversion restricts the number of moment tensor grid points for which we calculate the waveform misfit (Eq. 2.2). As a result, the source-type grid points Λ are restricted to the region $n(\Lambda) = 0$ of the lune (shaded in Figure 2.6c, blue in Figure 2.6b). At each such Λ, a beachball is plotted in Figure 2.6c. The beachball is the 'best' moment tensor at Λ, in the sense that it minimizes the misfit function for moment tensors M with source type Λ and $n(M) = 0$; the orientation and magnitude of M are allowed to vary, but the source type Λ is fixed. Each beachball in the figure is colored by its misfit value (or rather variance reduction VR). Stated more formally: on the lune subset $n(\Lambda) = 0$ we define a function $\Phi(\Lambda)$ in terms of $\Phi(M)$ (Eq. 2.2) by

$$\Phi(\Lambda) = \min\left\{\Phi(t[\Lambda]_U) : U \in \mathbb{U},\, n([\Lambda]_U) = 0,\, t_1 \leq t \leq t_2\right\} \tag{2.7}$$

The variable t changes the magnitude of the moment tensor.

Figures 2.6b-c convey more information than does the minimum misfit solution M_0 alone, which is shown in Figure 2.6d as well as in the green box in Figure 2.6c. We see that, based on polarities alone, many source types are possible, ranging from a tensional crack on the left boundary of the lune, to a double couple at the center of the lune, to a variety of compressional cracks on the right boundary. We see, from the values of the waveform misfit function at the best beachballs, that there is a whole range of source types—dark blue in Figure 2.6c—that are nearly as plausible as the source type for M_0.

We use the example event to explore the stability of the moment tensor solution when using different subsets of waveforms and different choices of weighting. We quantify the difference between two moment tensor solutions, M_1 and M_2, in terms of

1. the difference ΔVR in variance reduction

2. the angular difference $\omega = \angle(M_1, M_2)$ between moment tensors

3. the angular difference $\theta = \angle(\Lambda_1, \Lambda_2)$ on the lune between two source types

If the pair of moment tensors has the same U, then $\omega = \theta$; otherwise $\omega \geq \theta$ (Tape & Tape, 2013).

2.4.1 Influence of first-motion polarities

Figures 2.7a-b show a comparison between the moment tensor solutions obtained with and without polarity measurements. The moment tensors in (a) and (b) are quite similar ($\omega = 9^\circ$, $\theta = 6^\circ$), providing support for using all polarity measurements in the grid search. We see that the polarities at two stations (PLAR and PLLO) are upward and are not predicted by the moment tensor in (b). This is not too surprising, since the misfit function is a sum of waveform differences for all time windows, so the algorithm will tend to fit the largest waveforms, possibly at the expense of not fitting the amplitudes or polarities of smaller waveforms. As discussed in Section 2.3.3, by using polarity measurements we ensure that all first-motion polarities are fit.

2.4.2 Influence of different waveform components

In Figures 2.7c-d we repeat the inversions of Figures 2.7a-b, but without using surface waves. The comparison provides insights into how much the surface waves are influencing the solution. For the example in Figure 2.7, it appears that the surface waves have a tendency to pull the source type from the compressional cracks toward the double couple. For most of the 63 events we could not identify any surface waves. Figure 2.7 is a reminder that the inclusion of surface waves could influence the solutions.

We would also like to see stability of the solution when using different subsets of waveforms. Figure 2.8 shows solutions for the case of (a) vertical-component P waves only, (b) radial-component P waves only, (c) surface waves only, and (d) all together. In all cases we use first-motion polarity measurements. The solution with the worst misfit is for radial-component P waves only (Figure 2.8b). We know from measurements of amplitude ratios (Figure A.4) that the synthetic P radial component is too large and therefore we see that over-fitting this component can lead to spurious results. This was discussed in Section 2.3.4.

The solutions using vertical-component P waves only (Figure 2.8a), surface waves only (Figure 2.8c), and both (Figure 2.8d) are similar. We find that the inclusion of surface waves and radial waves both have the effect of producing worse (lower) VR, though the waveform differences are

subtle to the eye. Our preference is to fit as much of the waveforms as possible, so we would like to fit more waveforms even if their inclusion leads to lower VR values.

2.5 Catalog of moment tensors

We performed two sets of inversions for all 63 events in order to examine the influence of using first-motion polarities. Figure 2.9 summarizes the differences between the two sets of inversions. For 40 out of 63 events, the difference between moment tensors is $\omega \leq 10^\circ$, the difference between source types is $\theta \leq 10^\circ$, and the difference in variance reductions is $\Delta VR <= 2\%$, indicating that the inclusion of polarities does not produce substantially different solutions. In our final catalog we choose to fit all polarity measurements, recognizing that the waveform fits will be quantitatively slightly worse.

To illustrate these results, we select four events from Figure 2.9 to display in Figure 2.10. The events in (a)-(c) are representative in the sense that the differences between the solutions with and without using polarities are small. They show that by fitting waveform differences for P waves (but not using first-motion polarities), we are able to also predict the correct polarity of the P wave for almost all stations. The one exception is station PLLL in (b), and, for this moment tensor, PLLL is a nodal station. Figure 2.10d shows an extreme case, where the inclusion of first-motion polarities leads to a very different solution. This event (20110823072700783) has the largest difference in VR among all 63 events: VR = 24 with polarities and VR = 36 without polarities. A visual inspection of the waveforms (Alvizuri, 2015) indicates that the no-polarity-case moment tensor (with M_w 1.7) provides somewhat better fits than the polarity-case moment tensor (with M_w 1.5).

Our full catalog is shown in Figure 2.11a and is available in Alvizuri (2015). Event origin times, hypocenters, and moment tensor results are listed in Table 2.4. Our 63 moment tensor solutions M_0 can be effectively represented by plotting them on the lune (Figure 2.11a). The location of the beachball on the lune provides its source type. The proximity of each solution to 'end member' moment tensors—such as the explosion source (at top), the double couple (at center), or the CLVDs (left and right)—can be seen by inspection. The color of the beachball provides the magnitude and the beachball itself conveys the orientation. What is not conveyed in Figure 2.11a is the uncertainty associated with each solution; for this, we rely on source-specific plots showing the variation of misfit on the lune. In Section 2.6 we discuss the source types shown in our catalog in the context of previous studies such as those in Figure 2.11b.

2.5.1 Subsets of the catalog

We single out three subsets of events, in hopes of identifying different physical mechanisms that may be active at Uturuncu volcano. We refer to the subsets as isotropic, tensional crack, and double couple events.

The isotropic events are shown in Figure 2.12. We define an event to be 'isotropic' if (1) its first-motion polarities are upward at all stations and (2) $n(\Lambda^D) \neq 0$, where $\Lambda^D = (1, 0, -1)$ is the double couple point at the center of the lune. The second condition says that no double couple, regardless of orientation, can have the correct polarities, that is, polarities that match the observed polarities at all stations. For an isotropic event, any moment tensor with source type Λ in the region $\lambda_3 > 0$ of the lune will have correct polarities, but there may be many other moment tensors that also have correct polarities, since, as shown in Figure 2.12, it may be possible to rotate a given beachball so that its white portions contain no stations. In fact, only one of the six events in Figure 2.12 has a best-fitting moment tensor whose source type Λ is in the region $\lambda_3 > 0$, where all first motions are upward. The lune latitudes for the source types of the six moment tensors range from $\delta = 23^\circ$ to $\delta = 46^\circ$; although the source types are not close to $(1, 1, 1)$, they are far from being deviatoric.

The tensional crack events are shown in Figure 2.13. We define an event to be a 'tensional crack' if (1) its best fitting moment tensor has its source type Λ in the region $\gamma = -15^\circ$ of the lune and (2) $n(\Lambda^D) \neq 0$. Four of the events in Figure 2.13 have best fitting beachballs (moment tensors) that have thin white bands, and one might hope that the events would be associated with a single physical process. In that case the orientations of the bands on the four balls should more or less agree, but they do not.

We define the 'double couple events' by their location; they are all clustered in a single region about 15 km southeast of the volcano. All 14 of the events in this region are shown in Figure 2.14. Most of these events occur within hours of each other and have similar moment tensor solutions. For all 14 events, a double couple moment tensor is a possible solution on the basis of polarities ($n(\Lambda^D) = 0$). (However, note that with only six recording stations, the first-motion polarity measurements cannot exclude many source types.) Therefore these events could arise from shear slip on a fault (i.e., with no opening).

Figure 2.15a-b shows where our subsets of events are with respect to the volcanic center and where they appear on the lune. We see that the subsets of isotropic and tensional crack events occur near the volcanic center. We also see that the swarm of possible double couple events are slightly skewed toward the compressional CLVD (Figure 2.15b).

It is important to realize that our definitions of 'isotropic,' 'tensional crack,' and 'double couple' here are rather formal and may not say much physically about the nature of the actual source

processes. Our tensional crack events, for example, are approximately tensional cracks in the traditional sense if the classical moment tensor model (Aki & Richards, 1980) is applicable. The moment tensors inferred in our study, however, give little, if any, support for the classical model, since many of them, if interpreted in the classical model, would require unreasonable values for the Poisson parameter.

2.6 Discussion

2.6.1 The quality of waveform fits

The moment tensor literature includes solutions with higher values of *VR* and better-looking waveform fits than those displayed in Figure 2.4 or in Alvizuri (2015). The perceived lower quality of our waveform fits arises because we are dealing with small events. Such events give clear P wave signals only at high frequencies ($f \geq 1$ Hz), while the lower frequencies, which would normally be more reliable, are unavailable. From our perspective, by considering waveforms, rather than only the sign (or amplitude) of the first-motion polarities, we take a step forward in improving the estimation of moment tensors for small events.

The value of *VR* is calculated from amplitude differences and provides a useful comparison with other studies only when the misfit functions (including the chosen bandpass filters) are similar. For example, if the signal-to-noise ratios are adequate, then filtering seismograms at longer periods will result in better waveform fits and larger *VR*. This is because the assumption of a simple (e.g., layered) structure will be more appropriate for longer period waves. In general, we are interested in fitting the broadest possible band of frequencies, even if it results in lower *VR*. Also, at higher frequencies, the influence of 'site effects'—seismic velocity variations near each station—become more significant and contribute toward lower *VR*. (We discuss site effects in Section A.3.)

2.6.2 Toward uncertainty estimation for full moment tensors

Our waveform misfit function (Eq. 2.2) is evaluated over a six-dimensional space of moment tensors. Moment tensor source types make up the lune, which is one-sixth of the unit sphere. Using plots such as Figure 2.6, we emphasize the importance of showing the variations of the misfit function $\Phi(\Lambda)$ (Eq. 2.7) over the space of source types, something that was first done by Ford et al. (2010, 2012) (Table 2.1).

We acknowledge that we have not considered all sources of uncertainties, namely, the effects of three-dimensional structural variations (elastic or anelastic), the effects of topography, and uncertainties associated with different earthquake source parameters. The influence of three-

dimensional structural variations has been considered in some studies (Liu et al., 2004; Chen et al., 2005; Covellone & Savage, 2012; Zhu & Zhou, 2016). The effects of topography have been considered for longer period waveforms (Liu et al., 2004; Chouet et al., 2003). See Stähler & Sigloch (2014) for a study that inverted for hypocentral coordinates, origin time, and source time function in addition to the moment tensor parameters.

It is difficult to constrain the source type for events as small as those in our study (M_w = 0.3–2.8). This makes uncertainty estimation important. We have recently introduced a confidence parameter for moment tensors and have applied it to a set of 21 earthquakes that we assumed to be double couple moment tensors (Tape & Tape, 2016; Silwal & Tape, 2016). Our current plan is to adapt our full moment tensor approach to estimate confidence parameters.

2.6.3 Influence of first-motion polarities

Some of our rationale for using first-motion polarities was discussed in Section 2.3.3. Here we review some results and discuss possible shortcomings. Figure 2.9 showed that by fitting P waveforms (and surface waves, when available), we obtained moment tensor solutions whose first-motion polarities matched most or all of the observed polarities ($n(M_0) \approx 0$). In our study we chose to constrain the waveform-fitting moment tensor solutions to also fit all first-motion polarities. This choice has the effect of increasing the influence of small-amplitude P waves that nevertheless have a discernible first-motion polarity. Without the inclusion of first-motion polarities, the direct waveform difference will be biased toward the highest amplitude P waves.

First-motion polarities alone determine a subset of allowable moment tensors, which in turn can be represented on a source type plot such as the lune in Figure 2.6b. The shape of the region $n(\Lambda) = 0$ depends on the signs of the first-motion polarities, the source–station geometry, and the ray take-off angles, which in turn are influenced by the seismic velocity model. Using a different velocity model will change the positions of piercing points on the focal sphere and will therefore change the set of allowable moment tensor solutions. Having more stations and having uniformly distributed stations (with respect to the source) will result in a smaller allowable region of moment tensor source types.

In this study our approach has been to first carefully identify all first-motion polarity measurements. We then only consider moment tensors whose predicted first-motion polarities all match the observations ($n(M) = 0$, Eq. 2.5). A more flexible approach would allow for a weight (or uncertainty) to be assigned to each first-motion polarity measurement, and then the misfit function would balance two terms, one for waveform misfit and one for polarity misfit.

There are two things that first-motion polarities alone cannot provide: (1) magnitude and (2) a unique minimum of a misfit function. These can be obtained using amplitude measurements or

waveform differences. We use waveform differences to obtain a moment tensor solution M_0 with minimum waveform misfit and with magnitude M_w. Plots of the misfit function on the lune reveal the region of plausible moment tensor solutions about the global minimum solution M_0.

2.6.4 Physical models for moment tensors

Our moment tensor catalog in Figure 2.11b provides a starting point for interpreting physical source models for the full moment tensors. We discuss our moment tensor solutions in the context of the classical model introduced by Aki & Richards (1980) and discussed in Dufumier & Rivera (1997); Minson et al. (2007); Tape & Tape (2013).

Tape & Tape (2013) reviewed two perspectives on the classical model: (1) a single-process model as an oblique crack and (2) a two-process model involving the sum of a crack and a double couple. We refer to (1) as the classical model, following Dufumier & Rivera (1997), and (2) as the crack-plus-double-couple (CDC) model, following Minson et al. (2007). Each model has a pair of variables that is used to characterize the source type (Tape & Tape, 2013).

Our moment tensor catalog represented by the classical model is presented in Figure 2.16ab. The two parameters representing the source type in the classical model are the Poisson ratio ν and the angle $\alpha = \angle(\mathbf{N}, \mathbf{S})$ between the normal vector and slip vector. The angle α is a function of lune longitude, with $\alpha = 90^\circ$ corresponding to $\gamma = 0^\circ$. For our 63 events, α is centered on 90° and ranges from 30° to 150°, with a couple events near the tensional crack endmember of $\alpha = 0^\circ$ (Figure 2.16b).

Mathematically any value of ν is possible, but the physically permissible range is $-1 \leq \nu < 0.5$, which is plotted in Figure 2.16a. Previous studies have found that Poisson ratios for orogenic belts range between 0.18–0.35 (Zandt & Ammon, 1995) and for the crust beneath the Altiplano they average 0.25 (Zandt et al., 1996). A small portion of our events (8/63) have Poisson ratios within a reasonable range of $\nu = 0.15$–0.35. Results from other published studies imply Poisson ratios with similar wide spreads—both outside a reasonable range and outside the permissible range. This prompted Tape & Tape (2013) to conclude that either (1) the classical model did not apply to the situation at hand or (2) the published moment tensors (and predicted Poisson ratios) had large uncertainties.

The CDC model characterizes any moment tensor as a sum of a crack moment tensor and a double couple moment tensor whose fault plane is the same as that of the crack. Two points are worth mentioning. First, the crack tensor and double couple tensor do not have the same eigenframe, so one cannot discuss the 'decomposition' in terms of eigenvalues alone. Second, two sums are possible for each moment tensor (e.g., Tape & Tape, 2012). Our moment tensor catalog represented by the CDC model is presented in Figure 2.16cd. The two coordinates describing the

source type for the CDC model are the azimuth ϕ on the lune and the crack fraction ζ (Tape & Tape, 2013).

The variation of ζ (Figure 2.16d) reveals that most of our events—if interpreted as a sum of a double couple and a crack—have significant crack fraction (Figure 2.16d). It is useful to consider the endmembers of the CDC model. If all events clustered near $\zeta = 0°$, then we would likely invoke a single-process model of shear faulting (with no opening or closing); if all events clustered near $\zeta = 90°$, then we might invoke a single-process model of tensional (or compressional) cracks. In the context of the CDC model, our events imply that contributions from the double couple and the crack are comparable in size.

Instead of interpreting M_0 in terms of the classical model or CDC model, one might choose to find the minimum misfit for an 'endmember' source type (Chiang et al., 2014). Figure A.24 summarizes results for the example event if we constrain the solution to be a double couple (Fig. A.24b), a tensional crack (Fig. A.24c), or a compressional crack (Fig. A.24d). For this event, there is at least one moment tensor for each of these subsets that satisfies $n(M) = 0$ (Eq. 2.5). This shows that, for source-station geometries such as ours, something more than polarities alone—e.g., measurements of waveform differences—is needed to constrain the source type. If considering the full moment tensor space, the minimum of the waveform misfit function occurs at M_0, which has a source type at $(\gamma = 5°, \delta = -13°)$. However it is possible that one could have additional information that would warrant constraining the moment tensor inversion to a specific source type. For example, one might have microseismicity at depth or GPS measurements at the surface that are consistent with pure opening at depth.

2.7 Conclusion

1. We present a compilation of 63 full moment tensors for events at Uturuncu volcano, Bolivia, for the time period of the PLUTONS array (2010-04-12 to 2012-03-09). Our catalog represents the complete set of events for which we could obtain reliable moment tensor solutions. For each event we used as many waveform measurements (both P waves and surface waves) and first-motion measurements as possible.

   In the context of the published literature (Table 2.1), our catalog of moment tensors is large, the events we analyze are small ($M_w = 0.3$–2.8), the waveforms are high frequency. We present the variations in misfit function over the space of source types for each event.

2. We characterize three subsets of moment tensors within our catalog. One subset, located close to the volcano, contains 6 events with isotropic components whose first-motion polarities exclude the possibility of a double-couple mechanism.

3. Our findings of positively isotropic events are in agreement with other studies of full moment tensors in volcanic and geothermal settings (Figure 2.11b). As noted in Tape & Tape (2013), the large spread in source types of previously published events could be explained by a multiple-process model. Alternatively, they could be explained by the classical model, whereby the full moment tensor solutions have large uncertainties in the space of source types (i.e., on the lune). Most previous studies did not provide uncertainty estimates, making interpretation challenging.

   Our plots of misfit $\Phi(\Lambda)$ on the lune (Figure 2.6) are a step toward uncertainty estimation. They show the range of permissible source types. Considering this range, we conclude that the classical model remains a possibility (Section 2.6.4).

4. Full moment tensor inversion of P waveforms at the frequencies used in this study (2–10 Hz) is a delicate procedure, especially when the velocity structure is not well known. We would expect more reliable solutions in a setting with larger magnitudes (say, up to M_w 4). In that case, lower frequency waves, including surface waves, could be used within full moment tensor inversions. Solutions for larger events could help determine the reliability of the solutions for smaller events, for which fewer waveforms are available.

Table 2.1: Examples of published studies on full moment tensor inversions. See Table 2.2 for explanation of columns. See Section 2.2 for discussion.

study	events	stations	magnitude range	frequency range (Hz)	details for moment tensor inversion								UNC	F2.11b
					FMP	BW	SW	WD	AR	1D/3D	GS	L		
Alvizuri & Tape (2016)	63	5–23	0.3 to 2.8	0.25–10	Y	Y	Y	Y	–	1D	Y	–	B	Y
Pesicek et al. (2016)	9												C	–
Dammeier et al. (2015)	2												C	–
Boyd et al. (2015)	53	39	3.29 to 4.72	0.02–0.10	Y	–	Y	Y	–	1D	Y	–	B	Y
Dreger et al. (2012)	828								–	1D				
Ross et al. (2015)	7	71–126	4.2 to 5.4	0.02–0.3	–	Y	Y	Y	–	1D	Y	–	C	–
Aso & Ide (2014)	38	5	1.2 to 2.1	≤ 10	–	Y	–	Y	–	1D	Y	Y	–	–
Stähler & Sigloch (2014)	1	17–41	5.7	–	–	Y	–	Y	–	1D	–	–	A	–
Stierle et al. (2014)	33	35	2.5 to 4.3	0.5–35	–	Y	–	Y	–	1D	Y	–	C	–
Chiang et al. (2014)	3	3–4	5.21 to 5.25	0.01–0.08	Y	–	Y	Y	–	1D	Y	–	B	–
Guilhem et al. (2014)	15	30	3.31 to 4.43	0.5–2.5	Y	Y	–	Y	–	1D	–	Y	B	–
Nayak & Dreger (2014)	62	5	1.3 to 1.6	0.1–0.2	Y	–	Y	Y	–	1D	Y	–	B	–
Pesicek et al. (2012)	7	10–12	1.0 to 2.3	2–10	Y	–	–	–	Y	3D	Y	Y	C	Y
Ford et al. (2012)	1	8	3.5	0.02–0.1	–	–	Y	Y	–	1D	–	Y	B	–
Vavryčuk (2011)	71	7–22	≤ 3.7	1–35	–	Y	–	–	–	1D	–	Y	C	Y
Eisner et al. (2010)	4	980	0.4 to 0.7	–	–	–	–	–	–	1D	–	–	–	–
Baig & Urbancic (2010)	147	–	–	–	–	–	–	–	–	–	–	–	–	–
Julian et al. (2010)	38	36	0.3 to 2.6	≤ 5	Y	–	–	–	Y	–	–	Y	–	–
Walter et al. (2010)	14	24		20–70	–	Y	–	Y	–	1D/3D	Y	Y	–	–
Ford et al. (2010)	2	6–8	4.2 to 4.8	0.02–0.1	–	–	Y	Y	–	1D	Y	–	B	–
Ford et al. (2009)	32	16–52	3.3 to 5.4	0.02–0.1	–	–	Y	–	–	1D	–	Y	C	–
Šilený et al. (2009)	24	8	-2 to -1.4	–	Y	Y	–	–	–	1D	–	Y	–	–
Walter et al. (2009)	13	–	-2.6 to -1.3	5–60	–	Y	–	Y	–	1D	Y	–	–	–
Minson & Dreger (2008)	18	9	3.7 to 6.5	0.02–0.05	–	–	Y	–	–	1D	Y	–	–	Y
Šilený & Milev (2008)	5	12	2.0 to 3.0	≥ 3	–	–	–	Y	–	1D	–	Y	C	–
Minson et al. (2007)	13	3–9	4.5 to 6.2	≤ 0.05	–	–	Y	–	–	1D	Y	Y	–	Y
Šilený & Milev (2006)	5	16	–	4.5–20	–	Y	–	–	Y	–	–	–	C	–
Foulger et al. (2004)	26	65	0.4 to 3.1	≤ 5	Y	–	–	–	Y	1D	–	Y	–	Y
Horálek et al. (2002)	70	6–9	0.3 to 3.0	≥ 0.5	–	Y	–	–	Y	1D	–	Y	–	–
Vavryčuk (2001)	36	9	0.5 to 3.0	–	–	–	–	–	–	–	–	–	–	Y
Miller et al. (1998b)	70	30	–	≤ 5	Y	Y	–	–	Y	3D	–	Y	–	–
Dahm & Brandsdóttir (1997)	15	4–21	1.1 to 2.3	1.5–7.0	Y	Y	–	–	Y	–	–	Y	–	–

Table 2.2: Explanation of columns for Table 2.1.

FMP	used first-motion polarities
BW	used body waves
SW	used surface waves
WD	used waveform difference
AR	used amplitude ratios
1D/3D	computed Green's function's using 1D or 3D structural model
GS	used grid search
L	used linearized inversion
UNC	addressed uncertainties [A] posterior probability density over moment tensor (or eigenvalue) space [B] show misfit function over full eigenvalue space [C] approximate posterior probability density over moment tensor (or eigenvalue) space
F2.11	data plotted in Figure 2.11

Table 2.3: Moment tensor results for the example event for different subsets of data and different allowable subsets of moment tensors. Each row lists the optimal moment tensor solution as six parameters: magnitude M_w, lune longitude γ, lune latitude δ, strike κ, dip θ, and rake σ. The percent variance reduction is *VR*. The weights (10, 01, or 00) for the waveform components for each inversion are listed for P-wave vertical (PV), P-wave radial (PR), and surface waves (Surf). The number of first motion polarities used in the inversion are listed under Npol. The label 'subset' denotes whether the moment tensor inversion assumes the full moment tensor space ('–') or is restricted to specific physical models by setting $\gamma = 0^\circ$ and $\delta = 0^\circ$ for the double-couple (DC), $\gamma = -30^\circ$ for tensional crack (C+), and $\gamma = 30^\circ$ for compressional crack (C–). Figures associated with each inversion are listed in the last two columns.

M_w	γ	δ	κ	θ	σ	*VR*	PV	PR	Surf	Npol	subset	figures	
2.8	10	−10	150	76	−75	22.1	10	01	10	11	–	2.6, 2.7a	2.4, A.8
2.8	5	−13	145	73	−70	22.4	10	01	10	–	–	2.7b	A.9
2.9	20	−23	145	66	−80	30.9	10	01	00	11	–	2.7c	A.10
3.0	20	−26	130	58	−80	32.8	10	01	00	–	–	2.7d	A.11
3.0	20	−23	145	66	−80	47.6	10	00	00	11	–	2.8a	A.12
2.2	0	0	10	5	−75	15.2	00	01	00	11	–	2.8b	A.13
2.8	15	3	150	73	−55	21.7	00	00	10	11	–	2.8c	A.14
2.7	[0]	[0]	170	90	−85	21.2	10	01	00	11	DC	A.24b	A.21
2.7	[−30]	34	50	50	75	11.4	10	01	00	11	C+	A.24c	A.22
3.1	[30]	−30	345	35	−90	24.2	10	01	00	11	C–	A.24d	A.23

Table 2.4: Catalog of full moment tensors computed in this study. The moment tensor parameters are magnitude M_w, lune longitude γ, lune latitude δ, strike κ, dip θ, and rake σ. Variance reduction is VR. The origin time, hypocenter, and magnitude M_{KW} are from Keyson & West (2013). A text file for our catalog is available as Table A.2.

origin time	longitude	latitude	depth	M_{KW}	M_w	γ	δ	κ	θ	σ	Npol	VR
2010-05-16 06:34:54.464	−67.18560	−22.26000	0.6	2.44	2.80	10	−10	150	76	−75	11	22
2010-05-16 08:56:11.725	−67.18490	−22.26290	5.1	2.21	2.60	−20	23	355	73	70	11	21
2010-06-01 07:36:04.690	−67.14330	−22.40580	1.1	1.14	1.80	5	−3	35	20	10	10	48
2010-06-01 22:13:52.679	−67.15120	−22.41310	4.8	1.28	2.00	10	−10	25	20	−5	11	38
2010-09-30 09:52:32.848	−67.09720	−22.46800	4.5	1.02	1.60	−15	30	15	73	90	5	43
2010-09-30 09:54:13.030	−67.09670	−22.46630	4.6	1.18	1.90	20	−10	30	20	−35	6	66
2010-09-30 09:56:12.039	−67.09730	−22.46450	4.5	1.48	2.10	20	−6	40	20	−30	6	67
2010-09-30 10:25:01.621	−67.10100	−22.45460	4.9	1.31	1.90	15	−3	50	20	−15	6	54
2010-09-30 11:45:31.523	−67.09330	−22.45600	4.2	1.12	1.80	15	−3	50	20	−20	6	66
2010-09-30 15:57:02.647	−67.09750	−22.45440	4.4	2.17	2.50	10	3	45	20	−40	6	53
2010-09-30 16:39:13.172	−67.11020	−22.48550	4.8	1.18	2.00	15	−10	45	40	−55	5	71
2010-09-30 17:23:33.129	−67.10050	−22.46470	4.7	1.69	2.20	5	6	75	28	−35	6	56
2010-09-30 18:35:17.772	−67.09560	−22.45960	4.5	1.36	1.80	5	23	40	5	−75	6	65
2010-09-30 21:59:12.435	−67.11050	−22.46970	5.4	1.99	2.40	5	10	75	20	−35	6	51
2010-10-01 11:10:55.009	−67.10680	−22.45200	4.6	1.98	2.40	25	−3	25	20	−40	6	54
2010-10-01 11:12:42.832	−67.11030	−22.45780	5.4	1.58	2.20	25	−6	45	28	−30	6	60
2010-10-05 03:21:24.419	−67.10110	−22.47510	4.1	1.45	2.00	5	−16	15	20	−40	7	50
2011-01-27 03:09:47.813	−67.20520	−22.41470	4.4	1.02	1.80	−15	30	95	76	90	12	57
2011-04-25 03:50:05.648	−67.15960	−22.30250	3.8	0.16	1.00	−15	30	255	45	80	11	38
2011-04-25 04:47:54.697	−67.15750	−22.30580	4.2	0.16	0.70	10	38	165	28	−90	19	20
2011-04-29 19:15:51.352	−67.20790	−22.25480	4.2	0.96	1.50	−30	34	150	81	−0	23	25
2011-04-30 15:56:47.801	−67.26760	−22.27770	4.2	0.48	1.30	−15	46	160	62	60	16	32
2011-05-01 12:59:10.539	−67.22360	−22.32290	4.6	0.34	1.10	−10	38	200	40	−40	18	28
2011-05-07 02:36:04.488	−67.09170	−22.53560	4.2	0.23	1.10	−10	16	5	66	−60	6	46
2011-05-28 02:37:26.768	−67.16800	−22.34170	9.8	0.29	0.50	−15	13	30	69	−35	11	33
2011-05-28 02:42:24.281	−67.16780	−22.34500	4.8	0.01	0.50	−15	13	5	58	−70	6	49
2011-05-28 02:52:38.269	−67.16060	−22.33740	4.7	0.07	0.90	−0	23	15	50	−90	15	34
2011-05-28 02:53:39.982	−67.16600	−22.34130	5.0	0.03	0.70	−5	34	10	62	−90	17	33
2011-05-28 03:35:23.921	−67.17050	−22.34610	6.2	0.01	0.60	5	26	210	87	10	16	29
2011-05-28 06:18:23.523	−67.18730	−22.23570	4.0	0.16	1.20	25	−19	30	70	90	6	55
2011-05-31 12:48:24.834	−67.25680	−22.19370	4.9	0.28	0.60	10	23	255	54	85	7	15
2011-06-06 07:02:01.270	−67.30960	−22.27640	2.5	0.19	1.20	−20	38	260	28	30	7	14
2011-06-22 02:33:24.299	−67.23240	−22.33870	4.2	0.18	0.60	10	38	15	83	−0	18	17
2011-06-30 10:42:59.611	−67.00150	−22.49720	4.1	−0.00	1.00	−10	19	45	28	−25	7	25
2011-07-08 14:58:21.435	−67.16500	−22.29920	3.9	0.00	0.90	−15	19	90	40	75	11	34
2011-08-02 03:00:42.673	−67.24990	−22.16650	12.0	0.17	1.10	−0	3	60	87	20	6	50
2011-08-08 10:38:42.458	−67.16720	−22.23130	13.3	0.25	0.70	−10	38	55	35	85	16	30
2011-08-09 03:21:09.852	−67.16970	−22.23770	5.8	0.02	0.70	−5	34	50	35	70	11	36
2011-08-10 03:18:14.398	−67.20560	−22.28700	4.8	0.22	0.90	5	3	225	50	−85	15	22
2011-08-10 03:18:38.705	−67.20610	−22.28890	4.5	0.15	1.00	20	10	105	58	−85	9	35
2011-08-17 00:43:17.677	−67.24330	−22.12260	4.5	0.15	0.90	−20	16	185	76	75	10	28
2011-08-23 07:26:42.794	−67.16570	−22.30830	4.3	0.10	0.80	−10	46	240	62	80	15	30
2011-08-23 07:27:00.783	−67.16980	−22.30720	4.2	0.87	1.50	−25	30	205	50	−30	21	24
2011-08-23 20:21:12.670	−67.19860	−22.26820	4.9	0.53	1.30	0	−13	110	45	−60	8	38
2011-08-29 07:14:01.139	−67.13580	−22.26970	4.2	0.01	0.80	15	19	350	28	45	7	55
2011-09-27 18:14:40.559	−67.23870	−22.19590	4.5	0.13	0.90	25	34	15	50	25	11	30
2011-09-27 21:10:49.558	−67.23990	−22.19600	4.8	0.29	1.00	5	3	20	90	5	12	36
2011-10-25 03:07:50.754	−67.13140	−22.28540	5.0	0.13	0.70	−10	34	0	76	10	7	46
2011-10-28 07:25:30.002	−67.12560	−22.50580	5.0	0.43	0.60	5	13	205	69	−55	10	37
2011-11-11 11:02:21.636	−67.24970	−22.51810	4.5	0.29	0.90	20	−13	225	87	85	7	58
2011-12-09 14:34:54.837	−67.16660	−22.29270	3.8	0.20	1.20	−15	26	60	58	65	7	48
2011-12-22 23:16:21.860	−67.17870	−22.29980	4.3	0.33	0.70	−20	23	270	40	−10	11	14
2011-12-22 23:17:08.220	−67.18440	−22.29550	4.5	0.43	0.80	−10	26	350	80	−85	11	7
2011-12-24 03:53:32.713	−67.25020	−22.37750	4.9	0.07	0.90	15	30	60	40	85	13	39
2011-12-24 06:41:28.067	−67.17930	−22.24090	4.7	0.47	1.00	5	30	330	54	−60	20	14
2011-12-24 06:43:11.431	−67.17250	−22.23990	4.8	−0.00	0.80	−30	34	162	80	−30	9	18
2011-12-24 06:49:06.473	−67.17940	−22.23940	4.7	0.11	0.80	0	42	30	40	65	15	23
2011-12-24 17:29:41.331	−67.17490	−22.23270	5.5	0.29	1.00	−5	23	85	32	90	6	37
2012-01-07 13:38:00.237	−67.16120	−22.29760	4.5	0.27	1.20	−20	10	105	40	75	7	46
2012-01-08 08:27:20.474	−67.16020	−22.29910	4.5	0.14	0.70	15	6	335	66	−80	17	31
2012-01-26 20:19:37.383	−67.22030	−22.27800	4.6	0.05	0.70	−0	16	120	40	−15	10	32
2012-02-02 12:58:16.847	−67.02280	−22.38860	8.0	0.42	0.70	−20	10	15	50	−50	8	53
2012-02-04 02:58:00.727	−67.06570	−22.40470	10.1	0.06	0.80	5	16	180	76	20	11	44

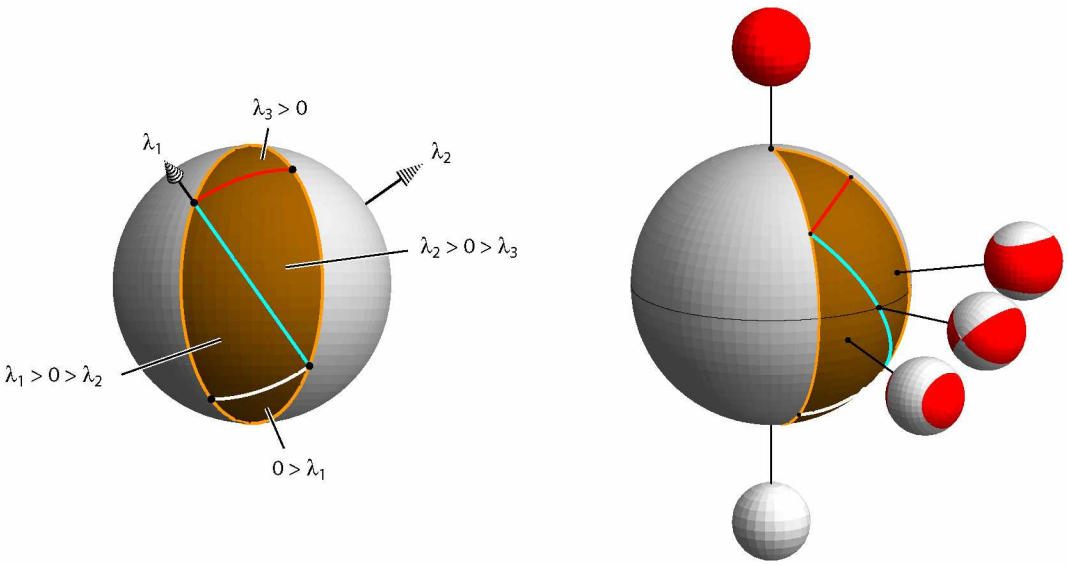

Figure 2.1: Four regimes for moment tensors, depicted on the fundamental lune. See Tape & Tape (2013, Fig. S1). The lune is the surface of normalized moment tensor eigenvalue triples $\Lambda = (\lambda_1, \lambda_2, \lambda_3)$, with $\lambda_1 \geq \lambda_2 \geq \lambda_3$. The three arcs $\lambda_3 = 0$ (red), $\lambda_2 = 0$ (blue), and $\lambda_1 = 0$ (white) divide the lune into four regions. Above $\lambda_3 = 0$, beachballs are all red ($\lambda_3 > 0$). Above and to the right of the arc $\lambda_2 = 0$, moment tensor beachballs have red bands and white caps ($\lambda_2 > 0 > \lambda_3$). Below and to the left of it they have white bands and red caps ($\lambda_1 > 0 > \lambda_2$). Below the arc $\lambda_1 = 0$, beachballs are all white ($\lambda_1 < 0$). Double couple moment tensors are at the center of the lune, where $\Lambda = (1, 0, -1)$. (Although points on the lune have unit norm, we often give them as unnormalized directions; this $(1, 0, -1)$ instead of $(1, 0, -1)/\sqrt{2}$.)

Figure 2.2: [FOLLOWING PAGE] Stations and events near Uturuncu volcano. (a) Map showing stations and all events with depths less than 60 km in the Uturuncu catalog (Keyson & West, 2013). Our region of interest is inside the station array and ranges between longitudes -67.4° and -66.9° and between latitudes -22.6° and -22.1°. There are 421 events in this region, 63 of which (red circles) meet our selection criteria in this study (Section 2.3.1). Top and right plots show the seismicity projected onto vertical cross sections. The histogram shows the distribution of events with depth; it reveals a predominance of event depths near 5 km. (b) (top) Number of PLUTONS stations active as a function of time. The vertical lines mark the time period of events considered in our study, 2010-04-12 to 2012-03-09. (bottom) Events as a function of time; the red circles are the 63 events in our study. (c) Frequency-magnitude distribution for 421 crustal events in the region of interest. The relationship implies the occurrence of one $M \geq 2.5$ earthquakes per two years in this region.

(a)

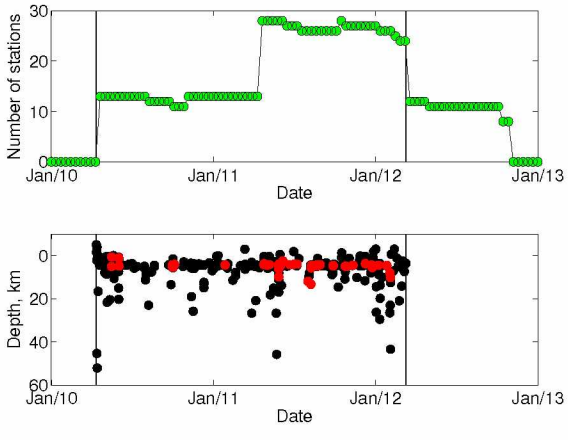

(b)

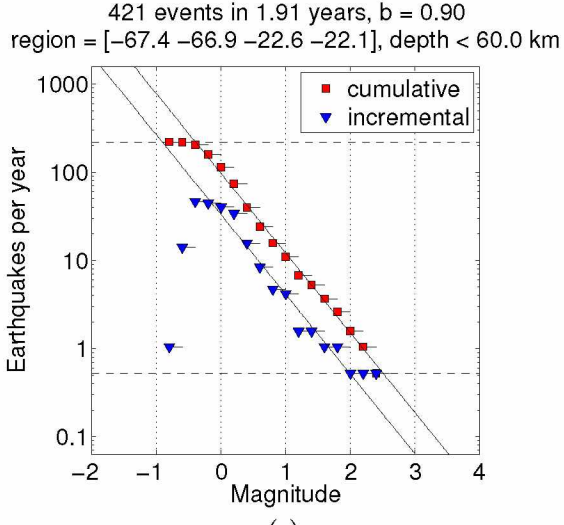

(c)

Figure 2.2

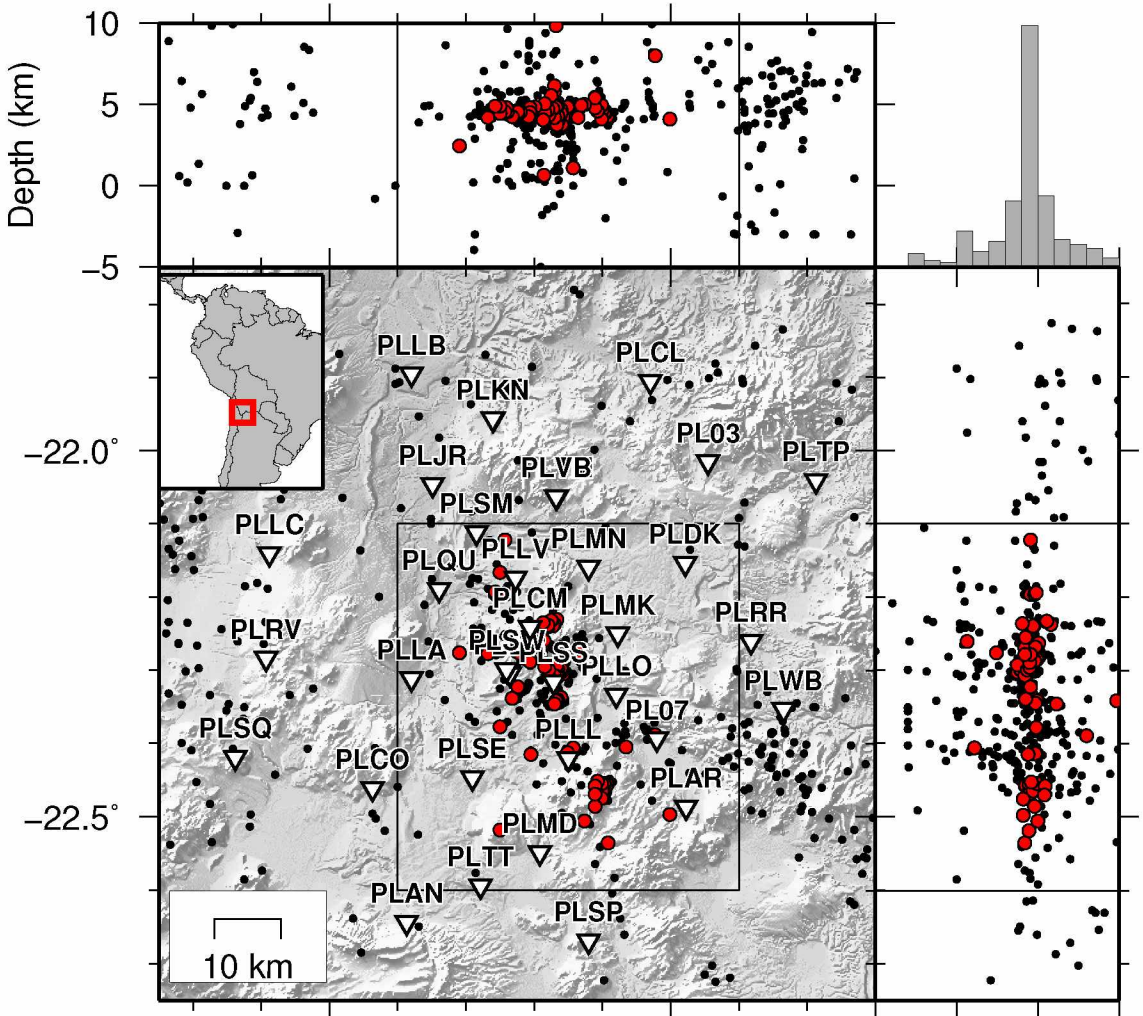
Depth (km)
10
5
0
−5
−22.0˚
−22.5˚
PLLB
PLCL
PLKN
PL03
PLTP
PLJR
PLVB
PLSM
PLLC
PLLV
PLMN
PLDK
PLQU
PLCM
PLMK
PLRR
PLRV
PLLA
PLSW
PLSS
PLLO
PLWB
PL07
PLSQ
PLLL
PLCO
PLSE
PLAR
PLMD
PLTT
PLAN
PLSP
10 km

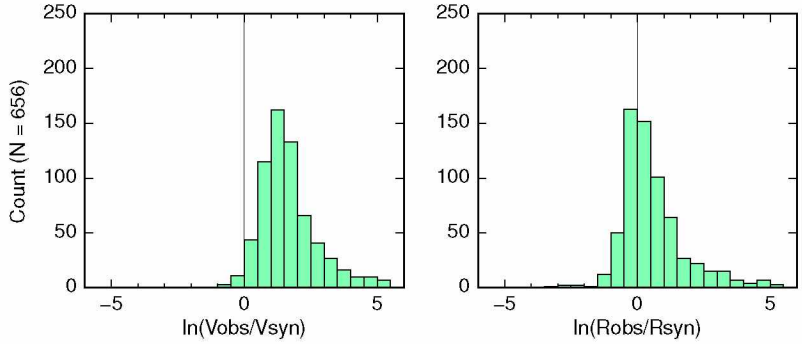

(a) weights P01 R01 S01

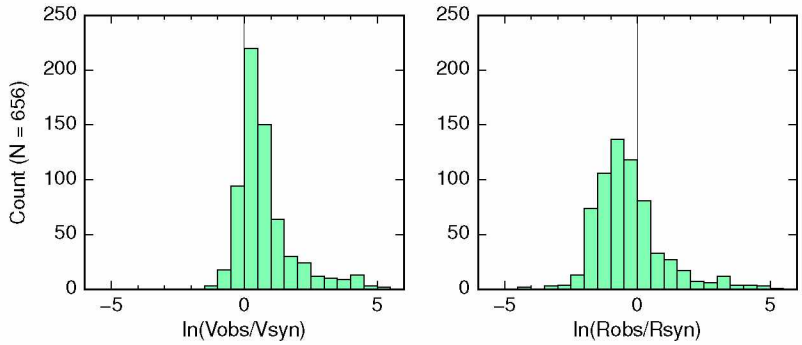

(b) weights P10 R01 S10

Figure 2.3: P wave amplitude ratios, $\ln(A_{\text{obs}}/A_{\text{syn}})$, for all 656 windows for all 63 events and for two different sets of weights. (a) Amplitude ratios for moment tensor inversions using equal weights for the vertical component P wave, the radial component P wave, and the surface waves. On the left is the amplitude ratio for the vertical component P wave; on the right is the ratio for the radial component. With this choice of weights, the histogram for the radial component is approximately centered on zero, whereas the histogram for the vertical component is skewed toward positive values, indicating that the vertical component synthetic amplitudes are small relative to observations. (b) Same as (a), but for this set of moment tensor inversions the radial component was down-weighted relative to the vertical component P wave and the surface waves. For these weights, we see that the vertical component P wave amplitude ratios are centered on zero, whereas the radial component ratios are skewed to negative values, indicating that the radial synthetic amplitudes are larger than the observations. Note that the moment tensor solutions in (b) are not identical to those in (a), since a different misfit function has been used. Figures A.4–A.7 provide an extended analysis of amplitude ratios.

Figure 2.4: [FOLLOWING PAGE] Moment tensor solution M_0 and waveform comparisons for the example event (20100516063454464) in this study. Each column is a different section of the three-component waveform: PV = vertical component P wave, PR = radial component P wave, SurfV = vertical component Rayleigh wave, SurfR = radial component Rayleigh wave, SurfT = transverse component Love wave. The stations are ordered by increasing epicentral distance from the top row. The observed waveforms are plotted in black, the synthetic waveforms are plotted in red. The body waves are filtered 2–10 Hz, and the surface waves are filtered 0.25–0.50 Hz (2–4 s). Each observed and synthetic waveform is scaled to fill the plotting window; Figure A.8 shows the same record section with absolute amplitudes. The numbers below each station name are, from top to bottom, the station epicentral distance, the station azimuth, and the sign of the first-motion polarity (1 is upward, -1 is downward). The number in parentheses is the source amplitude factor for M_0 at each station. The four numbers below each pair of waveforms are, from top to bottom, (1) the cross-correlation time shift $\Delta T = T_{\mathrm{obs}} - T_{\mathrm{syn}}$ required for matching the synthetics $s(t)$ with the data $u(t)$ (a positive time-shift means that the synthetics arrive earlier than the data), (2) the maximum cross-correlation percentage between $u(t)$ and $s(t - \Delta T)$, (3) the percentage of the total misfit, and (4) the amplitude ratio $\ln(A_{\mathrm{obs}}/A_{\mathrm{syn}})$. See Alvizuri (2015) for a description of the header lines.

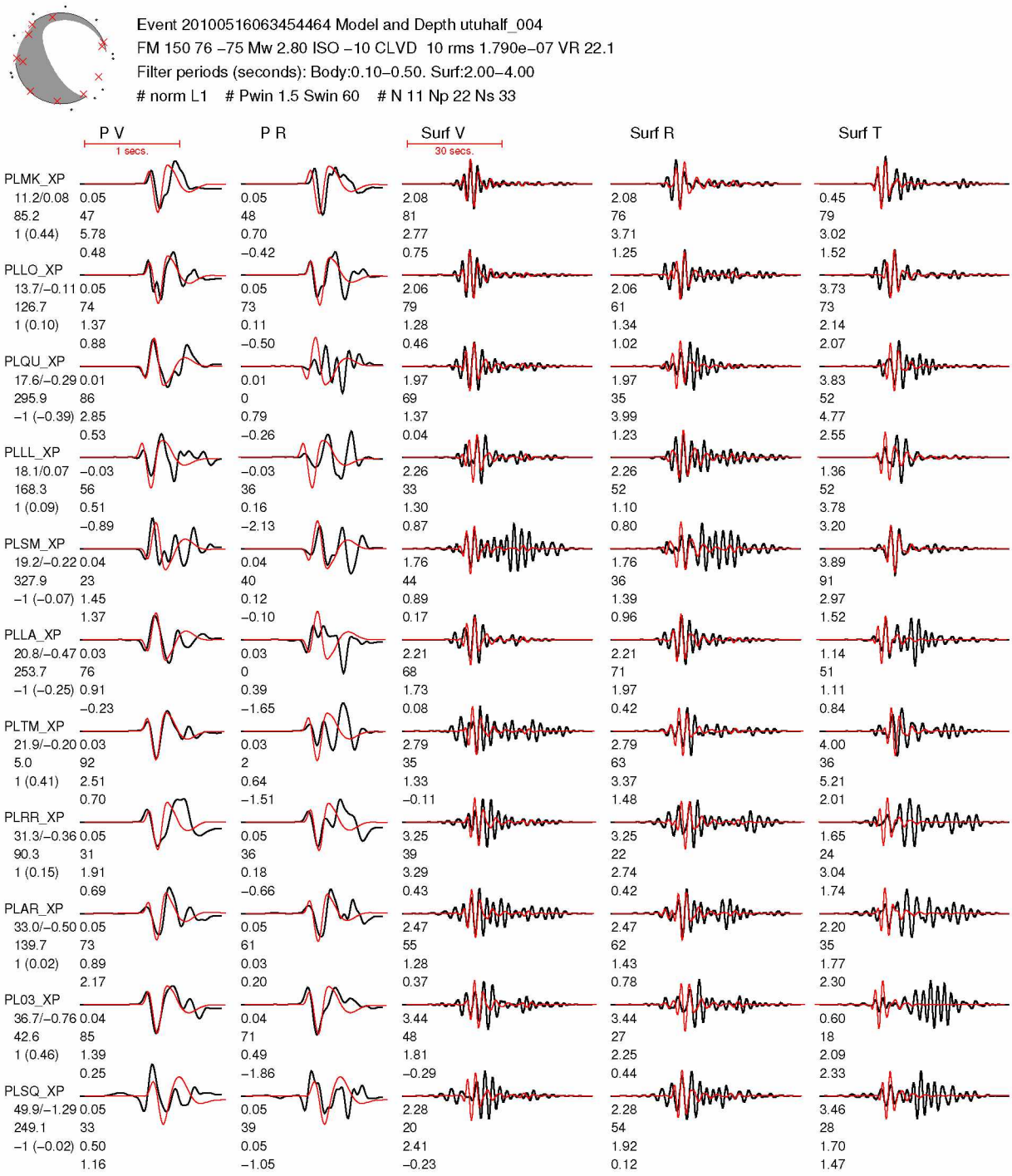
Event 20100516063454464 Model and Depth utuhalf_004
FM 150 76 −75 Mw 2.80 ISO −10 CLVD 10 rms 1.790e−07 VR 22.1
Filter periods (seconds): Body:0.10−0.50. Surf:2.00−4.00
norm L1 # Pwin 1.5 Swin 60 # N 11 Np 22 Ns 33
P V
1 secs.
P R
Surf V
30 secs.
Surf R
Surf T
PLMK_XP
11.2/0.08 0.05 0.48
85.2 47 5.78
1 (0.44) 0.05 0.70 2.08 2.08 0.45
48 −0.42 81 76 79
2.77 3.71 3.02
0.75 1.25 1.52
PLLO_XP
13.7/−0.11 0.05 0.88
126.7 74 1.37
1 (0.10) 0.05 0.11 2.06 2.06 3.73
73 −0.50 79 61 73
1.28 1.34 2.14
0.46 1.02 2.07
PLQU_XP
17.6/−0.29 0.01 0.53
295.9 86 2.85
−1 (−0.39) 0.01 0.79 1.97 1.97 3.83
0 −0.26 69 35 52
1.37 3.99 4.77
0.04 1.23 2.55
PLLL_XP
18.1/0.07 −0.03 −0.89
168.3 56 0.51
1 (0.09) −0.03 0.16 2.26 2.26 1.36
36 −2.13 33 52 52
1.30 1.10 3.78
0.87 0.80 3.20
PLSM_XP
19.2/−0.22 0.04 1.37
327.9 23 1.45
−1 (−0.07) 0.04 0.12 1.76 1.76 3.89
40 −0.10 44 36 91
0.89 1.39 2.97
0.17 0.96 1.52
PLLA_XP
20.8/−0.47 0.03 −0.23
253.7 76 0.91
−1 (−0.25) 0.03 0.39 2.21 2.21 1.14
0 −1.65 68 71 51
1.73 1.97 1.11
0.08 0.42 0.84
PLTM_XP
21.9/−0.20 0.03 0.70
5.0 92 2.51
1 (0.41) 0.03 0.64 2.79 2.79 4.00
2 −1.51 35 63 36
1.33 3.37 5.21
−0.11 1.48 2.01
PLRR_XP
31.3/−0.36 0.05 0.69
90.3 31 1.91
1 (0.15) 0.05 0.18 3.25 3.25 1.65
36 −0.66 39 22 24
3.29 2.74 3.04
0.43 0.42 1.74
PLAR_XP
33.0/−0.50 0.05 2.17
139.7 73 0.89
1 (0.02) 0.05 0.03 2.47 2.47 2.20
61 0.20 55 62 35
1.28 1.43 1.77
0.37 0.78 2.30
PL03_XP
36.7/−0.76 0.04 0.25
42.6 85 1.39
1 (0.46) 0.04 0.49 3.44 3.44 0.60
71 −1.86 48 27 18
1.81 2.25 2.09
−0.29 0.44 2.33
PLSQ_XP
49.9/−1.29 0.05 1.16
249.1 33 0.50
−1 (−0.02) 0.05 0.05 2.28 2.28 3.46
39 −1.05 20 54 28
2.41 1.92 1.70
−0.23 0.12 1.47

Figure 2.4

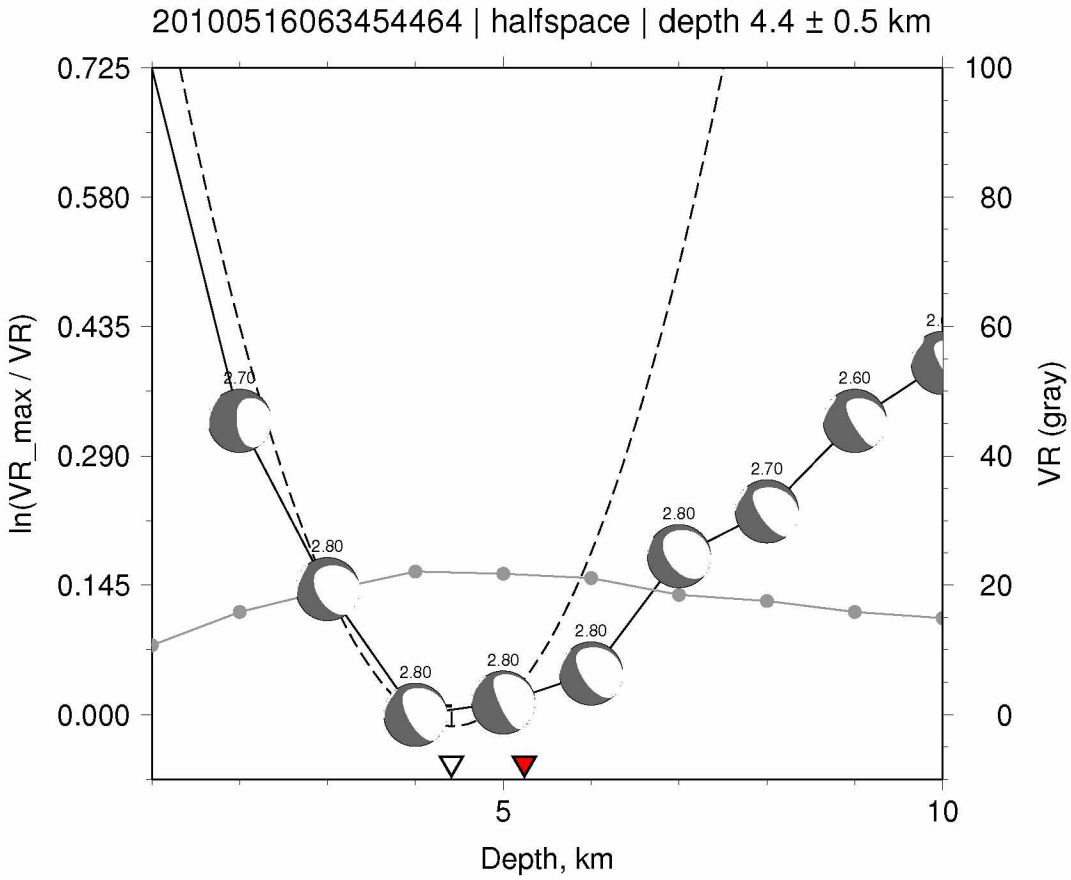

Figure 2.5: Grid search for the best-fitting depth for the example event (Figure 2.4). The red arrow marks the catalog depth (0.6 km; 5.2 km below the surface), and the white arrow marks the depth obtained from our moment tensor inversion (−0.2 km; 4.4 km below the surface). The gray line with solid circles is the variance reduction VR for the moment tensor solution obtained at that particular depth (scale at right). The best solution occurs at the maximum in variance reduction $VR_{\max} = 22.1$. The beachballs are plotted at the value of $\ln(VR_{\max}/VR)$, which gives the variance reduction relative to the maximum (scale at left). The orientation and magnitude are free to change for each depth. The black dashed line is the best-fitting parabola, which is used for estimating the uncertainty in depth; here the best-fitting depth is -0.2 ± 0.5 km, which is 4.4 ± 0.5 km below the surface.

Figure 2.6: [FOLLOWING PAGE] Full moment tensor misfit summary for the example event. For details, see Section 2.4. (a) Map of source location (red star) and stations used in the inversion for this event. The station is colored blue if the observed first-motion polarity on the vertical component is up (compression) and white if it is down (dilatation). (b) Contour plot of the polarity misfit on the lune. Not to be confused with the waveform misfit, the polarity misfit $n(M)$ (Eq. 2.5) for a moment tensor M is the number of stations where the observed first-motion polarity differs from the polarity predicted from M. The polarity misfit $n(\Lambda)$ (Eq. 2.6) at a point Λ on the lune is then the minimum of $n(M)$ for moment tensors M having source type Λ. At each point Λ in the region where $n(\Lambda) = 0$ (blue), there is therefore a moment tensor M with source type Λ that has correct polarities, that is, polarities that match the observed polarities at all 11 stations. (c) Contour plot of the variance reduction $VR(\Lambda)$. The variance reduction $VR(\Lambda)$ at a point Λ is the maximum variance reduction $VR(M)$ for moment tensors M that have source type Λ and that have correct polarities. (Compare Eq. 2.7, which is the analog of $VR(\Lambda)$ for misfit.) Large values (blue) of VR represent better fit between observed and synthetic waveforms. Since M is required to have correct polarities, the plot of $VR(\Lambda)$ is only defined on the region $n(\Lambda) = 0$. The beachball plotted at each point Λ of this region is the moment tensor $M(\Lambda)$ that maximizes $VR(M)$ with Λ fixed. Of the beachballs $M(\Lambda)$, our desired solution M_0 (green box) is the one with largest VR. The gray arcs on the lune are the great circle arcs $\lambda_1 = 0$, $\lambda_2 = 0$, and $\lambda_3 = 0$ (white, green, and red in Figure 2.1). Selected eigenvalue triples (black dots) on the boundary of the lune are indicated, with the understanding that the triples need to be normalized. The positive isotropic source $(1, 1, 1)$ is at the top, the negative isotropic source $(-1, -1, -1)$ is at the bottom, and the double couple $(1, 0, -1)$, not shown, would be at the center of the lune. (d) The moment tensor M_0, the same as in (c) but plotted in a lower-hemisphere projection. For this event, all ray paths travel upward from the source to the stations, so the stations to the east, having upward (compressional) first motions, are plotted on the left of the beachball at the antipode of the ray path direction.

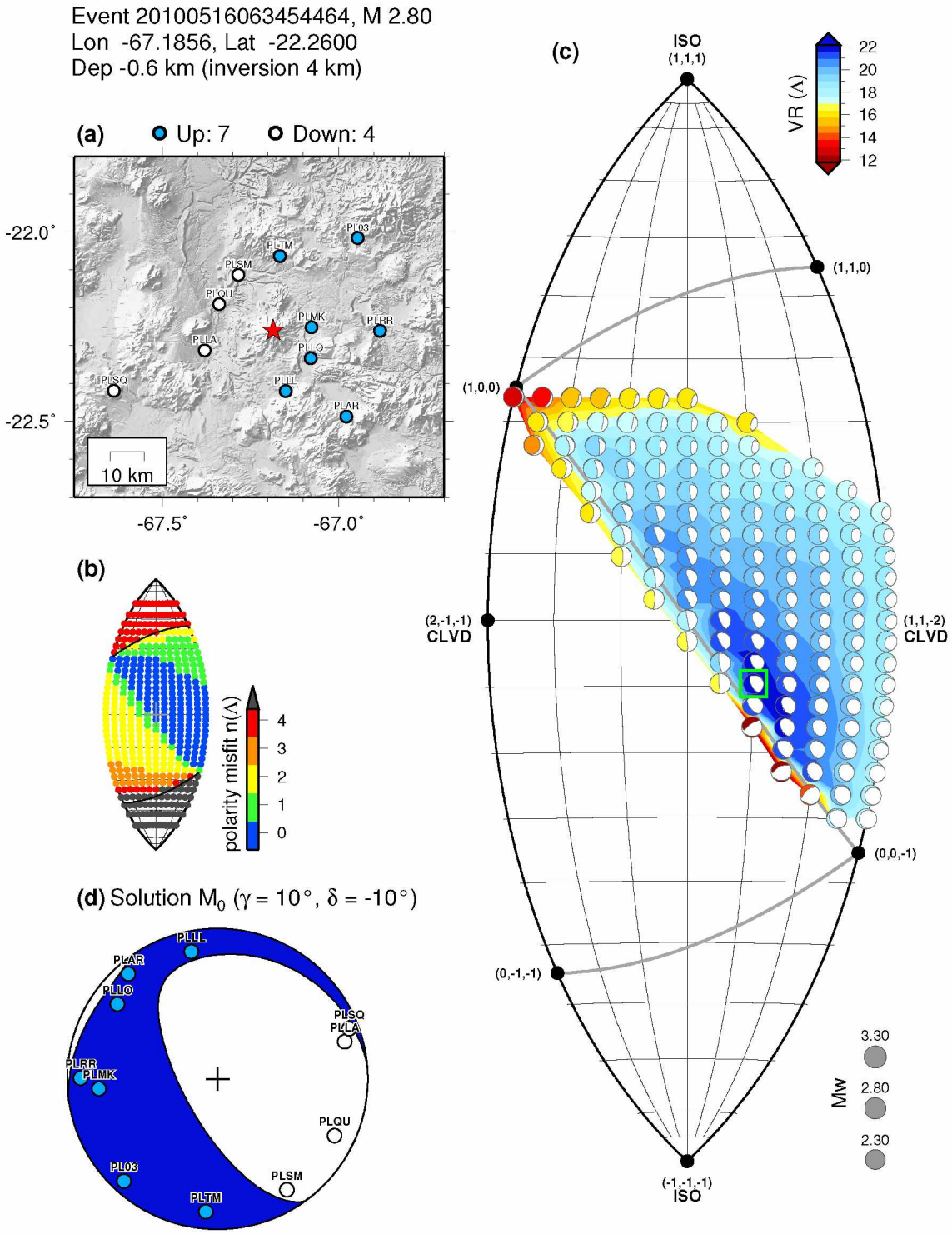
Event 20100516063454464, M 2.80
Lon -67.1856, Lat -22.2600
Dep -0.6 km (inversion 4 km)
(a)
Up: 7
Down: 4
-22.0˚
-22.5˚
-67.5˚
-67.0˚
10 km
PL03
PLTM
PLSM
PLQU
PLMK
PLRR
PLLA
PLLO
PLSQ
PLLL
PLAR
(b)
polarity misfit n(Λ)
4
3
2
1
0
(c)
ISO
(1,1,1)
VR (Λ)
22
20
18
16
14
12
(1,1,0)
(1,0,0)
(2,-1,-1)
CLVD
(1,1,-2)
CLVD
(0,0,-1)
(0,-1,-1)
(-1,-1,-1)
ISO
Mw
3.30
2.80
2.30
(d) Solution M0 (γ = 10°, δ = -10°)
PLLL
PLAR
PLLO
PLSQ
PLLA
PLRR
PLMK
PLQU
PL03
PLSM
PLTM

Figure 2.6

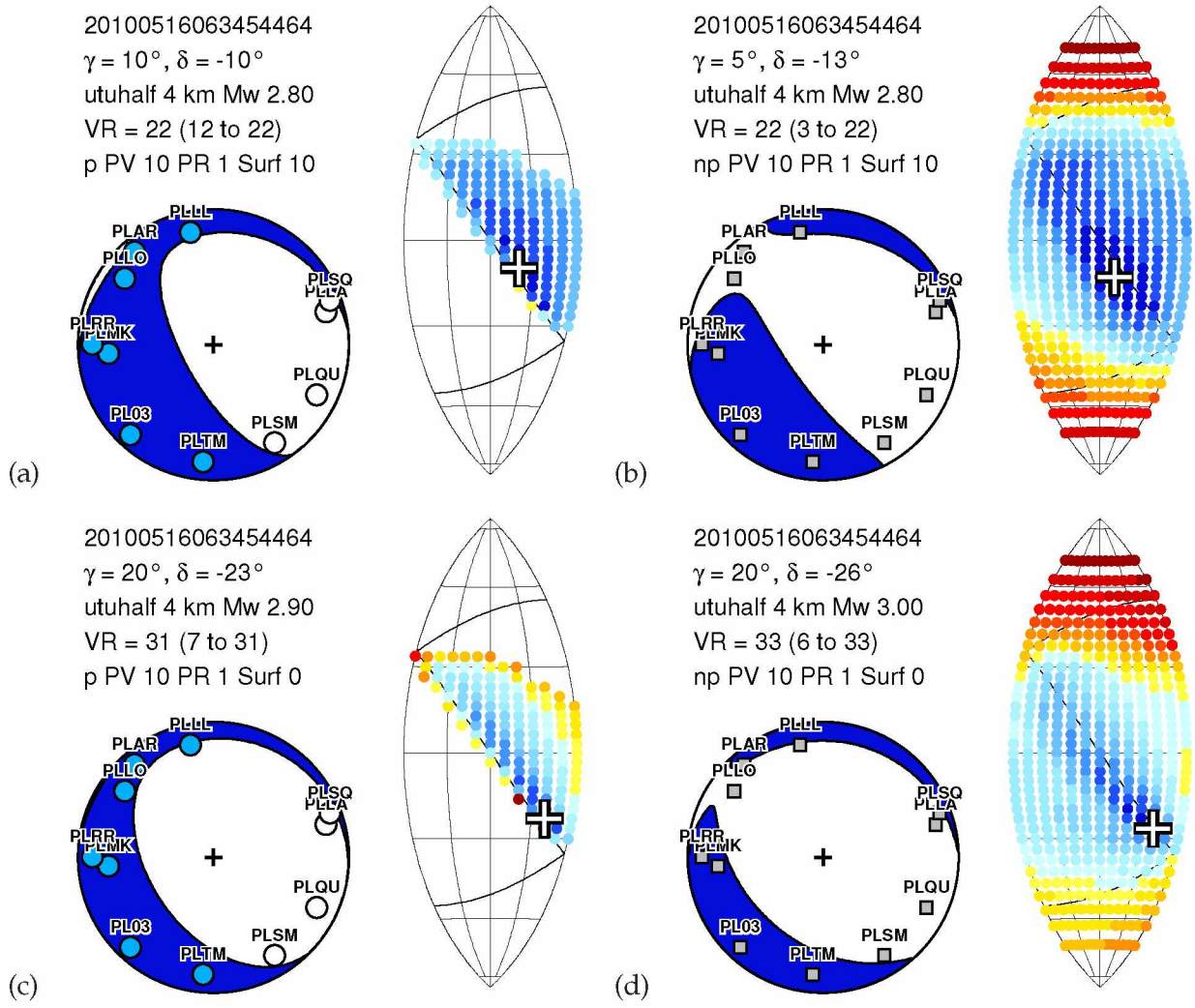

Figure 2.7: The influence of using first-motion polarities and surface waves on the full moment tensor solution, illustrated for the example event (Figures 2.4–2.6). Each two-part subplot is a distilled version of the full information represented in Figure 2.6. The beachball is the solution M_0 (Figure 2.6d); the lune plot shows $VR(\Lambda)$, with dark blue colors representing preferred solutions. The cross is plotted at $\Lambda(M_0)$, whose corresponding lune longitude γ and lune latitude δ are listed in the header. The value of $VR(M_0)$ is listed, along with the range of VR that are plotted. See Table 2.3 for a comparison of inversion results for the example event. (a) Inversion using polarities, P waves, and surface waves. The expanded version of this figure is Figure 2.6. (b) Inversion using P waves and surface waves. The difference between (a) and (b) are $\omega = 9°$, $\theta = 6°$, $\Delta VR = -0.3$. (c) Inversion using polarities and P waves. (d) Inversion using P waves only. The difference between (c) and (d) are $\omega = 13°$, $\theta = 4°$, $\Delta VR = -1.9$. For most of our events, we used polarities and P waves but not surface waves.

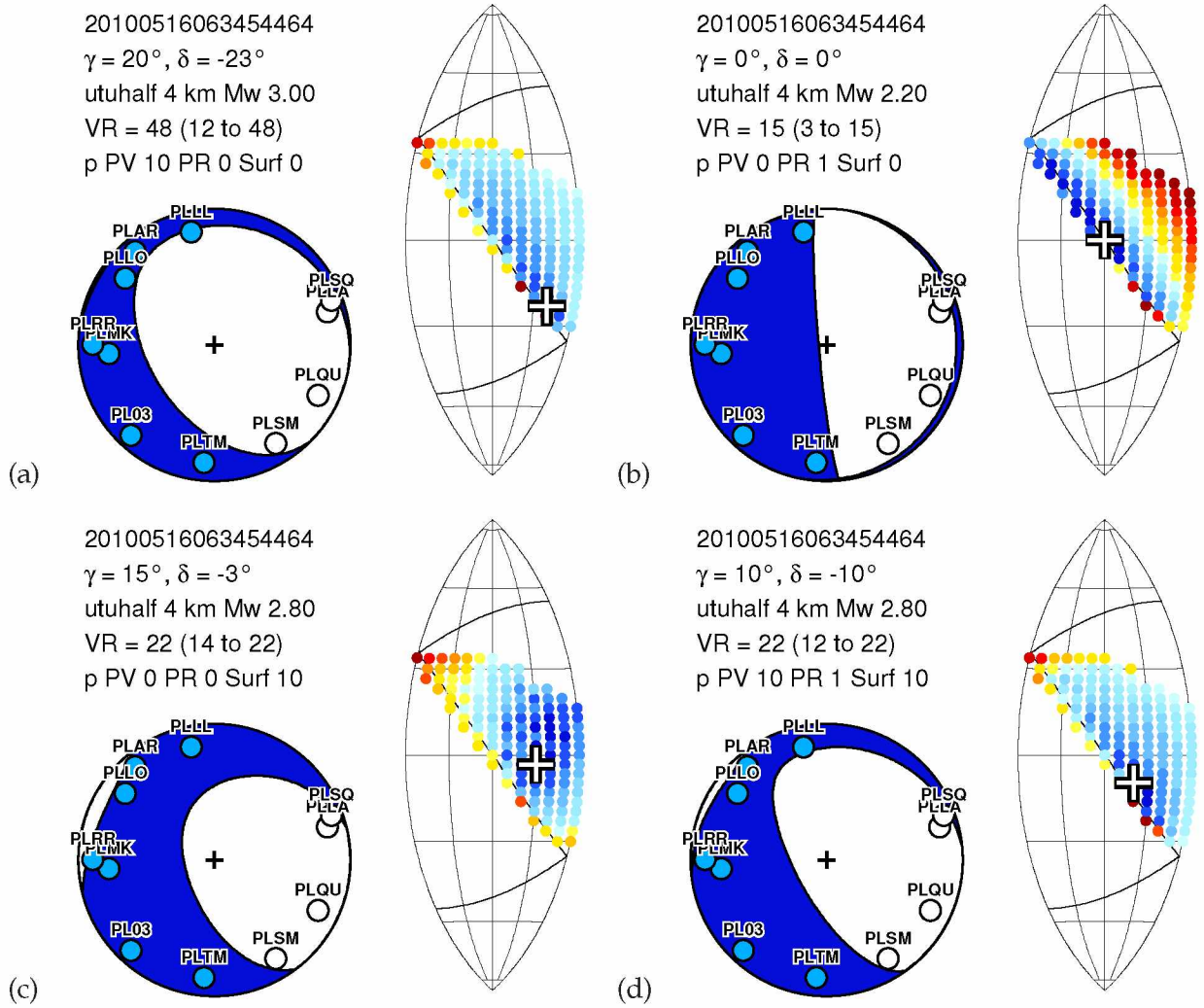

Figure 2.8: The influence of using different waveform components and different weights, illustrated for the example event. See Figure 2.7 caption for a description of the subplots. Here all inversions used first-motion polarities. See Table 2.3 for a comparison of inversion results for the example event. (a) Inversion using vertical component P waves only. (b) Inversion using radial component P waves only. (c) Inversion using surface waves only. (d) Inversion using P waves and surface waves.

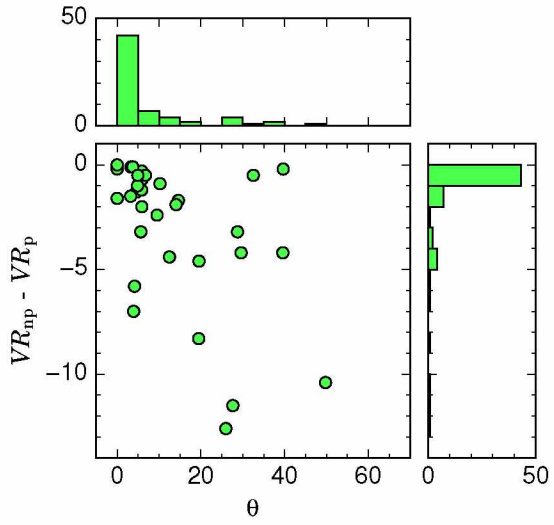

Figure 2.9: The influence of first-motion polarities on the moment tensor inversions for 63 events. Each of the 63 events is inverted twice, once with polarities (subscript 'p') and once without polarities (subscript 'np'). The two solutions are compared by (1) their moment tensors, quantified by the angle θ between source types Λ_{np} and Λ_p, and (2) their fits to waveforms, quantified by the difference in variance reduction $\Delta VR = VR_{np} - VR_p$. The figure shows that for the majority of the 63 events, inversions with or without first motions show differences in source types of $\theta \leq 5^\circ$ and differences in waveform fits of $\Delta VR \leq 1\%$.

Figure 2.10: [FOLLOWING PAGE] Four examples of moment tensor solutions showing the influence of using first-motion polarities identified in Figure 2.9. Each subplot contains a pair of beachball-and-lune plots. (a) (left) Moment tensor solution M_0 and lune plot $VR(\Lambda)$ using no first-motion polarities. (right) Same, but using first-motion polarities. The blue circles on the beachball are upward first motions (compressions), and the white circles are downward first motions (dilatations). The difference between the two moment tensors is represented by their angular distance in matrix space ($\omega = 0^\circ$), their angular distance on the lune ($\theta = 0^\circ$), and their difference in variance reduction ($\Delta VR = 0$). (b) Same as (a), but for a different event: $\omega = 10^\circ$, $\theta = 6^\circ$, $\Delta VR = -1.2$. (c) Same as (a), but for a different event: $\omega = 0^\circ$, $\theta = 0^\circ$, $\Delta VR = 0$. (d) Same as (a), but for a different event: $\omega = 65^\circ$, $\theta = 26^\circ$, $\Delta VR = -12.6$. The example in (d) was chosen to highlight an anomalous event with large values of θ and ΔVR; this is the bottom point plotted in Figure 2.9.

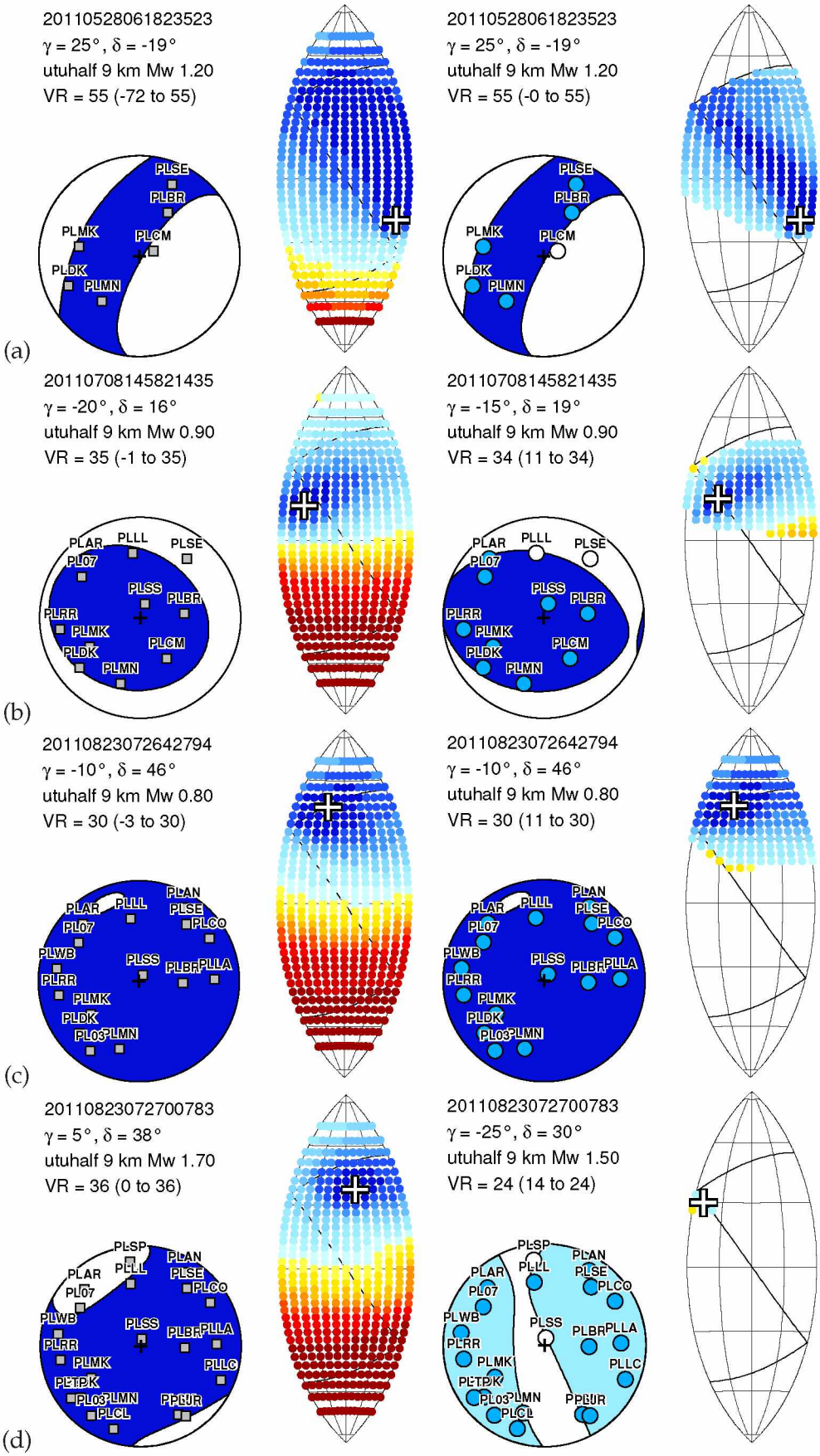
20110528061823523
γ = 25°, δ = -19°
utuhalf 9 km Mw 1.20
VR = 55 (-72 to 55)
PLSE
PLBR
PLMK
PLCM
PLDK
PLMN
20110528061823523
γ = 25°, δ = -19°
utuhalf 9 km Mw 1.20
VR = 55 (-0 to 55)
PLSE
PLBR
PLMK
PLCM
PLDK
PLMN
(a)
20110708145821435
γ = -20°, δ = 16°
utuhalf 9 km Mw 0.90
VR = 35 (-1 to 35)
PLAR
PLLL
PLSE
PL07
PLSS
PLBR
PLRR
PLMK
PLCM
PLDK
PLMN
20110708145821435
γ = -15°, δ = 19°
utuhalf 9 km Mw 0.90
VR = 34 (11 to 34)
PLAR
PLLL
PLSE
PL07
PLSS
PLBR
PLRR
PLMK
PLCM
PLDK
PLMN
(b)
20110823072642794
γ = -10°, δ = 46°
utuhalf 9 km Mw 0.80
VR = 30 (-3 to 30)
PLAN
PLAR
PLLL
PLSE
PLCO
PL07
PLWB
PLSS
PLBR
PLLA
PLRR
PLMK
PLDK
PL03
PLMN
20110823072642794
γ = -10°, δ = 46°
utuhalf 9 km Mw 0.80
VR = 30 (11 to 30)
PLAN
PLAR
PLLL
PLSE
PLCO
PL07
PLWB
PLSS
PLBR
PLLA
PLRR
PLMK
PLDK
PL03
PLMN
(c)
20110823072700783
γ = 5°, δ = 38°
utuhalf 9 km Mw 1.70
VR = 36 (0 to 36)
PLSP
PLAN
PLAR
PLLL
PLSE
PLCO
PL07
PLWB
PLSS
PLBR
PLLA
PLRR
PLMK
PLLC
PETPK
PL03
PLMN
PPLUR
PLCL
20110823072700783
γ = -25°, δ = 30°
utuhalf 9 km Mw 1.50
VR = 24 (14 to 24)
PLSP
PLAN
PLAR
PLLL
PLSE
PLCO
PL07
PLWB
PLSS
PLBR
PLLA
PLRR
PLMK
PLLC
PETPK
PL03
PLMN
PPLUR
PLCL
(d)

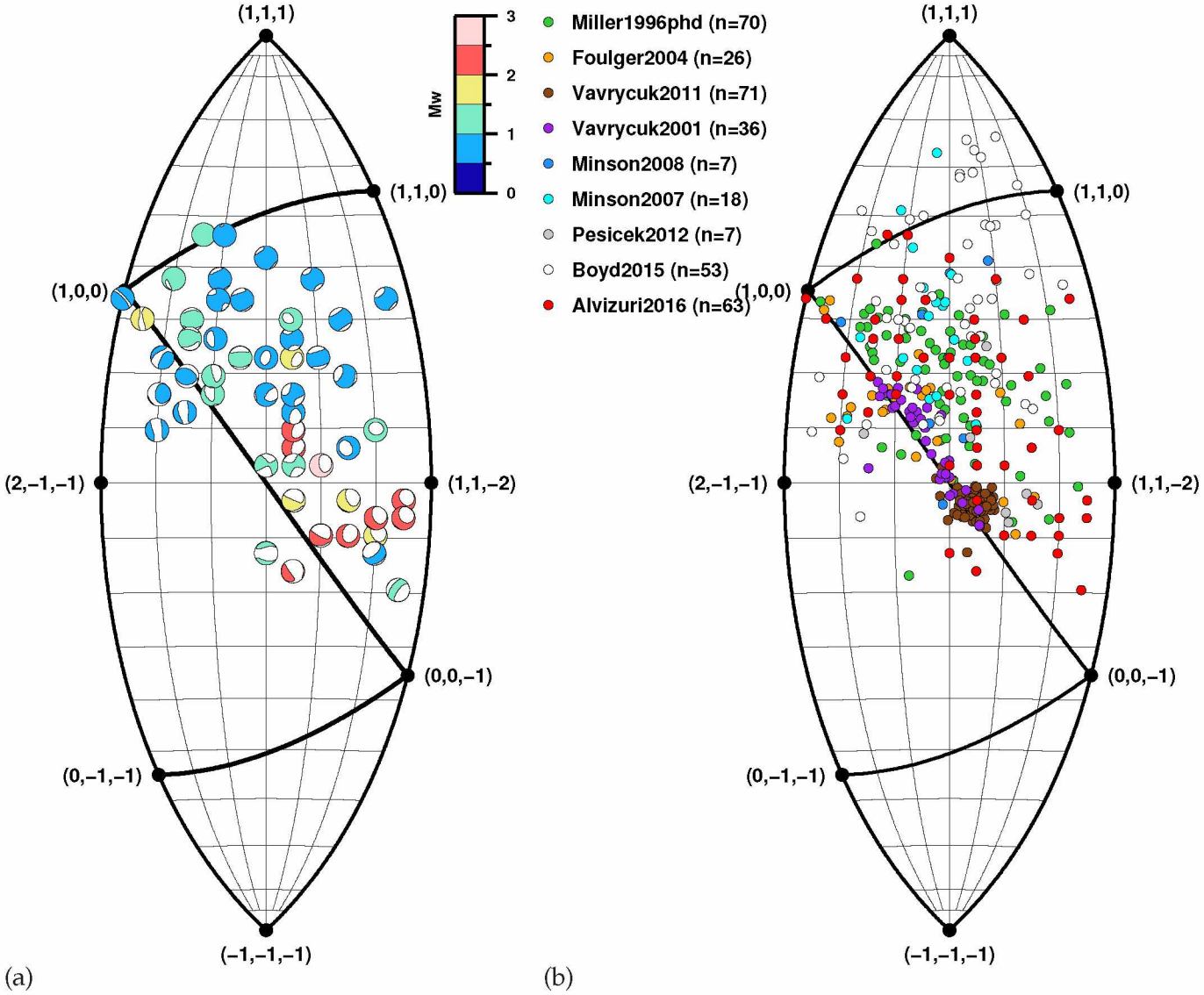

Figure 2.11: Our catalog of 63 moment tensor solutions, in comparison with previously published studies. (a) 63 moment tensor solutions from this study; beachballs are colored by estimated magnitude. Solutions are tabulated in Table 2.4. A key component of our analysis—the permissible lune regions on the basis of polarities—is not represented here but can be seen in other figures (e.g., Figure 2.6c and within Alvizuri (2015)). (b) Comparison between our solutions (red circles) and other published data sets for volcanic and geothermal regions (Table 2.1).

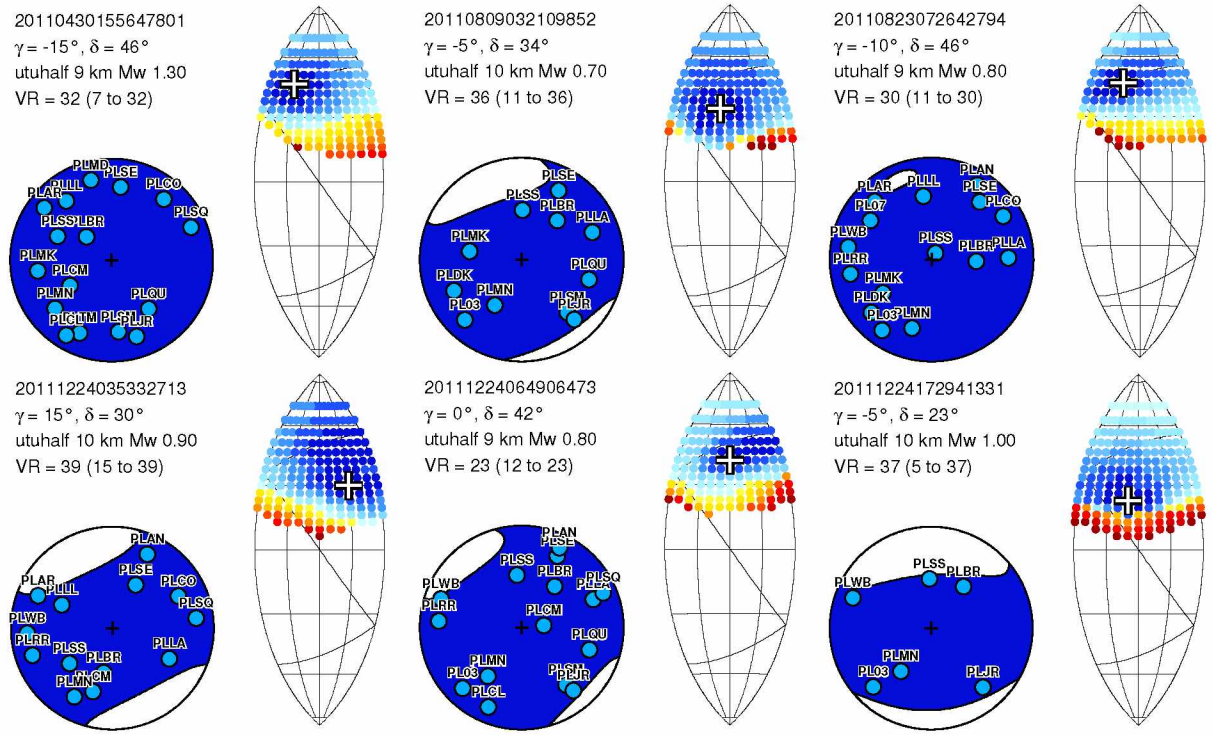

Figure 2.12: Solutions for isotropic events. We define an 'isotropic event' formally as having polarities (1) that are upward at all stations and (2) that exclude the possibility of a double couple moment tensor. The locations of these events are shown in Figure 2.15.

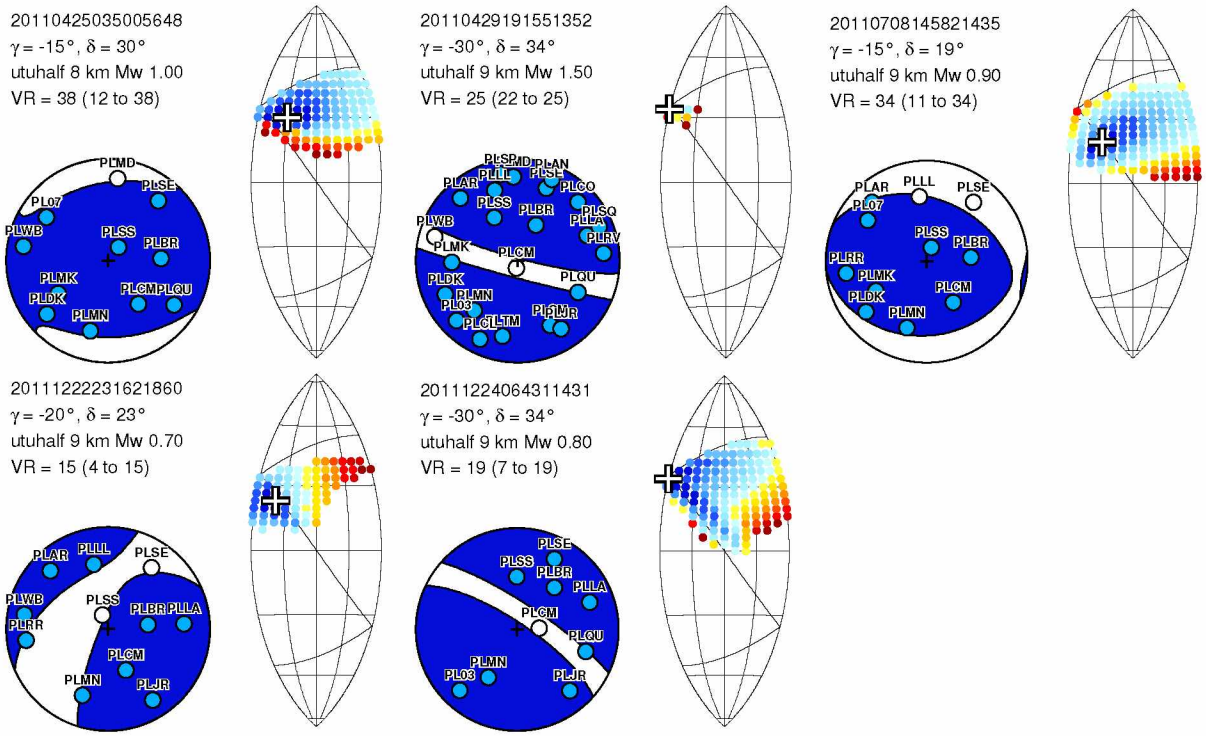

Figure 2.13: Solutions for tensional crack events. We define a 'tensional crack' event formally as having its best-fitting solution on the region of the lune with $\gamma \leq -15^\circ$ and as having polarities that exclude the possibility of a double couple moment tensor. The locations of these events are shown in Figure 2.15.

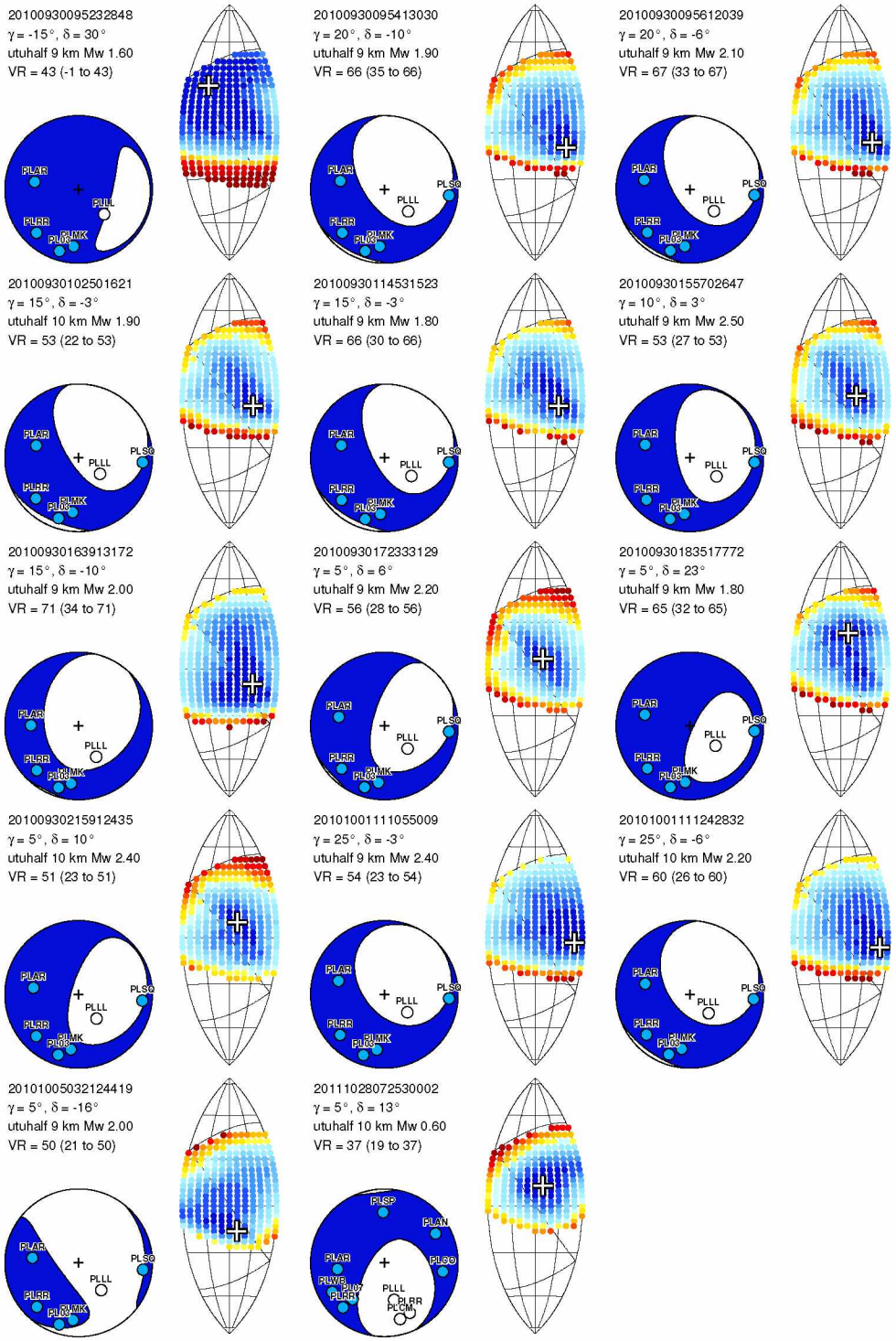

Figure 2.14: Subset of events that occur in a region southeast of the volcanic center, between longitudes $-67.15°$ and $-67.05°$ and between latitudes $-22.53°$ and $-22.43°$. The events are sorted by origin time, with the first 12 occurring within a time period of 25 hours. For most of the events, a double couple moment tensor provides a decent fit to the observed waveforms.; that is, the color at the double couple (center of lune) is dark blue. The locations of these events are shown in Figure 2.15.

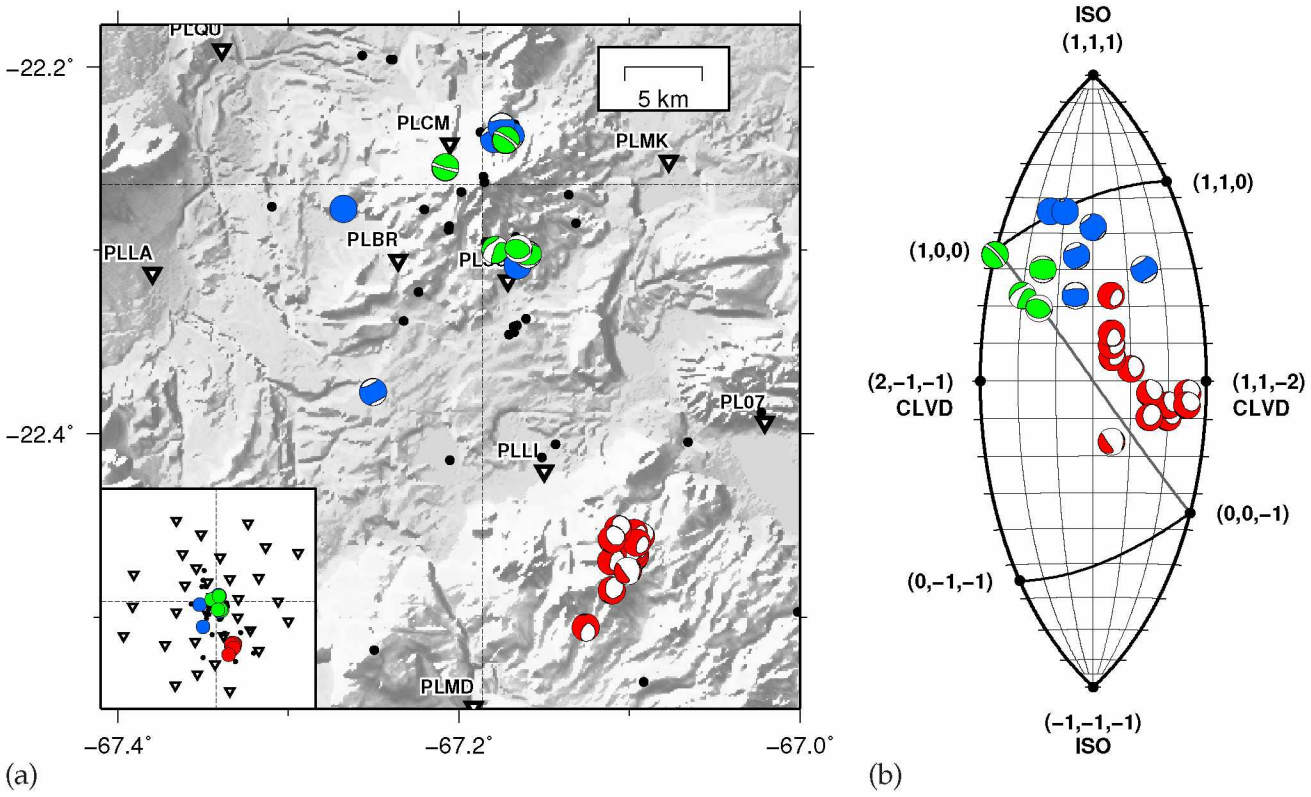

Figure 2.15: Summary of three subsets of events featured in Figures 2.12–2.14. The subsets are indicated by beachball color: isotropic (blue: 6 events), tensional crack (green: 5 events), and double couple (red: 14 events). (a) Map of the subset events. Uturuncu volcano is marked by the crossline at longitude $-67.19°$, latitude $-22.26°$. As shown in the inset map, all three subsets are inside the array of stations (Figure 2.2a). Most of the isotropic events and tensional crack events are distributed within 10 km of Uturuncu volcano. The cluster of double-couple events is about 25 km southeast of Uturuncu. (b) Lune plot of the subset events. Our selection criteria for the subsets are based on the source type; hence there is clustering on the lune.

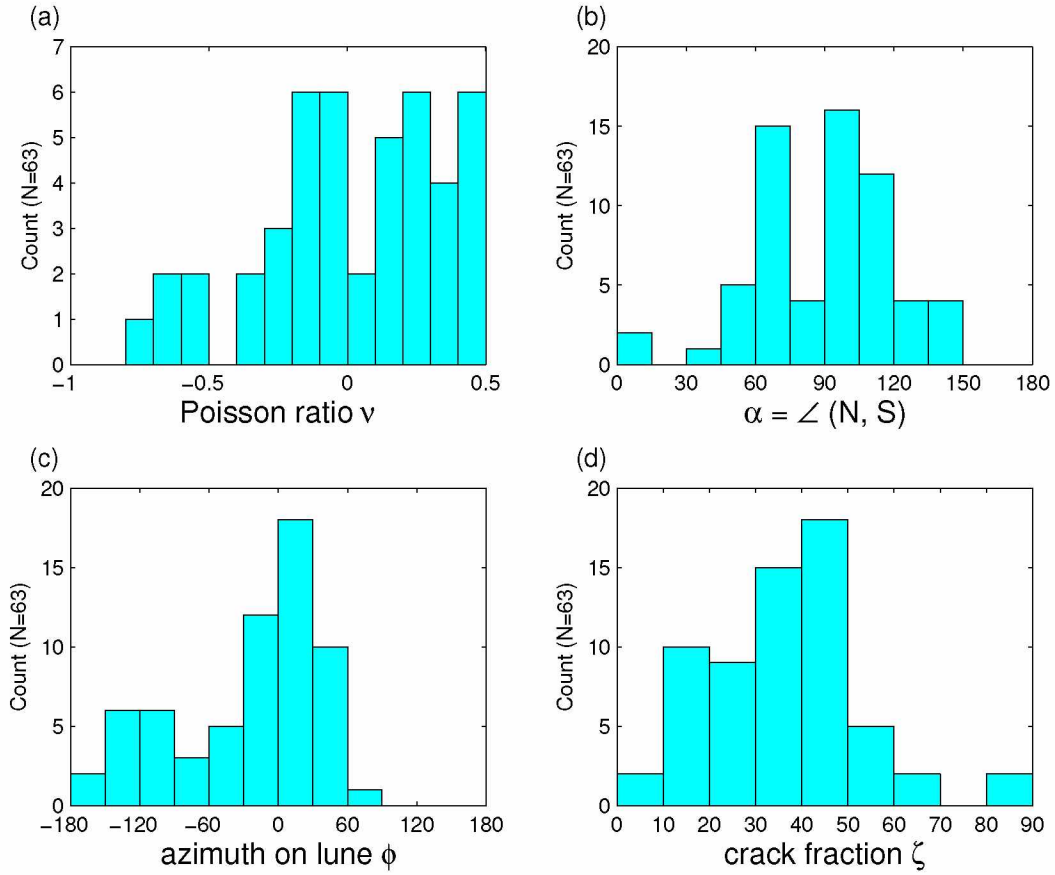

Figure 2.16: Source types of our 63 moment tensors represented by the classical model (a-b) and by the crack-plus-double-couple model (c-d). In the classical model each moment tensor source type is represented by a Poisson ratio ν and by the angle α between the fault normal and the slip direction. In the crack-plus-double-couple model each source type is represented by its azimuth ϕ on the lune and by the crack fraction ζ. These four quantities are calculated directly from the eigenvalues of the moment tensors. (a) Poisson values ν, plotted for the physically permissible range $-1 \leq \nu \leq 0.5$. 18 events fall outside the permissible range. (b) Angle between slip vector and normal vector: $\alpha = \angle(\mathbf{N}, \mathbf{S})$. For a tensional crack $\alpha = 0^\circ$, for a compressional crack $\alpha = 180^\circ$, and for a double couple $\alpha = 90^\circ$, where the slip vector is in the fault plane. (c) Azimuthal angle on the lune ϕ, measured from the double couple at ($\gamma = 0^\circ$, $\delta = 0^\circ$). Values increase in a counterclockwise sense from $\phi = 0^\circ$ at the isotropic point. (d) Crack fraction ζ. For a double couple moment tensor, $\zeta = 0^\circ$. For a tensional or compressional crack, $\zeta = 90^\circ$.

2.8 References

Aki, K. & Richards, P. G., 1980. *Quantitative Seismology, Theory and Methods*, W. H. Freeman, San Francisco, Calif., USA.

Alvizuri, C., 2015. Seismic moment tensor catalog for Uturuncu volcano, Bolivia, ScholarWorks@UA at http://hdl.handle.net/11122/6266 (last accessed 2016/01/22): descriptor file, text file of catalog, and composite figures of waveform fits and misfit analyses.

Alvizuri, C. & Tape, C., 2016. Full moment tensors for small events ($M_w < 3$) at Uturuncu volcano, Bolivia, *Geophys. J. Int.*, **206**, 1761–1783, doi:10.1093/gji/ggw247.

Aso, N. & Ide, S., 2014. Focal mechanisms of deep low-frequency earthquakes in Eastern Shimane in Western Japan, *J. Geophys. Res. Solid Earth*, **119**, 364–377, doi:10.1002/2013JB010681.

Baig, A. & Urbancic, T., 2010. Microseismic moment tensors: A path to understanding frac growth, *Leading Edge*, **29**, 320–324, doi:10.1190/1.3353729.

Boyd, O. S., Dreger, D. S., Lai, V. H., & Gritto, R., 2015. A systematic analysis of seismic moment tensor at The Geysers geothermal field, California, *Bull. Seis. Soc. Am.*, **105**(6), 2969–2986, doi:10.1785/0120140285.

Chen, P., Jordan, T. H., & Zhao, L., 2005. Finite-moment tensor of the 3 September 2002 Yorba Linda earthquake, *Bull. Seis. Soc. Am.*, **95**(3), 1170–1180, doi:10.1785/0120040094.

Chiang, A., Dreger, D. S., Ford, S. R., & Walter, W. R., 2014. Source characterization of underground explosions from combined regional moment tensor and first-motion analysis, *Bull. Seis. Soc. Am.*, **104**(4), 1587–1600, doi:10.1785/0120130228.

Chinn, D. S. & Isacks, B. L., 1983. Accurate source depths and focal mechanisms of shallow earthquakes in western South America and in the New Hebrides Island Arc, *Tectonics*, **2**(6), 529–563.

Chmielowski, J., Zandt, G., & Haberland, C., 1999. The central Andean Altiplano-Puna magma body, *Geophys. Res. Lett.*, **26**(6), 783–786, doi:10.1029/1999GL900078.

Chouet, B., Dawson, P., Ohminato, T., Martini, M., Saccorotti, G., Giudicepietro, F., De Luca, G., Milana, G., & Scarpa, R., 2003. Source mechanisms of explosions at Stromboli Volcano, Italy, determined from moment-tensor inversions of very-long-period data, *J. Geophys. Res.*, **108**(B1), 2019, doi:10.1029/2002JB001919.

Chouet, B. A. & Matoza, R. S., 2013. A multi-decadal view of seismic methods for detecting precursors of magma movement and eruption, *J. Volcan. Geothermal Res.*, **252**, 108–175, doi: 10.1016/j.jvolgeores.2012.11.013.

Comeau, M. J., Unsworth, M. J., Ticona, F., & Sunagua, M., 2015. Magnetotelluric images of magma distribution beneath Volcán Uturuncu, Bolivia: Implications for magma dynamics, *Geology*, **43**(3), 243–246, doi:10.1130/G36258.1.

Covellone, B. M. & Savage, B., 2012. A quantitative comparison between 1D and 3D source inversion methodologies: Application to the Middle East, *Bull. Seis. Soc. Am.*, **102**(5), 2189–2199, doi:10.1785/0120110278.

Dahm, T. & Brandsdóttir, B., 1997. Moment tensors of microearthquakes from the Eyjafjallajökull volcano in South Iceland, *Geophys. J. Int.*, **130**(1), 183–192.

Dammeier, F., Guilhem, A., Moore, J. R., Haslinger, F., & Loew, S., 2015. Moment tensor analysis of rockslide seismic signals, *Bull. Seis. Soc. Am.*, **105**(6), 3001–3014, doi:10.1785/0120150094.

de Silva, S. L., 1989. Altiplano-Puna volcanic complex of the central Andes, *Geology*, **17**, 1102–1106.

del Potro, R., Díez, M., Blundy, J., Camacho, A. G., & Gottsmann, J., 2013. Diapiric ascent of silicic magma beneath the Bolivian Altiplano, *Geophys. Res. Lett.*, **40**(10), 2044–2048, doi:10.1002/grl.50493.

Devlin, S., Isacks, B. L., Pritchard, M. E., Bamhart, W. D., & Lohman, R. B., 2012. Depths and focal mechanisms of crustal earthquakes in the central Andes determined from teleseismic waveform analysis and InSAR, *Tectonics*, **31**, TC2002, doi:10.1029/2011TC002914.

Dreger, D. S., Chiang, A., Ford, S. R., & Walter, W. R., 2012. Refinement of regional distance seismic moment tensor and uncertainty analysis for source-type identification, in *Proceedings of the 2012 Monitoring Research Review: Ground-Based Nuclear Explosion Monitoring Technologies*, pp. 377–386, National Nuclear Security Administration.

Dufumier, H. & Rivera, L., 1997. On the resolution of the isotropic component in moment tensor inversion, *Geophys. J. Int.*, **131**, 595–606.

Eisner, L., Williams-Stroud, S., Hill, A., Duncan, P., & Thornton, M., 2010. Beyond the dots in the box: Microseismicity-constrained fracture models for reservoir simulation, *Leading Edge*, **29**(3), 326–333, doi:10.1190/1.3353730.

Fialko, Y. & Pearse, J., 2012. Sombrero uplift above the Altiplano-Puna magma body: Evidence of a ballooning mid-crustal diapir, *Science*, **338**, 250–252, doi:10.1126/science.1226358.

Ford, S. R., Dreger, D. S., & Walter, W. R., 2009. Identifying isotropic events using a regional moment tensor inversion, *J. Geophys. Res.*, **114**, B01306, doi:10.1029/2008JB005743.

Ford, S. R., Dreger, D. S., & Walter, W. R., 2010. Network sensitivity solutions for regional moment-tensor inversions, *Bull. Seis. Soc. Am.*, **100**(5A), 1962–1970, doi:10.1785/0120090140.

Ford, S. R., Walter, W. R., & Dreger, D. S., 2012. Event discrimination using regional moment tensors with teleseismic-*P* constraints, *Bull. Seis. Soc. Am.*, **102**(2), 867–872, doi:10.1785/0120110227.

Foulger, G. R., Julian, B. R., Hill, D. P., Pitt, A. M., Malin, P. E., & Shalev, E., 2004. Non-double-couple microearthquakes at Long Valley caldera, California, provide evidence for hydraulic fracturing, *J. Volcan. Geothermal Res.*, **132**, 45–71, doi:10.1016/S0377-0273(03)00420-7.

Guilhem, A., Hutchings, L., Dreger, D. S., & Johnson, L. R., 2014. Moment tensor inversions of $M \sim 3$ earthquakes in the Geysers geothermal fields, California, *J. Geophys. Res. Solid Earth*, **119**(3), 2121–2137, doi:10.1002/2013JB010271.

Haberland, C., Rietbrock, A., Schurr, B., & Brasse, H., 2003. Coincident anomalies of seismic attenuation and electrical resistivity beneath the southern Bolivian Altiplano plateau, *Geophys. Res. Lett.*, **30**(18), 1923, doi:10.1029/2003GL017492.

Horálek, J., Šíený, J., & Fischer, T., 2002. Moment tensors of the January 1997 earthquake swarm in NW Bohemia (Czech Republic): double-couple vs. non-double-couple events, *Tectonophysics*, **356**, 65–85, doi:10.1016/S0040-1951(02)00377-3.

Isacks, B. L., 1988. Uplift of the central Andean plateau and bending of the Bolivian orocline, *J. Geophys. Res.*, **93**(B4), 3211–3231.

Jay, J. A., Pritchard, M. E., West, M. E., Christensen, D., Haney, M., Minaya, E., Sunagua, M., McNutt, S. R., & Zabala, M., 2011. Shallow seismicity, triggered seismicity, and ambient noise tomography at the long-dormant Uturuncu Volcano, Bolivia, *Bull. Volcanology*, **74**, 817–837, doi:10.1007/s00445-011-0568-7.

Julian, B. R., Miller, A. D., & Foulger, G. R., 1998. Non-double-couple earthquakes: 1. Theory, *Rev. Geophys.*, **36**(4), 525–549, doi:10.1029/98RG00716.

Julian, B. R., Foulger, G. R., Monastero, F. C., & Bjornstad, S., 2010. Imaging hydraulic fractures in a geothermal reservoir, *Geophys. Res. Lett.*, **37**, L07305, doi:10.1029/2009GL040933.

Keyson, L. & West, M. E., 2013. Earthquake sources near Uturuncu Volcano, Abstract V13B-2603 presented at 2013 Fall Meeting, AGU, San Francisco, Calif., 9-13 Dec.

Liu, Q., Polet, J., Komatitsch, D., & Tromp, J., 2004. Spectral-element moment tensor inversions for earthquakes in southern California, *Bull. Seis. Soc. Am.*, **94**(5), 1748–1761, doi:10.1785/012004038.

Miller, A. D., 1996. *Seismic Structure and Earthquake Focal Mechanisms of the Hengill Volcanic Complex, SW Iceland*, Ph.D. thesis, U. of Durham, Durham, UK.

Miller, A. D., Foulger, G. R., & Julian, B. R., 1998a. Non-double-couple earthquakes: 2. Observations, *Rev. Geophys.*, **36**(4), 551–568.

Miller, A. D., Julian, B. R., & Foulger, G. R., 1998b. Three-dimensional seismic structure and moment tensors of non-double-couple earthquakes at the Hengill–Grensdalur volcanic complex, Iceland, *Geophys. J. Int.*, **133**, 309–325.

Minson, S. E. & Dreger, D. S., 2008. Stable inversions for complete moment tensors, *Geophys. J. Int.*, **174**, 585–592, doi:10.1111/j.1365-246X.2008.03797.x.

Minson, S. E., Dreger, D. S., Bürgmann, R., Kanamori, H., & Larson, K. M., 2007. Seismically and geodetically determined nondouble-couple source mechanisms from the 2000 Miyakejima volcanic earthquake swarm, *J. Geophys. Res.*, **112**, B10308, doi:10.1029/2006JB004847.

Nayak, A. & Dreger, D. S., 2014. Moment tensor inversion of seismic events associated with the sinkhole at Napoleonville salt dome, Louisiana, *Bull. Seis. Soc. Am.*, **104**(4), 1763–1776, doi:10.1785/0120130260.

Pesicek, J. D., Sileny, J., Prejean, S. G., & Thurber, C. H., 2012. Determination and uncertainty of moment tensors for microearthquakes at Okmok Volcano, Alaska, *Geophys. J. Int.*, **190**, 1689–1709, doi:10.1111/j.1365-246X.2012.05574.x.

Pesicek, J. D., Cieślik, K., Lambert, M.-A., Carrillo, P., & Birkelo, B., 2016. Dense surface seismic data confirm non-double-couple source mechanisms induced by hydraulic fracturing, *Geophysics*, **81**(6), KS207–KS217, doi:10.1190/GEO2016-0192.1.

Pritchard, M. E. & Simons, M., 2002. A satellite geodetic survey of large-scale deformation of volcanic centres in the central Andes, *Nature*, **418**, 167–171, doi:10.1038/nature00872.

Riedesel, M. A. & Jordan, T. H., 1989. Display and assessment of seismic moment tensors, *Bull. Seis. Soc. Am.*, **79**(1), 85–100.

Ross, Z. E., Ben-Zion, Y., & Zhu, L., 2015. Isotropic source terms of San Jacinto fault zone earthquakes based on waveform inversions with a generalized CAP method, *Geophys. J. Int.*, **200**, 1267–1278, doi:10.1093/gji/ggu460.

Salisbury, M. J., Jicha, B. R., de Silva, S. L., Singer, B. S., Jiménez, N. C., & Ort, M. H., 2011. $^{40}Ar/^{39}Ar$ chronostratigraphy of Altiplano-Puna volcanic complex ignimbrites reveals the development of a major magmatic province, *Geol. Soc. Am. Bull.*, **123**(5-6), 821–840, doi:10.1130/B30280.1.

Shen, W., Alvizuri, C., Lin, F.-C., & Tape, C., 2016. A one-dimensional velocity model for Uturuncu volcano, Bolivia, and its impact on full moment tensor inversions, *Geosphere* (in press), doi:10.1130/GES01353.1.

Šilený, J. & Milev, A., 2006. Seismic moment tensor resolution on a local scale: simulated rockburst and mine-induced seismic events in the Kopanang gold mine, South Africa, *Pure App. Geophys.*, **163**, 1495–1513, doi:10.1007/s00024-006-0089-z.

Šilený, J. & Milev, A., 2008. Source mechanism of mining induced seismic events — Resolution of double couple and non double couple models, *Tectonophysics*, **456**, 3–15, doi:10.1016/j.tecto.2006.09.021.

Šilený, J., Hill, D. P., Eisner, L., & Cornet, F. H., 2009. Non-double-couple mechanisms of microearthquakes induced by hydraulic fracturing, *J. Geophys. Res.*, **114**, B08307, doi:10.1029/2008JB005987.

Silwal, V. & Tape, C., 2016. Seismic moment tensors and estimated uncertainties in southern Alaska, *J. Geophys. Res. Solid Earth*, **121**, 2772–2797, doi:10.1002/2015JB012588.

Sparks, R. S. J., Folkes, C. B., Humphreys, M. C. S., Barfod, D. N., Clavero, J., Sunagua, M. C., McNutt, S. R., & Pritchard, M. E., 2008. Uturuncu volcano, Bolivia: Volcanic unrest due to mid-crustal magma intrusion, *Am. J. Sci.*, **308**, 727–769, doi:10.2475/06.2008.01.

Stähler, S. C. & Sigloch, K., 2014. Fully probabilistic seismic source inversion – Part 1: Efficient parameterisation, *Solid Earth*, **5**, 1055–1069, doi:10.5194/se-5-1055-2014.

Stierle, E., Vavryčuk, V., & Bohnhoff, M., 2014. Resolution of non-double-couple components in the seismic moment tensor using regional networks—II: application to aftershocks of the 1999 M_w 7.4 Izmit earthquake, *Geophys. J. Int.*, **196**, 1878–1888, doi:10.1093/gji/ggt503.

Tan, Y., Song, A., Wei, S., & Helmberger, D., 2010. Surface wave path corrections and source inversions in southern California, *Bull. Seis. Soc. Am.*, **100**(6), 2891–2904, doi:10.1785/0120090063.

Tape, W. & Tape, C., 2012. A geometric setting for moment tensors, *Geophys. J. Int.*, **190**, 476–498, doi:10.1111/j.1365-246X.2012.05491.x.

Tape, W. & Tape, C., 2013. The classical model for moment tensors, *Geophys. J. Int.*, **195**, 1701–1720, doi:10.1093/gji/ggt302.

Tape, W. & Tape, C., 2016. A confidence parameter for seismic moment tensors, *Geophys. J. Int.*, **205**, 938–953, doi:10.1093/gji/ggw057.

Vavryčuk, V., 2001. Inversion for parameters of tensile earthquakes, *J. Geophys. Res.*, **106**(B8), 16,339–16,355, doi:10.1029/2001JB000372.

Vavryčuk, V., 2011. Tensile earthquakes: Theory, modeling, and inversion, *J. Geophys. Res.*, **116**, B12320, doi:10.1029/2011JB008770.

Walter, F., Clinton, J. F., Deichmann, N., Dreger, D. S., Minson, S. E., & Funk, M., 2009. Moment tensor inversions of icequakes on Gornergletscher, Switzerland, *Bull. Seis. Soc. Am.*, **99**(2A), 852–870, doi:10.1785/0120080110.

Walter, F., Dreger, D. S., Clinton, J. F., Deichmann, N., & Funk, M., 2010. Evidence for near-horizontal tensile faulting at the base of Gornergletscher, a Swiss Alpine Glacier, *Bull. Seis. Soc. Am.*, **100**(2), 458–472, doi:10.1785/0120090083.

Ward, K. M., Zandt, G., Beck, S. L., Christensen, D. H., & McFarlin, H., 2014. Seismic imaging of the magmatic underpinnings beneath the Altiplano-Puna volcanic complex from the joint inversion of surface wave dispersion and receiver functions, *Earth Planet. Sci. Lett.*, **404**, 43–53, doi:10.1016/j.epsl.2014.07.022.

West, M. & Christensen, D., 2010. Investigating the relationship between pluton growth and volcanism at two active intrusions in the central Andes, International Federation of Digital Seismograph Networks. Other/Seismic Network. doi:10.7914/SN/XP_2010.

West, M. E., Kukarina, E., & Koulakov, I., 2013. Structure of Uturuncu volcano from seismic tomography, Abstract V13B-2600 presented at 2013 Fall Meeting, AGU, San Francisco, Calif., 9-13 Dec.

Zandt, G. & Ammon, C. J., 1995. Continental crust composition constrained by measurements of crustal Poisson's ratio, *Nature*, **374**, 152–154.

Zandt, G., Beck, S. L., Ruppert, S. R., Ammon, C. J., Rock, D., Minaya, E., Wallace, T. C., & Silver, P. G., 1996. Anomalous crust of the Bolivian Altiplano, central Andes: Constraints from broadband regional seismic waveforms, *Geophys. Res. Lett.*, **23**(10), 1159–1162.

Zandt, G., Leidig, M., Chmielowski, J., Baumont, D., & Yuan, X., 2003. Seismic detection and characterization of the Altiplano-Puna magma body, central Andes, *Pure App. Geophys.*, **160**, 789–807, doi:10.1007/PL00012557.

Zhao, L.-S. & Helmberger, D. V., 1994. Source estimation from broadband regional seismograms, *Bull. Seis. Soc. Am.*, **84**(1), 91–104.

Zhu, L. & Ben-Zion, Y., 2013. Parameterization of general seismic potency and moment tensors for source inversion of seismic waveform data, *Geophys. J. Int.*, **194**, 839–843, doi:10.1093/gji/ggt137.

Zhu, L. & Helmberger, D., 1996. Advancement in source estimation techniques using broadband regional seismograms, *Bull. Seis. Soc. Am.*, **86**(5), 1634–1641.

Zhu, L. & Rivera, L. A., 2002. A note on the dynamic and static displacements from a point source in multilayered media, *Geophys. J. Int.*, **148**, 619–627, doi:10.1046/j.1365-246X.2002.01610.x.

Zhu, L. & Zhou, X., 2016. Seismic moment tensor inversion using 3D velocity model and its application to the 2013 Lushan earthquake sequence, *Physics and Chemistry of the Earth* (in press), doi:10.1016/j.pce.2016.01.002.

Chapter 3

Estimation of full moment tensors, including uncertainties, for earthquakes, volcanic events, and nuclear explosions[1]

3.1 Abstract

A seismic moment tensor is a 3×3 symmetric matrix that provides a compact representation of a seismic source. We develop an algorithm to estimate moment tensors and their uncertainties from observed seismic data. For a given event, the algorithm performs a grid search over the six-dimensional space of moment tensors by generating synthetic waveforms for each moment tensor and then evaluating a misfit function between the observed and synthetic waveforms. 'The' moment tensor M_0 for the event is then the moment tensor with minimum misfit. To describe the uncertainty associated with M_0, we first convert the misfit function to a probability function. The uncertainty, or rather the confidence, is then given by the 'confidence curve' $\mathscr{P}(V)$, where $\mathscr{P}(V)$ is the probability that the true moment tensor for the event lies within the neighborhood of M that has fractional volume V. The area under the confidence curve provides a single, abbreviated 'confidence parameter' for M_0. We apply the method to data from events in different regions and tectonic settings: 63 small ($M_w < 2.5$) events at Uturuncu volcano in Bolivia, 21 moderate ($M_w > 4$) earthquakes in the southern Alaska subduction zone, and 12 earthquakes and 17 nuclear explosions at the Nevada Test Site. Characterization of moment tensor uncertainties puts us in better position to discriminate among moment tensor source types and to assign physical processes to the events.

3.2 Introduction

The seismic moment tensor is a 3×3 symmetric matrix that characterizes a seismic source within Earth's crust. Its six parameters can be separated into three eigenvalues that characterize the magnitude and moment tensor 'source type,' and three angles (e.g., strike, dip, and rake) that provide the moment tensor orientation. For most earthquakes, the source type is a four-parameter double couple moment tensor, representing shear faulting. For exotic events, the source type is characterized by a six-parameter 'full' moment tensor, whose eigenvalues may represent, for example, an explosion, an implosion, or an oblique opening (or closing) crack (Aki & Richards, 2002).

Full moment tensors have been used to characterize events in a range of settings, including earthquakes, volcanoes, glaciers, landslides, hydraulic fracturing, mine collapses, and nuclear explosions (Alvizuri & Tape, 2016, tab. 1). In most studies, the goal has been to estimate the moment

[1]To be published as C. Alvizuri, V. Silwal, L. Krischer, and C. Tape. Estimation of full moment tensors with uncertainties, for earthquakes, volcanic events, and nuclear tests. *Geophysics* (in prep.).

tensor M_0 that provides synthetic seismograms that best-fit a set of observed seismograms. M_0 provides the minimum of a misfit function defined over the space of moment tensors.

In the past decade, efforts have been made to characterize uncertainties of moment tensors. Some studies have estimated the uncertainties by repeatedly solving for M_0 using different subsets of data (boot-strapping or related Monte Carlo approaches) (Šilený & Milev, 2006; Ford et al., 2009; Vavryčuk, 2011; Ross et al., 2015; Pesicek et al., 2012, 2016). Other studies have provided a view of how the misfit function varied over the full space of moment tensor source types (Ford et al., 2010; Nayak & Dreger, 2014; Boyd et al., 2015; Alvizuri & Tape, 2016). To our knowledge, Stähler & Sigloch (2014) is the only study to have formally accounted for uncertainties, by generating moment tensor samples of a posterior probability density. This was made possible by using a uniform distribution of moment tensors; we use an alternative uniform distribution in our study (Tape & Tape, 2015).

The goal of this study is to estimate moment tensor uncertainties for three sets of previously studied events: 21 Alaska earthquakes, 63 volcanic events, and 29 events from the Nevada Test Site. Following Tape & Tape (2016), we represent moment tensor uncertainties in the form of a confidence curve that expresses the concentration of probability in moment tensor space near M_0. We build upon three recent studies: Tape & Tape (2016), which established the theory for confidence curves; Silwal & Tape (2016), which estimated confidence curves for double couple moment tensors; and Alvizuri & Tape (2016), which estimated a catalog of full moment tensors for volcanic events. In our examination of earthquakes and nuclear explosions from the Nevada Test Site, we use the exact same events as in Ford et al. (2009). In comparison with the approach of Ford et al. (2009), we use more stations, body waves (in addition to surface waves), a broader bandpass for surface waves (10–50 s), and an alternative characterization of moment tensor uncertainties.

3.3 Data

We examine events from three previous studies: 21 earthquakes in southern Alaska (Silwal & Tape, 2016, tab. 4), 63 events at Uturuncu volcano in Bolivia (Alvizuri & Tape, 2016, tab. 4), and 29 earthquakes and nuclear tests at the Nevada Test Site (Ford et al., 2009, tab. 1). Figure 3.1 shows the three regions and the stations used within the moment tensor inversions.

For the Alaska and Uturuncu data sets, all waveforms are openly available from the IRIS Data Management Center. For the Nevada Test Site events, the waveforms are openly available from IRIS and the Northern California Data Center, while other waveforms are from Walter et al. (2006). A summary of available waveforms for the NTS events is provided in Table 3.1, where we see the expected trend of increasing data availability with time, as broadband seismic stations became more prevalent in the 1990s.

All waveforms were downloaded and processed using ObsPy, a python-based package for seismology (Beyreuther et al., 2010; Krischer et al., 2015). The processing steps for each event were: (1) obtain three-component waveforms and metadata from the IRIS (Incorporated Research Institutions for Seismology) Data Management Center, the Northern California Earthquake Data Center (NCEDC), or Walter et al. (2006); the time interval is 100 s before the origin time to 600 s after the origin time, (2) remove instrument response using an acausal Butterworth filter with frequencies 0.005, 0.006, 10.0, and 15.0 Hz (flat bandpass 0.006–10.0 Hz), (3) using the source-station azimuth and the sensor orientation angle, rotate horizontal components to radial and transverse directions. Additional processing steps, such as cutting time windows and additional bandpass filtering, were applied during the moment tensor inversions.

We use high-frequency P waves for the Uturuncu and NTS events. Within the misfit function, described next, we make waveform measurements between observed and synthetic P waves. These measurements are more reliable when we align the P waves on the observed P arrival time. For the Uturuncu events we use arrival times from Keyson & West (2013); for the NTS events we pick arrival times for the IRIS stations and use the arrival times in Walter et al. (2006) for the Lawrence Livermore National Laboratory (LLNL) stations. For the Uturuncu events we use first-motion polarity measurements from Alvizuri & Tape (2016).

3.4 Methods

Seismic moment tensor inversion requires specifying a misfit function between observed seismograms and synthetic (or 'modeled') seismograms. Synthetic seismograms are calculated using a model of the source—in our case, a moment tensor—and a model of Earth's structure—in our case, a layered model. We calculate synthetic seismograms for a range of source depths and source-station distances using the frequency-wavenumber method of Haskell (1964) amd Zhu & Rivera (2002). The source origin times and hypocenters are assumed to be fixed.

The misfit function we use, from Zhu & Helmberger (1996), measures integrated differences between observed and synthetic velocity seismograms within five time windows: P wave on vertical and radial components, Rayleigh wave on vertical and radial components, and Love wave on transverse component. Prior to calculating the waveform difference, we allow the synthetic seismograms to be shifted in time to maximize the cross-correlation with observed seismograms. For each station, three time shifts are allowed, for the P, Rayleigh, and Love waves. These different time shifts are allowed because these waves are sensitive to different parts of Earth structure. By allowing for different time shifts, we are recognizing that our layered Earth structural models cannot adequately predict the traveltimes for seismic waves. Additional discussion of time shifts can be found in Silwal & Tape (2016).

For our moment tensor inversions, we use the 'cut-and-paste' (CAP) code of Zhu & Helmberger (1996); Zhu & Ben-Zion (2013), with some modifications. For the misfit function we use an L1 norm (Silwal & Tape, 2016), and we incorporate the number of misfitting polarities into the waveform-based misfit function. We also use an efficient grid search over moment tensor space, described below.

3.4.1 Parameterization of moment tensors

A moment tensor is a 3×3 symmetric matrix that can be expressed as $M = [\Lambda]_U = U[\Lambda]U^{-1}$, where $[\Lambda]$ is a diagonal matrix of eigenvalues, with $\Lambda = (\lambda_1, \lambda_2, \lambda_3)$ and $\lambda_1 \geq \lambda_2 \geq \lambda_3$. The parameterization of moment tensors is useful for visualizing moment tensor space, and it is critical for estimating uncertainties. For visualizing the space of moment tensor source types, we use the eigenvalue space of moment tensors—represented by a lune. The lune is the set of normalized eigenvalues $\hat{\Lambda}/\|\Lambda\|$. The lune has the +isotropic moment tensor $(1,1,1)/\sqrt{3}$ at its north pole, the -isotropic moment tensor $(-1,-1,-1)/\sqrt{3}$ at its south pole, and the double couple moment tensor $(1,0,-1)/\sqrt{2}$ at its center. A picture is more effective: see Tape & Tape (2013, fig. 1) or Alvizuri & Tape (2016, fig. 1). The lune divides the source types—or beachball patterns—into four regions: (1) all-solid beachballs ($\lambda_3 > 0$), (2) solid beachballs with white caps ($\lambda_2 > 0 > \lambda_3$), (3) white beachballs with red caps ($\lambda_1 > 0 > \lambda_2$), (4) all-white beachballs ($\lambda_1 < 0$). (We note that the two-color beachballs do not represent the variations in amplitude of the source radiation pattern.)

The lune addresses two parameters of a seismic moment tensor. Earthquake magnitude, proportional to $\|\Lambda\|$, is the third parameter related to the eigenvalues. The remaining three parameters—strike angle, dip angle, and slip angle—describe the orientation U of the moment tensor.

To search moment tensor space, we separate magnitude from the five other parameters. Although the lune is effective for visualizing moment tensor space, it does not offer the most efficient parameters for a moment tensors grid search (Tape & Tape, 2015). Following Tape & Tape (2015), we parameterize moment tensors as follows:

- v, analogous to lune longitude, $-1/3 \leq v \leq 1/3$
- w, analogous to lune latitude, $-3\pi/8 \leq w \leq 3\pi/8$
- strike angle κ, $0^\circ \leq \kappa < 360^\circ$
- rake (or slip) angle σ, $-90^\circ \leq \sigma \leq 90^\circ$
- $h = \cos\theta$, $0 < h \leq 1$, corresponding to dip θ ranging from 0° to 90°

The lune latitude δ is related to lune colatitude β of Tape & Tape (2012) as $\delta = \pi/2 - \beta$. Similarly, the parameter w is related to u of Tape & Tape (2015) as $w = 3\pi/4 - u$. The five parameters $(v, w, \kappa, \sigma, h)$ provide uniformly distributed moment tensors, in that equal volumes in the 5D space will have equal numbers of moment tensors (Tape & Tape, 2015).

3.4.2 Grid search for the optimal moment tensor

For practical reasons, we perform two grid searches. The first is a coarse grid search of 100,000 moment tensors, with each moment tensor searching over a range of M_w magnitudes in 0.1 intervals and source depths in 1 km intervals. This first search provides the best-fitting magnitude and depth.

The second search is a fine grid search of $10,000,000$ moment tensors, with each moment tensor represented by $M = (v, w, \kappa, \sigma, h)$. For each moment tensor in the grid search, we evaluate the misfit function. If first-motion polarity measurements are used, we also compute the misfit between observed and predicted first-motion polarities for each moment tensor in the grid.

3.4.3 Confidence curves for moment tensors

Our grid search of moment tensor space provides a global minimum M_0 of the misfit function, as well as a complete view of how the misfit function varies over the full space. Tape & Tape (2016) provided an approach to distilling the complexity of a misfit function into a 'confidence curve' $\mathscr{P}(V)$, which provides the probability as a function of fractional volume of moment tensor space, measured from M_0. The slope of the confidence curve at the origin (M_0) is proportional to the probability $p(M_0)$. The area under the confidence curve provides the confidence parameter $\mathscr{P}_{\text{AV}}$.

Application of the confidence curves for double couple moment tensors was presented in Silwal & Tape (2016). The extension to full moment tensors involves replacing the homogeneous probability density $V'(\omega)$ with one that is appropriate for full moment tensors. As established in Tape & Tape (2016) (see their fig. 4a). For full moment tensors, $V'(\omega) = \frac{8}{3\pi} \sin^4 \omega$ (Tape & Tape, 2016, eq. 29).

As described in Silwal & Tape (2016), a choice of a constant k is needed when converting the misfit function $\Phi(M)$ into a posterior probability function $p(\mathbf{m}) \propto e^{-k\Phi(M)}$.

3.5 Results

Ideally we want to find a moment tensor that produces synthetic seismograms that fit all three components of all available broadband seismograms. This is impractical, mainly due to the high-frequency portions of the seismic wavefield that cannot be fit using 1D (or even 3D) seismic ve-

locity models. Therefore the observed and synthetic seismograms are filtered with a minimum period, e.g., 10–20 s in Ford et al. (2009). Filtering with a maximum period (e.g., 50 s) is also needed in order to suppress contaminating noise at the longest periods. For example, most of the events in Ford et al. (2009) were bandpass filtered 20–50 s; at these periods, the seismograms exhibit surface waves only. Removal of spurious waveforms or stations further reduces the amount of seismic wavefield that is being fit.

To fit the most of the seismic wavefield, we try to use the broadest period range, the largest number of stations, and a combination of body waves and surface waves. These choices involve substantial exploration of parameters, and they depend strongly on the event magnitude and particular regional settings.

3.5.1 Nevada earthquakes

The Little Skull Mountain of 1992-06-29 occurred inside the Nevada Test Site (Figure 3.1) and is the largest earthquake analyzed by Ford et al. (2009). It is notable for its size ($M_w > 5$) and its occurrence near Yucca Mountain, which, at the time, was under consideration as storage site for nulcear waste. Reported magnitude values include M_S 5.4 (Gomberg & Bodin, 1994), M_L 5.6 (Harmsen, 1994), M_w 5.6 (Lohman et al., 2002; Ford et al., 2009), and M_w 5.7 (Dziewonski et al., 1981; Ekström et al., 2012). The Little Skull Mountain earthquake occurred 22 hours after the M_w 7.3 Landers, California, earthquake. Gomberg & Bodin (1994) concluded that seismic waves from the Landers earthquake dynamically triggered the Little Skull Mountain earthquake. Table 1 of Lohman et al. (2002) summarizes several studies of the source parameters of the Little Skull Mountain earthquake.

Our moment tensor inversions for the Little Skull Mountain earthquake used 15 broadband stations (Table 3.1). For our first inversion, we assume a double couple moment tensor and include body waves (filtered 1–4 s) and surface waves (filtered 10–50 s). We first perform a coarse search over magnitude, depth, strike, dip, and rake, to determine the best-fitting depth and magnitude. Figure 3.2 reveals an estimated depth of 9–20 km and an estimated magnitude of M_w 5.2. The depth search over full moment tensor space provides similar results, with a best-fitting depth of 10 km (Figure 3.3). We use 10 km for the estimated depth, based on consensus from previous studies, several of which are more sensitive to depth estimation (Lohman et al., 2002, tab. 1).

With the depth and magnitude fixed, we then perform a fine grid search over the space of strike, dip, and rake. The best-fitting focal mechanism and waveform fits are shown in Figure 3.4. Synthetic seismograms from the 1D model are able to fit the main surface wave arrivals on the data, but they are not able to fit the complexities caused by 3D structure, such as for paths across

the San Joaquin Valley and Sierra Nevada. These effects are diminished when filtering seismograms with a larger minimum period (such as 20 s instead of 10 s).

Our misfit analysis of double couple moment tensors was presented in Silwal & Tape (2016) for Alaska earthquakes. Application to the Little Skull Mountain earthquake is shown in Figure 3.5. Figure 3.5i provides a sampling of 20 beachballs from the posterior distribution; we see that a normal-fault mechanism is preferred, but that the data allow for some notable deviations. An optimal confidence curve is one that has a steep slope at the origin and then rises all the way to $\mathscr{P}(V) \approx 1$, such that $\mathscr{P}(V)$ makes the shape of a Γ. For the Little Skull Mountain earthquake, the confidence curve has a steep slope at the origin but then reveals a more gradual rise, indicating that the probability for the solution is encountered gradually as one moves away from the global minimum moment tensor solution.

The full moment tensor solution for Little Skull Mountain (Figure 3.6) reveals a minor improvement of waveform fits (VR 30.6 vs 28.2). Our initial misfit analysis of full moment tensors was presented in Alvizuri & Tape (2016) for events at Uturuncu volcano. Application to the Little Skull Mountain earthquake is shown in Figure 3.7. The best-fitting solution is close to the deviatoric arc, with lune longitude $\gamma = -14^\circ$ and lune latitude 3°. In the discussion we will revisit the double couple versus full moment tensor inversion results.

Within the moment tensor inversions, time shifts are applied to the synthetic waveforms as an attempt to account for the approximateness of our layered velocity model. Figure 3.8 shows the time shifts of Rayleigh waves and Love waves for the solution in Figure 3.6. The time shifts provide a perspective on potential cycle-skipping of waveform fits, since stations in the same azimuth should have time shifts with the same sign. The time shifts in Figure 3.6 exhibit systematic variations with azimuth that we attribute to differences in 3D structure. The sign discrepancy between time shifts for Love and Rayleigh waves suggests the presence of crustal anisotropy or that that 1D model needs to be adjusted in the shallowest layer, where the Love and Rayleigh waves have differing sensitivities. The plots also reveal stations that are nodal to the mechanism. At these stations, the P and Rayleigh waves can be low amplitude and possibly distorted by 3D structure effects.

3.5.2 Nevada nuclear tests

Following Ford et al. (2009), we use the 1991-09-14 HOYA nuclear test to illustrate the waveform fits and misfit analysis. For HOYA we use 14 stations and filter surface waves at 10–50 s and body waves at high frequencies (0.8–10 Hz). For the LLNL stations we use the 'HF' waveforms for the body waves and 'LF' waveforms for the surface waves. (These waveforms are recorded by

different sensors.) For the body waves, we align the synthetic P waves on the observed P onset times and then allow a time shift of only ± 0.5 s.

The waveform fits and misfit analysis for HOYA are shown in Figures 3.9 and 3.10. The best-fitting moment tensor is at $(-5^\circ, 66^\circ)$ on the lune, within the isotropic region defined by all-positive eigenvalues. The region of lowest fit is tightly constrained around the best-fitting solution, but there are also two other local minima in moment tensor space (Figure 3.10). Some local minima—for example the negative isotropic local minimum in Figure 3.10—arise from cycle-skipping, a topic we will discuss later. Time shift plots for HOYA are shown in Figure 3.11.

We calculate moment tensor solutions for all 32 events from Ford et al. (2009). The events of Ford et al. (2009) are represented as beachballs on the lune in Figure 3.12c. We also plot the beachballs on the *vw* rectangle, which has an advantage over the lune in that distances on the plot better reflect distances between moment tensors. As an example, the 17 explosions from Ford et al. (2009) are spread out on the lune but are close together on the rectangle, indicating that the moment tensors are quantifiably very similar to each other.

3.5.3 Uturuncu volcanic events

We reproduce the results from Alvizuri & Tape (2016), but using a modified misfit function. Previously we excluded any moment tensor that had any disagreement between its predicted first-motion polarities and the observed first-motion polarities. The modified misfit function balances the polarity misfit with the waveform misfit. This means that the misfit function is plotted on the entire lune, rather than on a subregion, as in Alvizuri & Tape (2016).

Figure 3.12a shows the full moment tensor catalog for 63 small ($M_w < 3$) events at Uturuncu volcano. Most events in the catalog have a positive isotropic component ($\delta < 0^\circ$). We show the beachballs on a plot of the *vw* rectangle, which is more appropriate than the lune when the intent is to represent distances in moment tensor space. All-outward beachballs (with all positive eigenvalues) are quite similar to each other; as we might expect, they occupy a much larger region on the lune than they do on the *vw* rectangle.

3.5.4 Alaska earthquakes

We apply the analysis of Alvizuri & Tape (2016) to the 21 earthquakes of Silwal & Tape (2016). No first-motion polarities were used, so the misfit function uses only waveform differences. Figure 3.12b shows the full moment tensor solutions on the lune and on the *vw* rectangle. While some earthquakes exhibit a possibly spurious, negative isotropic component, most events are quite close to the double couple at the center of the lune.

3.6 Discussion

Earthquakes are useful for calibrating the results from non-earthquake events, such as nuclear explosions. Importantly, the full moment tensor inversions for earthquakes need to be performed with conditions that are as close to possible as the non-earthquake events, notably: same stations, same time period (meaning same station metadata), similar epicentral region (similar paths). This was the motivation behind the event selection in Ford et al. (2009).

Earthquake mechanisms estimated as full moment tensors tend to cluster near the double couple region of source type space, as we might hope. However, the spread of best-fitting moment tensors can deviate significantly from the ideal double couple, as shown in Dreger et al. (2012) and Boyd et al. (2015) for a set of 828 events in the Berkeley Seismological Laboratory catalog. The Berkeley moment tensor solutions typically use <8 stations and are based on low-pass-filtered surface waves (Pasyanos et al., 1996; Dreger et al., 1998). By comparison, our full moment tensor analysis of 21 Alaska earthquakes uses dozens of stations and also includes body waves. The moment tensors are more tightly clustered around the double couple at the center of the lune (Figure 3.12b). This suggests that improved data coverage and use of body waves can diminish the spread in source types that are observed for sets of earthquakes.

We further examine the double couple constraint with two earthquakes in Figure 3.13. Because the full space of moment tensors is larger than the subspace of double couple moment tensors, the best-fitting full moment tensor will always provide a better fit to data than the double couple. The challenge is to determine whether the improvement is good enough to warrant invoking a physical model (e.g., opening across a fault) over the traditional model of shear faulting. For the two earthquakes in Figure 3.13, the double couple is within the source type region of good waveform fits and therefore we would attribute deviations from the double couple to variations in the data and modeling.

For the moment tensor inversions in this study we have included waveform fits for body waves. To examine the influence of body waves, we performed separate inversions with body waves only, surface waves only, and both combined. Results for the Little Skull Mountain earthquake and the HOYA nuclear test are shown in Figure 3.14. For the Little Skull Mountain earthquake we see that all three mechanisms are notably different, though they all share a white central region and solid regions to the northwest and southeast. The body+surf lune plot (Figure 3.13c) appears to be a blend of the lune plots for the body-only (Figure 3.13a) and surface-only (Figure 3.13b) cases. Note that the magnitude estimate from body waves only is lower than the overall estimate (M_w 4.9 vs M_w 5.2).

For HOYA, the lune plot for body+surf (Figure 3.13f) reveals multiple good-fitting regions, some of which are present in the body-only (Figure 3.13d) and surface-only (Figure 3.13e) lune

plots. Although first-motion polarities are not used within the inversion, each mechanism predicts outward first-motions at all stations.

It is possible that the mechanisms obtained from high-frequency body waves could differ from the mechanisms obtained from long-period surface waves. This could arise from time-dependent complexity in the source process, whereby the initial slip is responsible for the body waves and later, longer-duration slip is responsible for generating surface waves. Therefore we must be careful in interpreting differences in Figure 3.14, since some could be real, rather than caused by errors in modeling or data.

Our magnitude estimates for the Little Skull Mountain earthquake and for HOYA are lower than those in the published literature. Our M_{w} 5.2 estimate for Little Skull Mountain compares with M_{w} 5.6 from Lohman et al. (2002); Ford et al. (2009) and M_{w} 5.7 from the GCMT catalog. Further work, including testing of different velocity models and attenuation models, is needed to examine this discrepancy.

The application of time shifts to synthetic seismograms in moment tensor inversions is a widely used practice that can be both subtle and dangerous. As an extreme example, the moment tensor $-M_0$ will exhibit the same relative variations in amplitudes as the best-fitting moment tensor M_0. While the inclusion of first-motion polarity measurements can distinguish between these extreme cases, there are other cases that are difficult. With only ten or so waveforms, as in the case of the NTS events (Table 3.1), a single misaligned waveform can influence the solution. One challenge is that the prospects of cycle skipping—misalignment of the synthetic wave with the observed wave—increase as we decrease the period content.

The best approach to eliminating time shifts would be to use a 3D velocity model that accurately predicts the arrival times of all waves used in the moment tensor inversion. For us, this would require accurate prediction of the seismic wavefield for periods ≥ 1 s. Such a regional model does not exist for any active tectonic setting, including the western United States. Cycle skipping of surface waves is particularly problematic, so one could have the more realistic goal of eliminating time shifts for periods ≥ 5 s. With dense data arrays and significant computational modeling, it is possible to fit the seismic wavefield at these periods (Tape et al., 2009; Lee et al., 2014). To integrate such a model into a moment tensor inversion would require replacing the inexpensive, efficient calculation of 1D synthetic seismograms with expensive calculation of 3D synthetic seismograms from wavefield simulations (Komatitsch et al., 2004; Zhao et al., 2006; Lee et al., 2011).

3.7 Summary

We present full moment tensor solutions, with uncertainties, for three sets of events: 21 earthquakes in southern Alaska, 63 events at Uturuncu volcano, Bolivia, and 29 events at the Nevada Test Site. We characterize each event as a point-source moment tensor with a fixed epicenter and origin time. The source time function is a trapezoidal function whose width scales with magnitude. We perform a separate grid search over depth and magnitude, and our emphasis on uncertainty estimation is with the 5D space of normalized moment tensors.

Our key findings are as follows:

1. The misfit function in moment tensor space exhibits local minima and other complexities (e.g., Figure 3.10). These reveal the importance of evaluating the misfit function over the full space of moment tensors, as opposed to linearized inversions, which may lead into an incorrect local minimum.

2. The complexities of the misfit function can be distilled into a confidence curve $\mathscr{P}(V)$ that adjusts the posterior probability for the homogeneous probability of uniform moment tensors (Tape & Tape, 2016; Silwal & Tape, 2016). The area under the confidence curve is the confidence parameter $\mathscr{P}_{\text{AV}}$.

   Even in cases where moment tensor space is uniformly parameterized (e.g., Stähler & Sigloch, 2014), there is still a benefit to the confidence curve in that it can account for the 'imprinted' influence of the homogeneous probability for moment tensors.

3. We present a high-quality catalog of full moment tensors from the Nevada Test Site, building upon the efforts of Ford et al. (2009). In comparison with Ford et al. (2009), we include more stations, we use a lower minimum period (10 s) for all events, and we include (regional) body waves in all inversions. The inclusion of body waves improves the coverage of the source hemisphere, since the body-wave take-off angles tend to be steep (and downward), whereas surface-wave paths are near horizontal.

   Further efforts to include first-motion polarity measurements from short-period stations (Harmsen, 1994) could result in moment tensor solutions with higher confidence than those presented here.

Additional work is needed to improve our understanding of the theory and application of moment tensor confidence curves. The majority of choices are made within the misfit function, which includes time windowing, weighting, choice of norm, and time shifting of synthetic seismograms. For example, a more complete representation of data covariance terms (e.g., Stähler & Sigloch, 2016; Mustać & Tkalčić, 2016) could eliminate the need for a scale factor. The use of 3D synthetic

seismograms could lessen the need for time shifts, if the 3D velocity model is accurate. Some questions can be adequately addressed without real data within synthetic inversions (Wéber, 2006; Walter et al., 2010; Stierle et al., 2014; Staněk et al., 2014).

Our primary goal has been to characterize uncertainties of moment tensors. This provides a starting point for interpreting the results in the context of physical models, such as those discussed in Tape & Tape (2013) or Patton & Taylor (2011). We can interpret any full moment tensor as a one-process model of an oblique opening crack (Minson & Dreger, 2008) or as a two-process model of a tensional or compressional crack combined with shear slip within the same crack plane (Aki & Richards, 2002). More complex source processes have been proposed, but they cannot be distinguished or evaluated using the typical set of seismic waveforms.

3.8 Acknowledgments

We thank Matt Gardine and Michael West for help with the database of Walter et al. (2006). This project was supported by Air Force Research Laboratory (contract FA9453-15-C-0063) and by the National Science Foundation (grant EAR-1215959).

Table 3.1: Nuclear explosions, earthquakes, and mine collapses from Ford et al. (2009), re-examined in this study.

				Depth	# stations used (# available)			
Event name	Origin time	Longitude	Latitude	(m)	IRIS	NCEDC	LLNL	Total
KERNVILLE	1988-02-15 18:10:00.09	-116.4720	37.3140	542	3 (5)	3 (4)	3 (6)	9 (15)
AMARILLO	1989-06-27 15:30:00.02	-116.3540	37.2750	640	6 (7)	3 (6)	3 (6)	12 (19)
DISKO ELM	1989-09-14 15:00:00.10	-116.1640	37.2360	261	7 (8)	1 (5)	3 (8)	11 (21)
HORNITOS	1989-10-31 15:30:00.09	-116.4920	37.2630	564	9 (9)	6 (6)	0 (8)	15 (23)
BARNWELL	1989-12-08 15:00:00.09	-116.4100	37.2310	601	11 (11)	8 (8)	3 (8)	22 (27)
METROPOLIS	1990-03-10 16:00:00.08	-116.0560	37.1120	469	3 (10)	4 (7)	3 (8)	10 (25)
BULLION	1990-06-13 16:00:00.09	-116.4210	37.2620	674	11 (11)	7 (7)	4 (8)	22 (26)
AUSTIN	1990-06-21 18:15:00.00	-116.0050	36.9930	350	11 (11)	4 (6)	3 (8)	18 (25)
HOUSTON	1990-11-14 19:17:00.07	-116.3720	37.2270	594	2 (13)	4 (5)	3 (8)	9 (26)
COSO	1991-03-08 21:02:45.08	-116.0750	37.1040	417	21 (21)	1 (1)	3 (6)	25 (28)
BEXAR	1991-04-04 19:00:00.00	-116.3140	37.2960	629	10 (10)	0 (0)	3 (6)	13 (16)
HOYA	1991-09-14 19:00:00.08	-116.4290	37.2260	658	9 (25)	2 (4)	3 (6)	14 (35)
LUBBOCK	1991-10-18 19:12:00.00	-116.0460	37.0630	457	7 (23)	1 (4)	3 (6)	11 (33)
BRISTOL	1991-11-26 18:35:00.07	-116.0700	37.0960	457	23 (23)	4 (4)	3 (6)	30 (33)
JUNCTION	1992-03-26 16:30:00.00	-116.3610	37.2720	622	7 (27)	2 (4)	3 (6)	12 (37)
HUNTERS TROPHY	1992-09-18 17:00:00.08	-116.2110	37.2070	385	12 (34)	8 (12)	1 (2)	21 (48)
DIVIDER	1992-09-23 15:04:00.00	-115.9890	37.0210	340	15 (36)	10 (14)	0 (2)	25 (52)
Little Skull Main	1992-06-29 10:14:21.89	-116.2722	36.6385	4530	9 (50)	6 (12)	0 (1)	15 (63)
Little Skull Aftershock	1992-07-05 06:54:10.72	-116.0178	36.6767	6590	– (50)	– (12)	– (2)	– (64)
Timber Mountain	1995-07-31 12:34:45.03	-116.2057	37.1363	7010	– (52)	– (26)	– (0)	– (78)
Amargosa	1996-09-05 08:16:56.09	-116.3378	36.6827	5000	– (49)	– (30)	– (0)	– (79)
Groom Pass	1997-04-26 01:49:35.58	-115.9220	37.1987	6040	– (78)	– (32)	– (23)	– (133)
Indian Springs	1997-06-14 19:48:19.93	-115.8133	36.5172	7020	– (74)	– (32)	– (0)	– (106)
Calico Fan	1997-09-12 13:36:54.20	-116.1182	36.8422	16560	– (163)	– (34)	– (2)	– (199)
Warm Springs	1998-12-12 01:41:30.33	-116.1605	37.5437	2870	– (145)	– (38)	– (3)	– (186)
Frenchman Flat 1	1999-01-23 03:00:34.82	-116.0277	36.7640	7410	– (146)	– (40)	– (25)	– (211)
Frenchman Flat 2	1999-01-27 10:44:17.80	-115.4578	36.7790	8850	– (95)	– (40)	– (26)	– (161)
Little Skull	2002-06-14 12:40:45.82	-116.3448	36.6438	8750	– (0)	– (40)	– (66)	– (106)
Ralston	2007-01-24 11:30:16.10	-117.0986	37.4133	6090	– (441)	– (19)	– (0)	– (460)
ATRISCO Hole	1982-08-05 14:21:00	-116.0065	37.0842	640	– (3)	– (0)	– (4)	– (7)
Trona Mine 1	1995-02-03 15:26:10.69	-109.64	41.53	1000	– (37)	– (21)	– (3)	– (61)
Trona Mine 2	2000-01-30 14:46:51.31	-109.68	41.46	1000	68 (184)	1 (36)	0 (0)	69 (220)

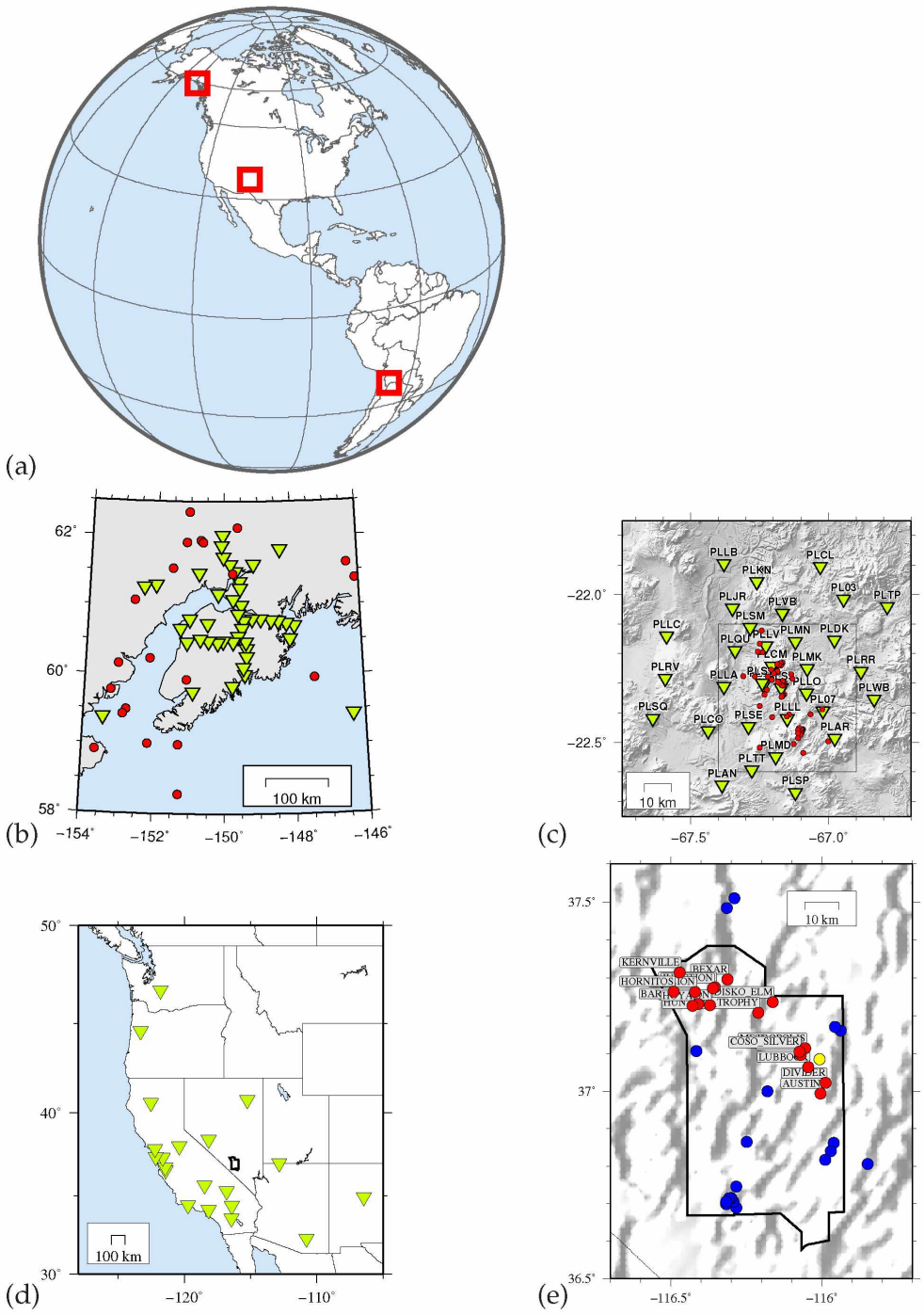

Figure 3.1: Three study regions of Alaska, Bolivia, and the Nevada Test Site. (a) Global perspective showing our three study regions. (b) 21 earthquakes in southern Alaska. (c) 63 events at Uturuncu volcano, Bolivia. (d) Western United States, showing Nevada Test site (outlined). (e) Zoom-in on Nevada Test Site. Nuclear explosions (17) are red, earthquakes (12) are blue, and collapses (3) are yellow.

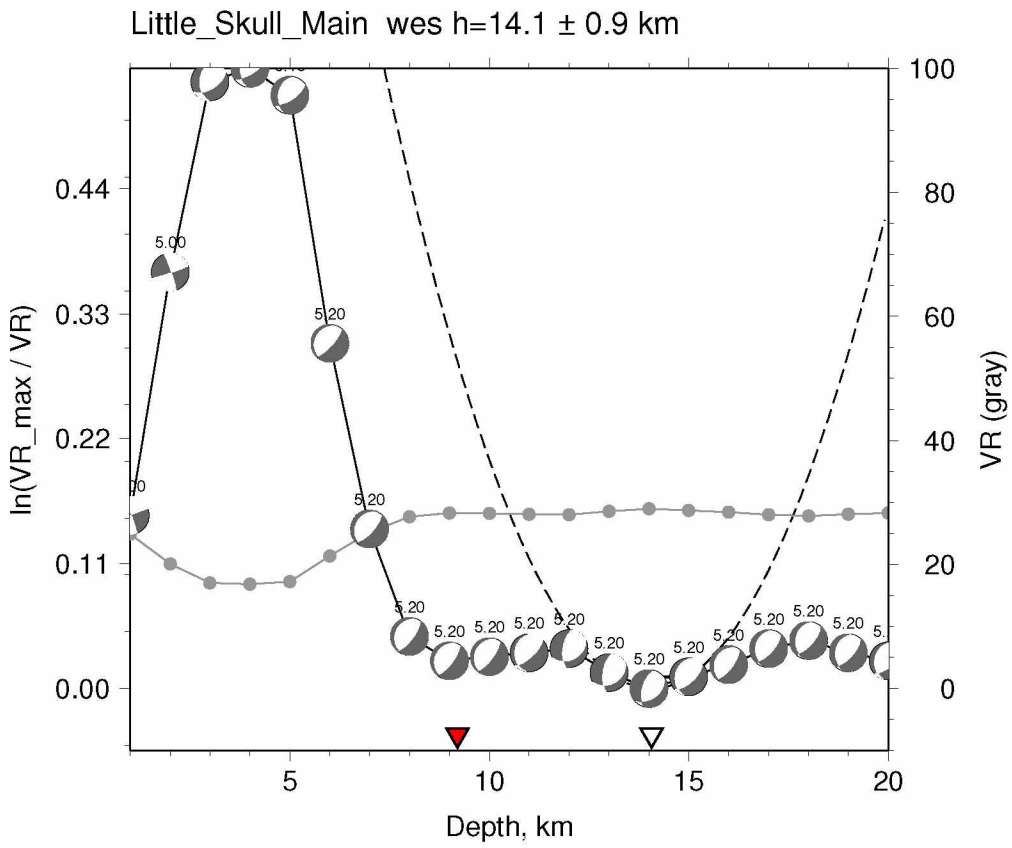

Figure 3.2: Grid search over depth for the best double couple moment tensor for the Little Skull Mountain earthquake. Each beachball shows the best-fitting moment tensor (and magnitude) for a particular depth. The right axis shows the variance reduction (light gray curve). The left axis shows the deviation in variance reduction from the global minimum (black curve) at 14 km. The white triangle is the global minimum, the red triangle is the catalog depth from Walter et al. (2006). The plot reveals an estimated depth between 9 and 20 km.

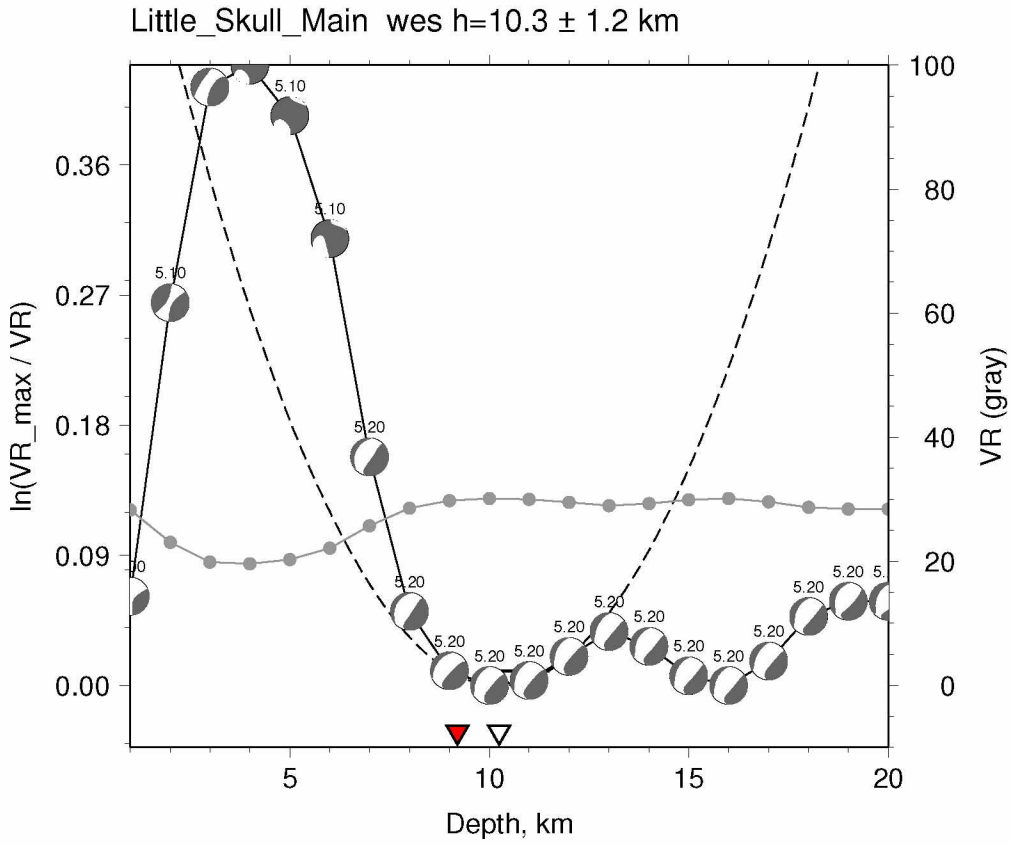

Figure 3.3: Same as Figure 3.2, but for a full moment tensor instead of a double couple moment tensor. The estimated depth is between 9 and 18 km, with a misfit minimum at 10 km.

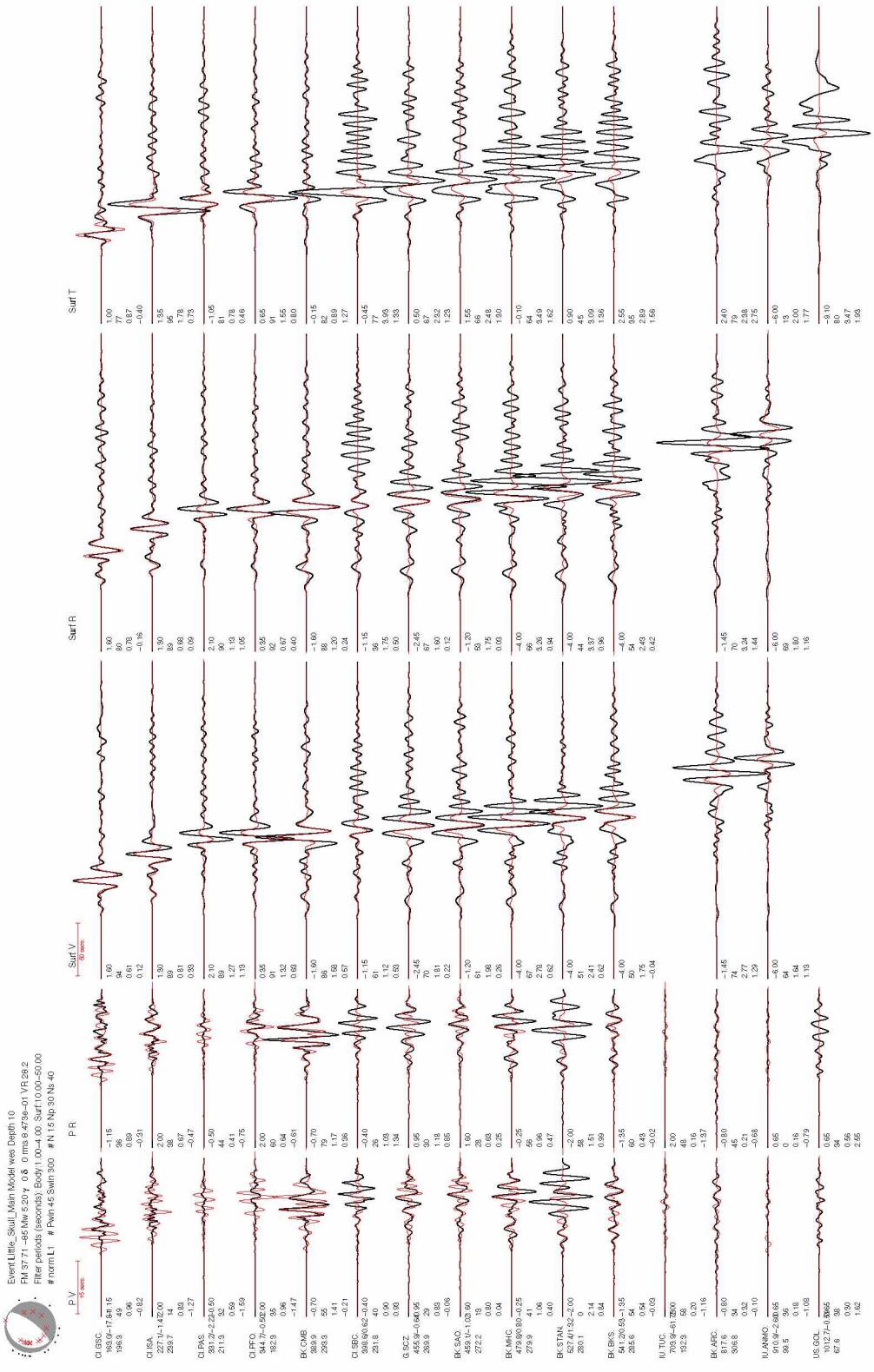

Figure 3.4: Waveform fits for the Little Skull Mountain earthquake, assuming a double couple moment tensor. Recorded waveforms (black) and synthetic waveforms (red) are fit within five different time windows: P-vertical, P-radial, Surf-vertical, Surf-radial, and Surf-transverse.

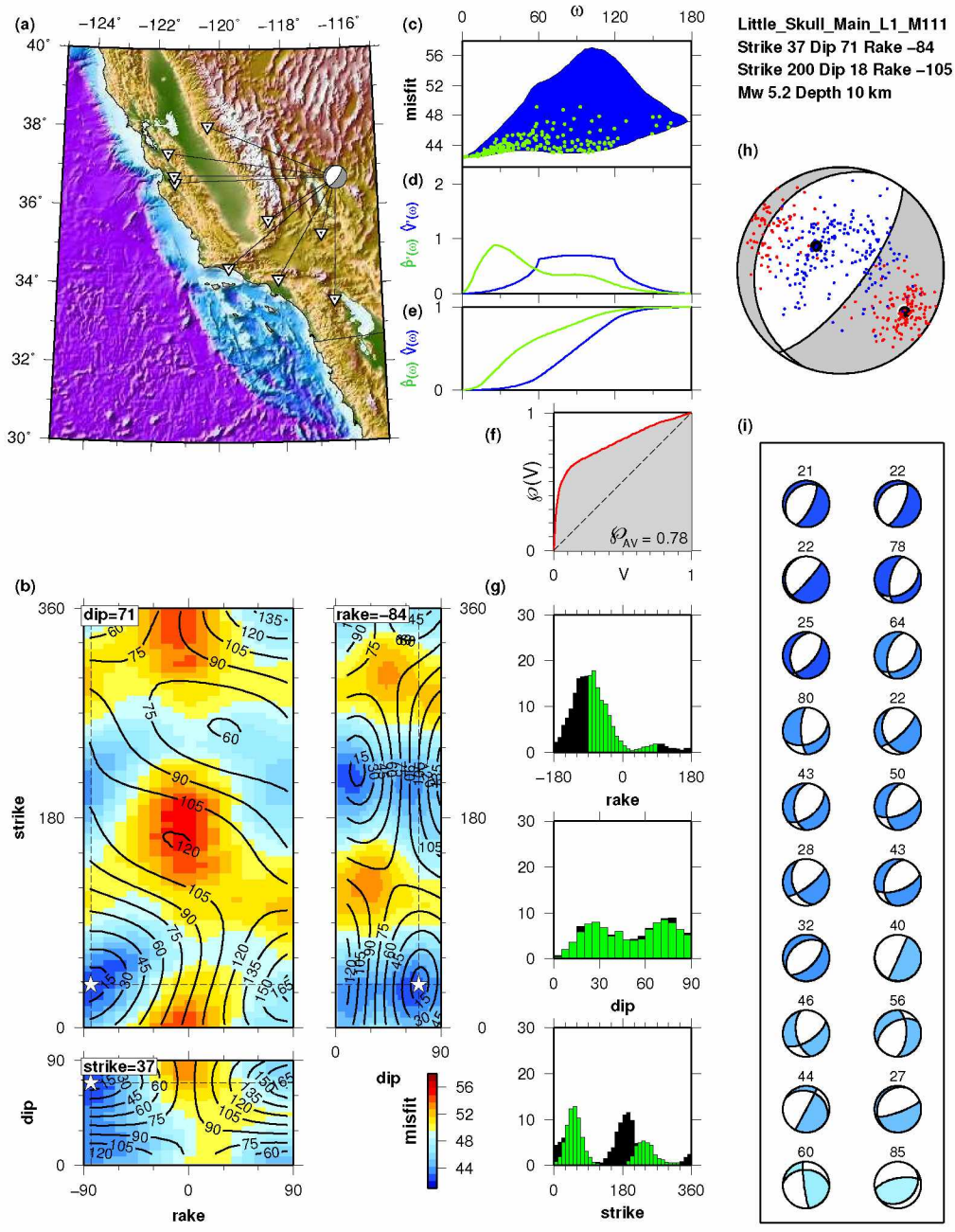

Figure 3.5: Misfit summary for the Little Skull Mountain earthquake when assuming a double couple moment tensor. The confidence curve $\mathscr{P}(V)$ is shown in (f). See text and Silwal & Tape (2016) for details.

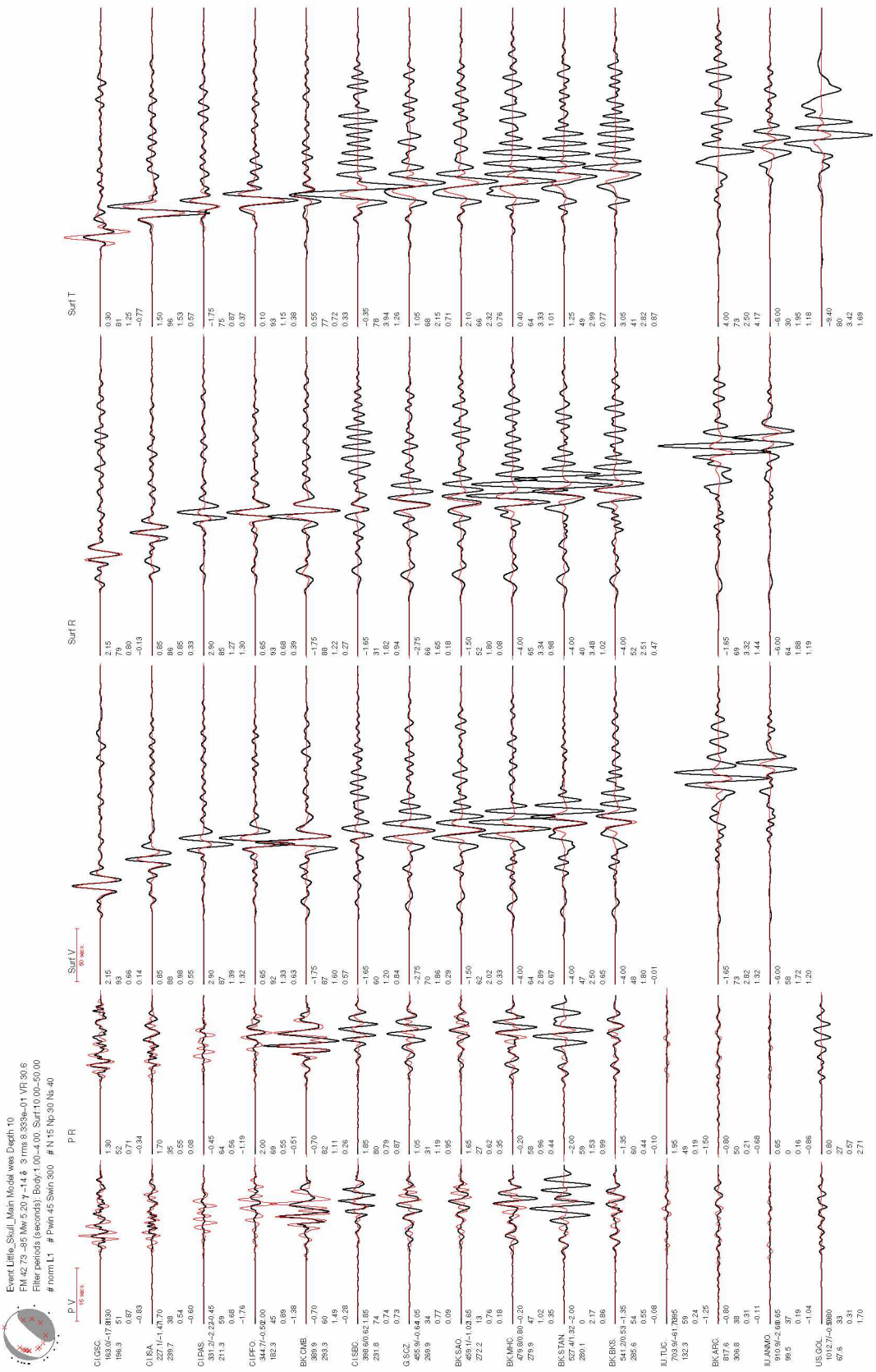

Figure 3.6: Waveform fits for the Little Skull Mountain earthquake, assuming a full moment tensor. See misfit analysis in Figure 3.7.

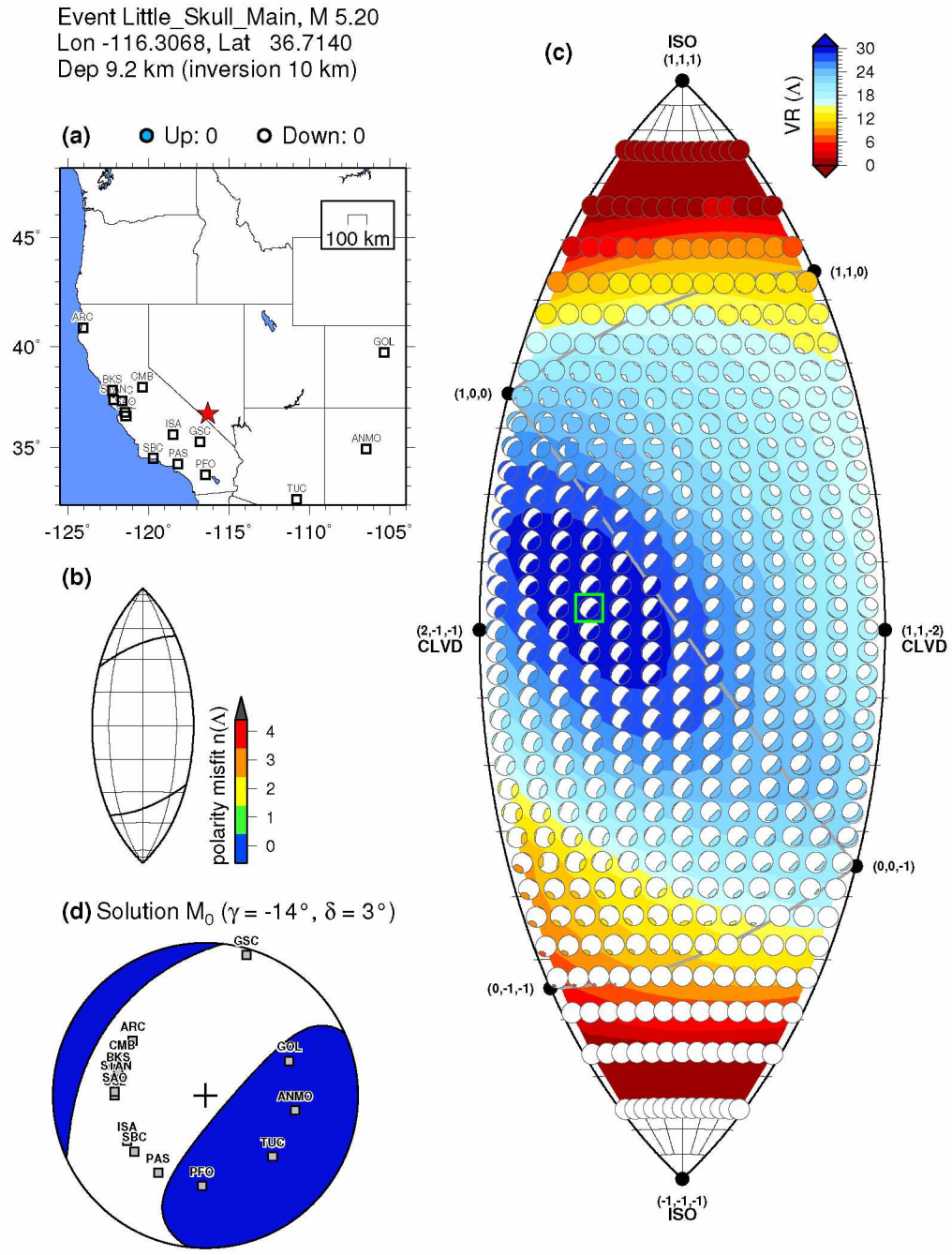

Figure 3.7: Misfit summary, after Alvizuri & Tape (2016) (fig. 6), for the Little Skull Mountain earthquake. (a) Map showing epicenter and stations. (b) Lune plot related to first-motion polarities, which were not used in this case. (c) Variance reduction on the lune, with the best-fitting moment tensor M_0 exhibiting the highest variance reduction. (d) Best-fitting moment tensor M_0, with lune longitude $\gamma = -14^\circ$ and lune latitude $\delta = 3^\circ$. See waveform fits in Figure 3.6.

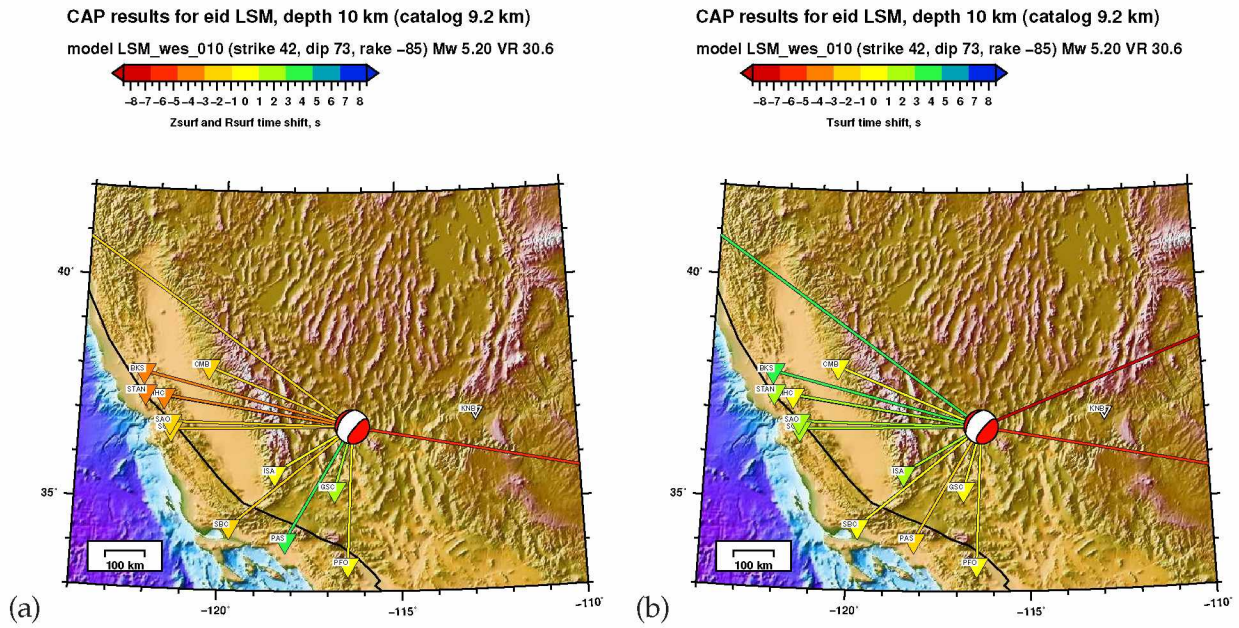

(a) (b)

Figure 3.8: Surface wave time shifts used in the full moment tensor inversion for the Little Skull Mountain earthquake (Figure 3.6). (a) Rayleigh waves on vertical and radial components. (b) Love waves on transverse component.

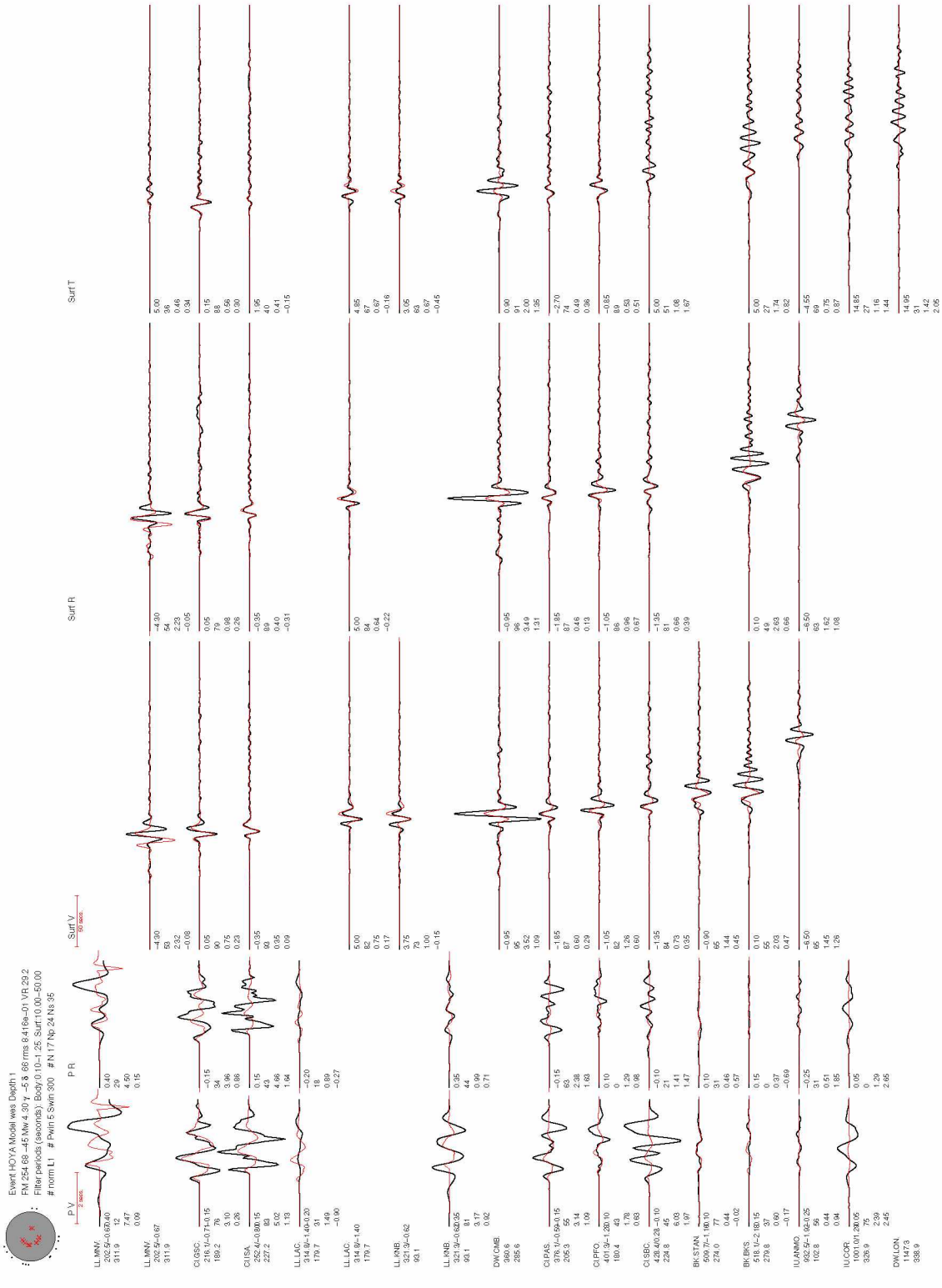

Figure 3.9: Waveform fits for the HOYA nuclear test. See Figure 3.10 for the misfit analysis.

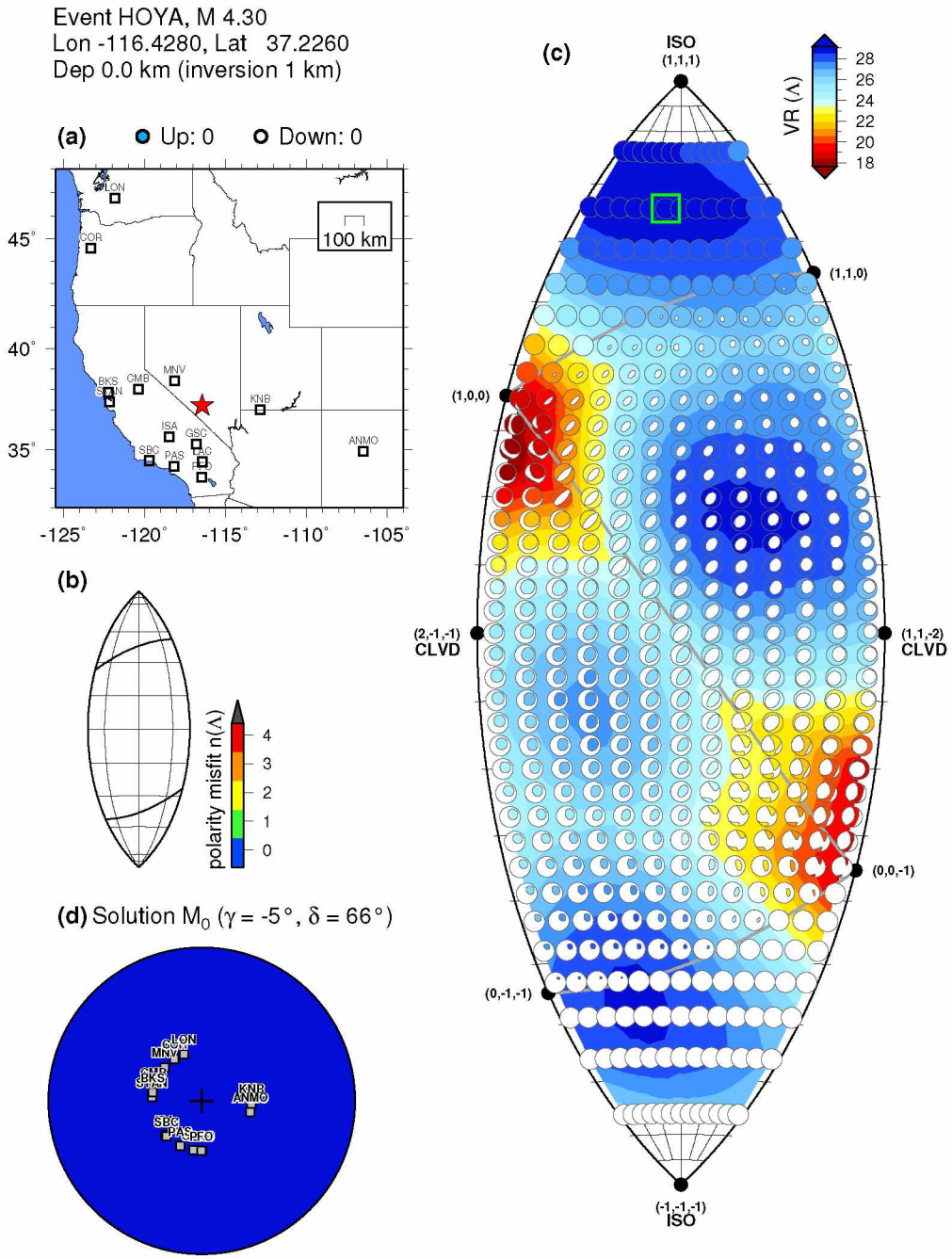

Figure 3.10: Same as Figure 3.7, but for the HOYA nuclear test. Waveforms for the best-fitting moment tensor are shown in Figure 3.9.

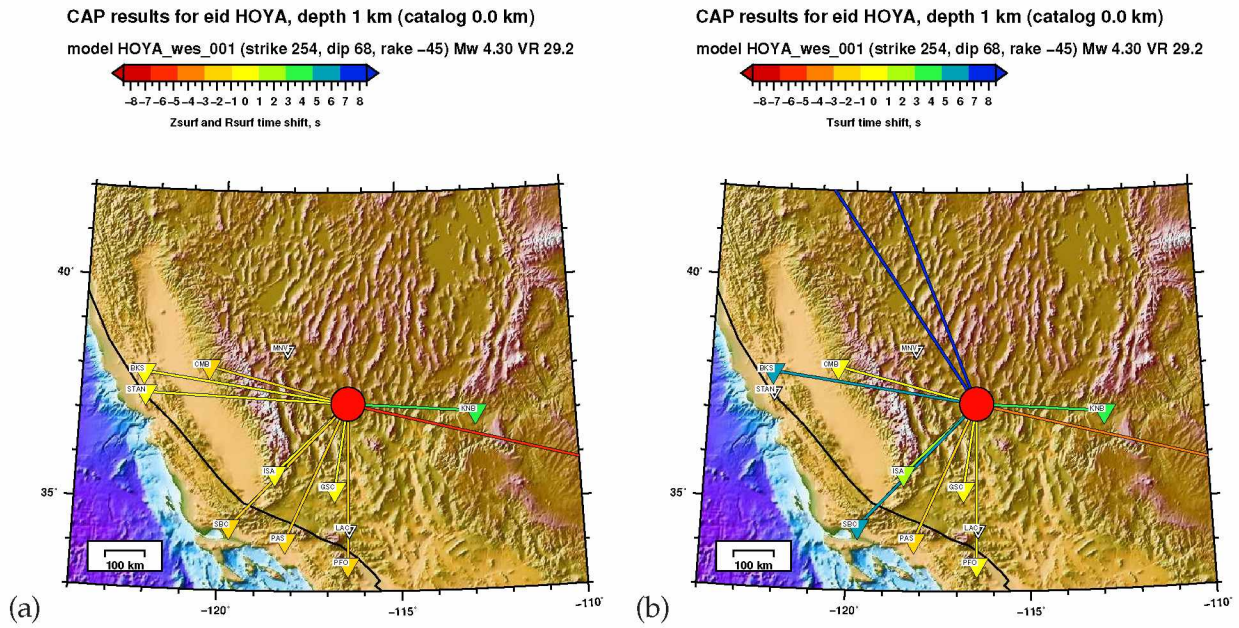

Figure 3.11: Surface wave time shifts used in the full moment tensor inversion for the HOYA nuclear test (Figure 3.9). (a) Rayleigh waves on vertical and radial components. (b) Love waves on transverse component.

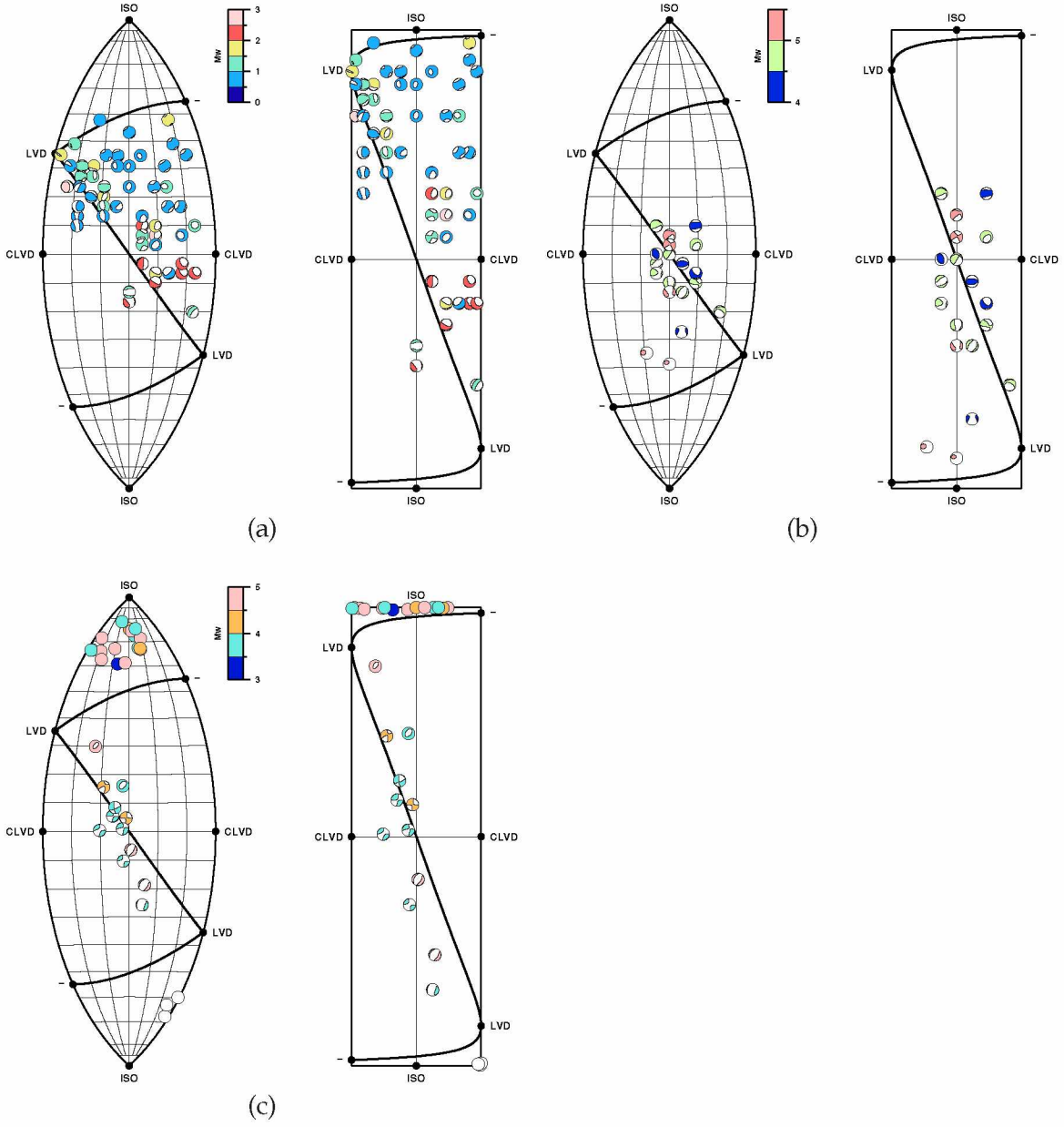

Figure 3.12: Full moment tensor catalogs, plotted on the lune (left) and on the *vw* rectangle (right) (Tape & Tape, 2012, 2015). Beachballs are colored by magnitude. (a) 63 events from Uturuncu volcano, Bolivia. (b) 21 earthquakes from southern Alaska. (c) 29 earthquakes, explosions, and collapses from Nevada Test Site (Ford et al., 2009).

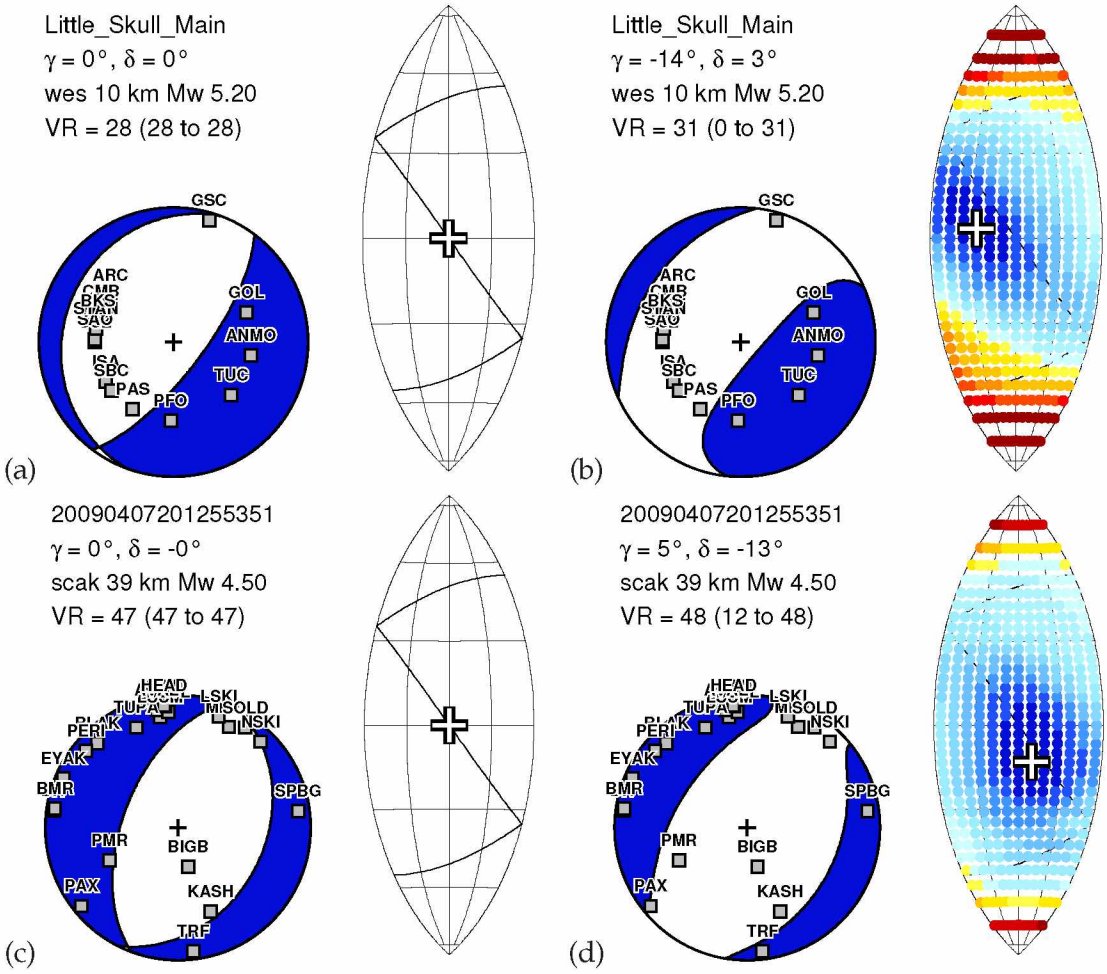

Figure 3.13: Comparison between double couple moment tensors and full moment tensors for two earthquakes. (a) The best-fitting double couple for Little Skull Mountain earthquake on 1992-07-29. (b) The best-fitting full moment tensor for the Little Skull Mountain earthquake. (c)-(d) Same as (a)-(b) but for a high-quality Alaska earthquake on 2007-04-07.

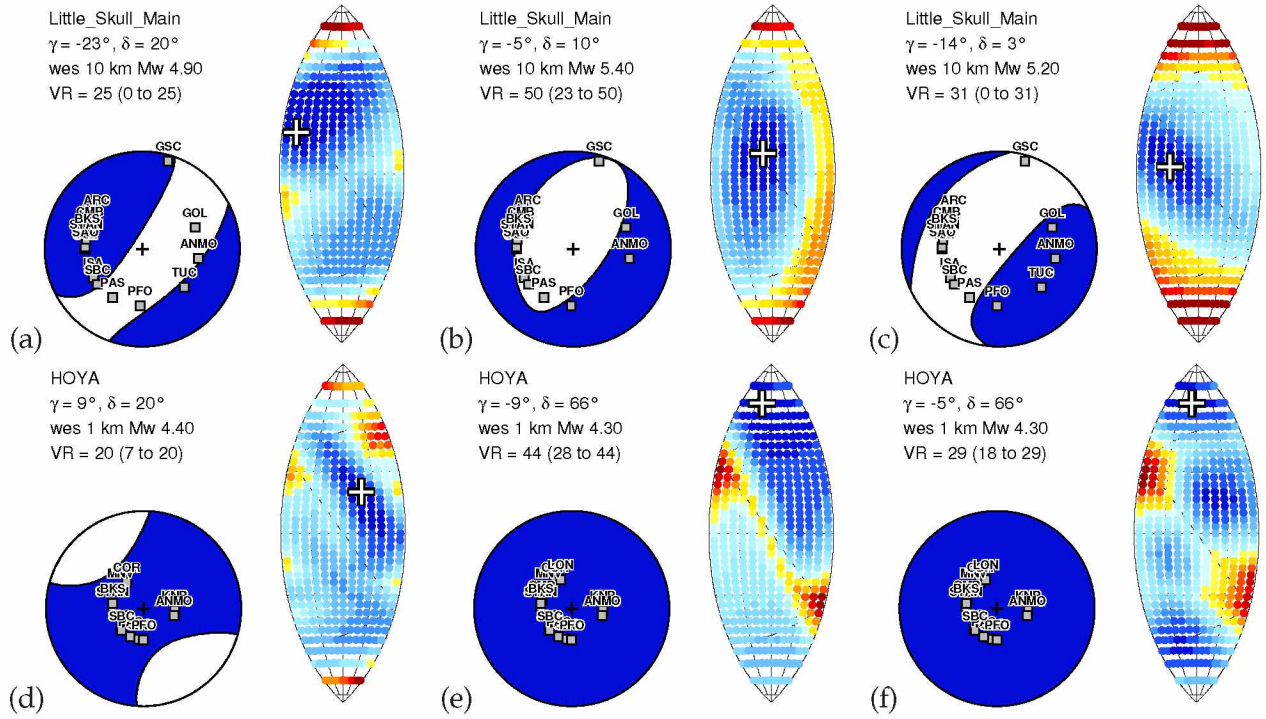

Figure 3.14: The influence of body waves and surface waves on moment tensor inversions. Color scales change for each subplot. (a)-(c) Little Skull Mountain: body waves only, surface waves only, and combined. (d)-(f) HOYA: body waves only, surface waves only, and combined.

3.9 References

Aki, K. & Richards, P. G., 2002. *Quantitative Seismology*, University Science Books, San Francisco, Calif., USA, 2nd edn., 2009 corrected printing.

Alvizuri, C. & Tape, C., 2016. Full moment tensors for small events ($M_W < 3$) at Uturuncu volcano, Bolivia, *Geophys. J. Int.*, **206**, 1761–1783, doi:10.1093/gji/ggw247.

Beyreuther, M., Barsch, R., Krischer, L., Megies, T., Behr, Y., & Wassermann, J., 2010. ObsPy: A Python toolbox for seismology, *Seis. Res. Lett.*, **81**(3), 530–533, doi:10.1785/gssrl.81.3.530.

Boyd, O. S., Dreger, D. S., Lai, V. H., & Gritto, R., 2015. A systematic analysis of seismic moment tensor at The Geysers geothermal field, California, *Bull. Seis. Soc. Am.*, **105**(6), 2969–2986, doi: 10.1785/0120140285.

Dreger, D., Uhrhammer, R., Pasyanos, M., Franck, J., & Romanowicz, B., 1998. Regional and far-regional earthquake locations and source parameters using sparse broadband networks: A test on the Ridgecrest sequence, *Bull. Seis. Soc. Am.*, **88**(6), 1353–1362.

Dreger, D. S., Chiang, A., Ford, S. R., & Walter, W. R., 2012. Refinement of regional distance seismic moment tensor and uncertainty analysis for source-type identification, in *Proceedings of the 2012 Monitoring Research Review: Ground-Based Nuclear Explosion Monitoring Technologies*, pp. 377–386, National Nuclear Security Administration.

Dziewonski, A., Chou, T.-A., & Woodhouse, J. H., 1981. Determination of earthquake source parameters from waveform data for studies of global and regional seismicity, *J. Geophys. Res.*, **86**(B4), 2825–2852, doi:10.1029/JB086iB04p02825.

Ekström, G., Nettles, M., & Dziewoński, A. M., 2012. The global GCMT project 2004–2010: Centroid-moment tensors for 13,017 earthquakes, *Phys. Earth Planet. Inter.*, **200-201**, 1–9, doi: 10.1016/j.pepi.2012.04.002.

Ford, S. R., Dreger, D. S., & Walter, W. R., 2009. Identifying isotropic events using a regional moment tensor inversion, *J. Geophys. Res.*, **114**, B01306, doi:10.1029/2008JB005743.

Ford, S. R., Dreger, D. S., & Walter, W. R., 2010. Network sensitivity solutions for regional moment-tensor inversions, *Bull. Seis. Soc. Am.*, **100**(5A), 1962–1970, doi:10.1785/0120090140.

Gomberg, J. & Bodin, P., 1994. Triggering of the M_S = 5.4 Little Skull Mountain, Nevada, earthquake with dynamic strains, *Bull. Seis. Soc. Am.*, **84**(3), 844–853.

Harmsen, S. C., 1994. The Little Skull Mountain, Nevada, earthquake of 29 June 1992: Aftershock focal mechanisms and tectonic stress field implications, *Bull. Seis. Soc. Am.*, **84**(5), 1484–1505.

Haskell, N., 1964. Total energy and energy spectral density of elastic wave radiation from propagating faults, *Bull. Seis. Soc. Am.*, **54**, 1811–1842.

Keyson, L. & West, M. E., 2013. Earthquake sources near Uturuncu Volcano, Abstract V13B-2603 presented at 2013 Fall Meeting, AGU, San Francisco, Calif., 9-13 Dec.

Komatitsch, D., Liu, Q., Tromp, J., Süss, P., Stidham, C., & Shaw, J. H., 2004. Simulations of ground motion in the Los Angeles basin based upon the spectral-element method, *Bull. Seis. Soc. Am.*, **94**(1), 187–206, doi:10.1785/0120030077.

Krischer, L., Mengies, T., Barsch, R., Beyreuther, M., Lecocq, T., Caudron, C., & Wassermann, J., 2015. ObsPy: a bridge for seismology into the scientific Python ecosystem, *Computational Science & Discovery*, **8**(1), 014003, doi:10.1088/1749-4699/8/1/014003.

Lee, E.-J., Chen, P., Jordan, T. H., & Wang, L., 2011. Rapid full-wave centroid moment tensor (CMT) inversion in a three-dimensional earth structure model for earthquakes in Southern California, *Geophys. J. Int.*, **186**, 311–330, doi:10.1111/j.1365-246X.2011.05031.x.

Lee, E.-J., Chen, P., Jordan, T. H., Maechling, P. B., Denolle, M. A. M., & Beroza, G. C., 2014. Full-3-D tomography for crustal structure in Southern California based on the scattering-integral and the adjoint-wavefield methods , *J. Geophys. Res. Solid Earth*, **119**, 6421–6451, doi:10.1002/2014JB011346.

Lohman, R. B., Simons, M., & Savage, B., 2002. Location and mechanism of the Little Skull Mountain earthquake as constrained by satellite radar interferometry and seismic waveform modeling, *J. Geophys. Res.*, **107**(B6), doi:10.1029/2001JB000627.

Minson, S. E. & Dreger, D. S., 2008. Stable inversions for complete moment tensors, *Geophys. J. Int.*, **174**, 585–592, doi:10.1111/j.1365-246X.2008.03797.x.

Mustać, M. & Tkalčić, H., 2016. Point source moment tensor inversion through a Bayesian hierarchical model, *Geophys. J. Int.*, **204**, 311–323, doi:10.1093/gji/ggv458.

Nayak, A. & Dreger, D. S., 2014. Moment tensor inversion of seismic events associated with the sinkhole at Napoleonville salt dome, Louisiana, *Bull. Seis. Soc. Am.*, **104**(4), 1763–1776, doi:10.1785/0120130260.

Pasyanos, M. E., Dreger, D. S., & Romanowicz, B., 1996. Toward real-time estimation of regional moment tensors, *Bull. Seis. Soc. Am.*, **86**(5), 1255–1269.

Patton, H. J. & Taylor, S. R., 2011. The apparent explosion moment: Inferences of volumetric moment due to source medium damage by underground nuclear explosions, *J. Geophys. Res.*, **116**, B03310, doi:10.1029/2010JB007937.

Pesicek, J. D., Sileny, J., Prejean, S. G., & Thurber, C. H., 2012. Determination and uncertainty of moment tensors for microearthquakes at Okmok Volcano, Alaska, *Geophys. J. Int.*, **190**, 1689–1709, doi:10.1111/j.1365-246X.2012.05574.x.

Pesicek, J. D., Cieślik, K., Lambert, M.-A., Carrillo, P., & Birkelo, B., 2016. Dense surface seismic data confirm non-double-couple source mechanisms induced by hydraulic fracturing, *Geophysics*, **81**(6), KS207–KS217, doi:10.1190/GEO2016-0192.1.

Ross, Z. E., Ben-Zion, Y., & Zhu, L., 2015. Isotropic source terms of San Jacinto fault zone earthquakes based on waveform inversions with a generalized CAP method, *Geophys. J. Int.*, **200**, 1267–1278, doi:10.1093/gji/ggu460.

Šilený, J. & Milev, A., 2006. Seismic moment tensor resolution on a local scale: simulated rockburst and mine-induced seismic events in the Kopanang gold mine, South Africa, *Pure App. Geophys.*, **163**, 1495–1513, doi:10.1007/s00024-006-0089-z.

Silwal, V. & Tape, C., 2016. Seismic moment tensors and estimated uncertainties in southern Alaska, *J. Geophys. Res. Solid Earth*, **121**, 2772–2797, doi:10.1002/2015JB012588.

Stähler, S. C. & Sigloch, K., 2014. Fully probabilistic seismic source inversion – Part 1: Efficient parameterisation, *Solid Earth*, **5**, 1055–1069, doi:10.5194/se-5-1055-2014.

Stähler, S. C. & Sigloch, K., 2016. Fully probabilistic seismic source inversion – Part 2: Modelling errors and station covariances, *Solid Earth*, **7**, 1521–1536, doi:10.5194/se-2016-87.

Staněk, F., Eisner, L., & Moser, T. J., 2014. Stability of source mechanisms inverted from P-wave amplitude microseismic monitoring data acquired at the surface, *Geophys. Prosp.*, **62**, 475–490, doi:10.1111/1365-2478.12107.

Stierle, E., Vavryčuk, V., Šílenỳ, J., & Bohnhoff, M., 2014. Resolution of non-double-couple components in the seismic moment tensor using regional networks—I: a synthetic case study, *Geophys. J. Int.*, **196**, 1869–1877, doi:10.1093/gji/ggt502.

Tape, C., Liu, Q., Maggi, A., & Tromp, J., 2009. Adjoint tomography of the southern California crust, *Science*, **325**, 988–992, doi:10.1126/science.1175298.

Tape, W. & Tape, C., 2012. A geometric setting for moment tensors, *Geophys. J. Int.*, **190**, 476–498, doi:10.1111/j.1365-246X.2012.05491.x.

Tape, W. & Tape, C., 2013. The classical model for moment tensors, *Geophys. J. Int.*, **195**, 1701–1720, doi:10.1093/gji/ggt302.

Tape, W. & Tape, C., 2015. A uniform parameterization of moment tensors, *Geophys. J. Int.*, **202**, 2074–2081, doi:10.1093/gji/ggv262.

Tape, W. & Tape, C., 2016. A confidence parameter for seismic moment tensors, *Geophys. J. Int.*, **205**, 938–953, doi:10.1093/gji/ggw057.

Vavryčuk, V., 2011. Tensile earthquakes: Theory, modeling, and inversion, *J. Geophys. Res.*, **116**, B12320, doi:10.1029/2011JB008770.

Walter, F., Dreger, D. S., Clinton, J. F., Deichmann, N., & Funk, M., 2010. Evidence for near-horizontal tensile faulting at the base of Gornergletscher, a Swiss Alpine Glacier, *Bull. Seis. Soc. Am.*, **100**(2), 458–472, doi:10.1785/0120090083.

Walter, W. R., Smith, K. D., O'Boyle, J. L., Hauk, T. F., Ryall, F., Ruppert, S. D., Myers, S. C., Abbot, R., & Dodge, D. A., 2006. An assembled western United States dataset for regional seismic analysis, ISSO 9660 CD, LLNL release UCRL-MI-222502.

Wéber, Z., 2006. Probabilistic local waveform inversion for moment tensor and hypocentral location, *Geophys. J. Int.*, **165**, 607–621.

Zhao, L., Chen, P., & Jordan, T. H., 2006. Strain Green's tensors, reciprocity, and their applications to seismic source and structure studies, *Bull. Seis. Soc. Am.*, **96**(5), 1753–1763, doi:10.1785/0120050253.

Zhu, L. & Ben-Zion, Y., 2013. Parameterization of general seismic potency and moment tensors for source inversion of seismic waveform data, *Geophys. J. Int.*, **194**, 839–843, doi:10.1093/gji/ggt137.

Zhu, L. & Helmberger, D., 1996. Advancement in source estimation techniques using broadband regional seismograms, *Bull. Seis. Soc. Am.*, **86**(5), 1634–1641.

Zhu, L. & Rivera, L. A., 2002. A note on the dynamic and static displacements from a point source in multilayered media, *Geophys. J. Int.*, **148**, 619–627, doi:10.1046/j.1365-246X.2002.01610.x.

Chapter 4
Conclusion

My research towards this thesis comprises two parts: (1) methodological and computational developments for estimating the seismic full moment tensor and its uncertainty, and (2) application of the method to natural and induced seismic events, and in diverse tectonic settings in the earth. These are described in the next sections.

The tools developed in this thesis are applied for estimating moment tensors to seismic sources such as earthquakes, volcanic, and nuclear explosions. However, these tools can be applied to any seismic source that can be observable by seismic stations. Some applications include glacial events, landslides, and even mineralogical phase transformations in the mantle. Another set of tools developed in this thesis are for estimating moment tensor uncertainties, for appraising their source-types, and appraising their equivalent force systems. Together, these tools provide a foundation for discussion about source processes and their physical mechanisms.

4.1 Methodological development

For this research I worked with an inversion method that relies on the exhaustive exploration over the 6-D space of moment tensors. As I extended this method for the full moment tensor, the space of solutions increased, with a typical inversion requiring a search over 2×10^8 solutions. In the course of this research I developed tools to efficiently estimate seismic full moment tensors, their misfit, and uncertainties. These methodological developments include:

- Develop an inversion routine to utilize a full moment tensor parameterization
- Develop an inversion routine that utilizes an efficient moment tensor sampling from a regular and a random grid
- Parallelize the inversion to run on multiple cores
- Develop methods to analyze the variation of misfit on the space of moment tensors
- Develop methods to analyze the full moment tensor uncertainty
- Develop methods to efficiently compute catalogs of full moment tensors

4.2 Applications

The methodology described above can be applied to wide range of seismic sources, natural and induced, beyond the double-couple. Some of these sources include volcanic, geothermal, glacial, landslides; mining-related such as from roof collapses; induced such as from hydraulic fracturing;

and nuclear explosions. For my current research I applied the method to events from a volcano in Bolivia, to earthquakes in Alaska, to earthquakes in the western U.S., and to nuclear explosions at the Nevadata Test Site in Nevada, U.S. The following sections describe the main findings.

4.2.1 Seismic events at Uturuncu volcano, Bolivia

1. I present a compilation of 63 full moment tensors for events at Uturuncu volcano, Bolivia, for the time period of the PLUTONS array (2010-04-12 to 2012-03-09). The catalog represents the complete set of events for which I could obtain reliable moment tensor solutions. For each event I used as many waveform measurements (both P waves and surface waves) and first-motion measurements as possible.

   In the context of the published literature (Table 2.1), the catalog of moment tensors is large, the events we analyze are small (M_w = 0.3–2.8), the waveforms are high frequency. I present the variations in misfit function over the space of source types for each event.

2. I characterize three subsets of moment tensors within our catalog. One subset, located close to the volcano, contains 6 events with isotropic components whose first-motion polarities exclude the possibility of a double-couple mechanism.

3. These findings of positively isotropic events are in agreement with other studies of full moment tensors in volcanic and geothermal settings (Figure 2.11b). As noted in Tape & Tape (2013), the large spread in source types of previously published events could be explained by a multiple-process model. Alternatively, they could be explained by the classical model, whereby the full moment tensor solutions have large uncertainties is the space of source types (i.e., on the lune). Most previous studies did not provide uncertainty estimates, making interpretation challenging.

   Our plots of misfit $\Phi(\Lambda)$ on the lune (Figure 2.6) are a step toward uncertainty estimation. They show the range of permissible source types. Considering this range, we conclude that the classical model remains a possibility (Section 2.6.4).

4. Full moment tensor inversion of P waveforms at the frequencies used in this study (2–10 Hz) is a delicate procedure, especially when the velocity structure is not well known. We would expect more reliable solutions in a setting with larger magnitudes (say, up to M_w 4). In that case, lower frequency waves, including surface waves, could be used within full moment tensor inversions. Solutions for larger events could help determine the reliability of the solutions for smaller events, for which fewer waveforms are available.

4.2.2 Earthquakes and nuclear tests

We present full moment tensor solutions, with uncertainties, for three sets of events: 21 earthquakes in southern Alaska, 63 events at Uturuncu volcano, Bolivia, and 29 events at the Nevada Test Site. We characterize each event as a point-source moment tensor with a fixed epicenter and origin time. The source time function is a simple function that scales with magnitude. We perform a separate grid search over depth and magnitude, and our emphasis on uncertainty estimation is with the 5D space of normalized moment tensors.

Our key findings are as follows:

1. The misfit function in moment tensor space exhibits local minima and other complexities (e.g., Figure 3.7). These reveal the importance of evaluating the misfit function over the full space of moment tensors, as opposed to linearized inversions, which may lead into an incorrect local minimum.

2. The complexities of the misfit function can be distilled into a confidence curve $\mathscr{P}(V)$ that adjusts the posterior probability for the homogeneous probability of uniform moment tensors (Tape & Tape, 2016; Silwal & Tape, 2016). The area under the confidence curve is the confidence parameter $\mathscr{P}_{\text{AV}}$.

   Even in cases where moment tensor space is uniformly parameterized (e.g., Stähler & Sigloch, 2014), there is still a benefit to the confidence curve in that it can account for the 'imprinted' influence of the homogeneous probability for moment tensors.

3. We present a high-quality catalog of full moment tensors from the Nevada Test Site, building upon the efforts of Ford et al. (2009). In comparison with Ford et al. (2009), we include more stations, we use a lower minimum period (10 s) for all events, and we include (regional) body waves in all inversions. The inclusion of body waves improves the coverage of the source hemisphere, since the body-wave take-off angles tend to be steep (and downward), whereas surface-wave paths are near horizontal.

   Further efforts to include first-motion polarity measurements from short-period stations (Harmsen, 1994) could result in moment tensor solutions with higher confidence than those presented here.

Additional work is needed to improve our understanding of the theory and application of moment tensor confidence curves. The majority of choices are made within the misfit function, which includes time windowing, weighting, choice of norm, and time shifting of synthetic seismograms. For example, a more complete representation of data covariance terms (e.g., Stähler & Sigloch,

2016; Mustać & Tkalčić, 2016) could eliminate the need for a scale factor. The use of 3D synthetic seismograms could lessen the need for time shifts, if the 3D velocity model is accurate. Some questions can be adequately addressed without real data within synthetic inversions (Wéber, 2006; Walter et al., 2010; Stierle et al., 2014; Staněk et al., 2014).

Our primary goal has been to characterize uncertainties of moment tensors. This provides a starting point for interpreting the results in the context of physical models, such as those discussed in Tape & Tape (2013) or Patton & Taylor (2011). We can interpret any full moment tensor as a one-process model of an oblique opening crack (Minson & Dreger, 2008) or as a two-process model of a tensional or compressional crack combined with shear slip within the same crack plane (Aki & Richards, 2002). More complex source processes have been proposed, but they cannot be distinguished or evaluated using the typical set of seismic waveforms.

4.3 References

Aki, K. & Richards, P. G., 2002. *Quantitative Seismology*, University Science Books, San Francisco, Calif., USA, 2nd edn., 2009 corrected printing.

Ford, S. R., Dreger, D. S., & Walter, W. R., 2009. Identifying isotropic events using a regional moment tensor inversion, *J. Geophys. Res.*, **114**, B01306, doi:10.1029/2008JB005743.

Harmsen, S. C., 1994. The Little Skull Mountain, Nevada, earthquake of 29 June 1992: Aftershock focal mechanisms and tectonic stress field implications, *Bull. Seis. Soc. Am.*, **84**(5), 1484–1505.

Minson, S. E. & Dreger, D. S., 2008. Stable inversions for complete moment tensors, *Geophys. J. Int.*, **174**, 585–592, doi:10.1111/j.1365-246X.2008.03797.x.

Mustać, M. & Tkalčić, H., 2016. Point source moment tensor inversion through a Bayesian hierarchical model, *Geophys. J. Int.*, **204**, 311–323, doi:10.1093/gji/ggv458.

Patton, H. J. & Taylor, S. R., 2011. The apparent explosion moment: Inferences of volumetric moment due to source medium damage by underground nuclear explosions, *J. Geophys. Res.*, **116**, B03310, doi:10.1029/2010JB007937.

Silwal, V. & Tape, C., 2016. Seismic moment tensors and estimated uncertainties in southern Alaska, *J. Geophys. Res. Solid Earth*, **121**, 2772–2797, doi:10.1002/2015JB012588.

Stähler, S. C. & Sigloch, K., 2014. Fully probabilistic seismic source inversion – Part 1: Efficient parameterisation, *Solid Earth*, **5**, 1055–1069, doi:10.5194/se-5-1055-2014.

Stähler, S. C. & Sigloch, K., 2016. Fully probabilistic seismic source inversion – Part 2: Modelling errors and station covariances, *Solid Earth*, **7**, 1521–1536, doi:10.5194/se-2016-87.

Staněk, F., Eisner, L., & Moser, T. J., 2014. Stability of source mechanisms inverted from P-wave amplitude microseismic monitoring data acquired at the surface, *Geophys. Prosp.*, **62**, 475–490, doi: 10.1111/1365-2478.12107.

Stierle, E., Vavryčuk, V., Šílenỳ, J., & Bohnhoff, M., 2014. Resolution of non-double-couple components in the seismic moment tensor using regional networks—I: a synthetic case study, *Geophys. J. Int.*, **196**, 1869–1877, doi:10.1093/gji/ggt502.

Tape, W. & Tape, C., 2013. The classical model for moment tensors, *Geophys. J. Int.*, **195**, 1701–1720, doi:10.1093/gji/ggt302.

Tape, W. & Tape, C., 2016. A confidence parameter for seismic moment tensors, *Geophys. J. Int.*, **205**, 938–953, doi:10.1093/gji/ggw057.

Walter, F., Dreger, D. S., Clinton, J. F., Deichmann, N., & Funk, M., 2010. Evidence for near-horizontal tensile faulting at the base of Gornergletscher, a Swiss Alpine Glacier, *Bull. Seis. Soc. Am.*, **100**(2), 458–472, doi:10.1785/0120090083.

Wéber, Z., 2006. Probabilistic local waveform inversion for moment tensor and hypocentral location, *Geophys. J. Int.*, **165**, 607–621.

Appendix A
Supplemental Materials

Supplemental Materials published with the article

Full moment tensors for small events ($M_W < 3$) at Uturuncu volcano, Bolivia

Celso Alvizuri and Carl Tape

Geophysical Journal International

A.1 ScholarWorks@UA collection

Our moment tensor catalog of 63 events is available in the text file in Table 2.4. We provide the complete results of our analysis in Alvizuri (2015). This includes two sets of figures: one for the catalog when using first-motion polarities, the other for the catalog when not using first-motion polarities.

A.1.1 Supplement overview

Results in this supplement include:

- Figure A.2: P travel time vs hypocentral distance for 63 events.
- Figure A.3: influence of polarities and structural model (homogeneous or 1D) on moment tensor solutions.
- Figures A.4–A.7: P-wave amplitude ratios and the influence of weights within the inversion.
- Figures A.8–A.20: inversion results for the example event using different subsets of waveforms.
- Figures A.21–A.24 show inversion results and their misfit for the example event but for inversions limited to specific physical models.

A.2 Classification based on wavenumbers and assumed heterogeneity

Aki & Richards (1980, Figure 13.11) offered a classification plot for examining the role of scattering in seismic wave propagation. On the y-axis of the plot is ka, the product of wavenumber k and length scale of heterogeneity a. On the x-axis of the plot is kL, the product of wavenumber k and propagation distance L. We can directly calculate kL using frequency limits in our study: 0.25–0.50 Hz for surface waves and 2–10 Hz for body waves. Most events are at depths of 10 km

below the surface, so we consider propagation distances of 10 km and 50 km. The values of kL are tabulated in Table A.1.

Figure A.1 reproduces the plot of Aki & Richards (1980, Figure 13.11). As they point out, "ka in seismology can take almost any value. However, scattering effects can be neglected for very large or very small ka." Studies of scattering within the crust of Japan estimated a correlation length of $a = 5$ km (Takemura et al., 2015). Individual volcanoes can be notoriously complex in structure (e.g., Tarantola, 2006), and we might expect them to have smaller length scales of heterogeneity. In Figure A.1, we choose four values of a from 10 m to 10 km and show where our values lie. Factors that would favor our assumption of a homogeneous velocity model (i.e., "equivalent homogeneous body") are: (1) finer heterogeneity (smaller a), (2) lower frequencies (smaller f), (3) shorter propagation distances (lower L), and (4) weaker strength of heterogeneity ($< \mu^2 >$ in Aki & Richards (1980)). Based on our kL-ka analysis, we must be cautious about scattering, as some of our possibilities fall outside the regime of validity for the assumption of a homogeneous velocity model.

Table A.1: kL values for relevant frequencies, velocities, and source-station distances in our study. kL is the dimensionless product of the wavenumber and the distance. The bandpass limits are 0.25–0.50 Hz for the surface waves and 2–10 Hz for the P waves. The number in parentheses is the wavelength. See also Figure A.1.

	L = 10 km				L = 50 km			
frequency	V_S = 2.82 km/s		V_P = 4.80 km/s		V_S = 2.82 km/s		V_P = 4.80 km/s	
0.25 Hz	6	(11.3 km)	3	(19.2 km)	33	(11.3 km)	20	(19.2 km)
0.50 Hz	11	(5.6 km)	7	(9.6 km)	67	(5.6 km)	39	(9.6 km)
2.0 Hz	45	(1.4)	26	(2.4 km)	267	(1.4 km)	157	(2.4 km)
10.0 Hz	223	(0.3 km)	131	(0.5 km)	1337	(0.3 km)	785	(0.5 km)

A.3 Influence of velocity structure on moment tensor inversions

Figure A.3 shows the influence of structure model and of first motion polarities on the inversion of moment tensors. Figure A.3a compares inversions with and without first motions, both using the 1D model. This result shows that moment tensor difference (θ) for a given event can vary by up to $\theta = 60^\circ$ when using the 1D model. In comparison, Figure 2.9 shows that the majority of solutions show variations of $\theta < 5^\circ$ when using the halfspace model.

Solutions obtained using either the halfspace or 1D model also show large differences. This means that solutions for these small events are sensitive to structure model. Figure A.3b compares

inversions with the halfspace and the 1D models, both inversions using first motion polarities. This result shows that moment tensors obtained using the halfspace and 1D models can vary by over $\theta = 40^{\circ}$ for a given event, and that scatter in waveform fit (ΔVR) does not favor either model.

We compare vertical and radial amplitudes for P-wave first arrivals. This allows us to compare observed P-wave amplitudes against those predicted from the structure model. Figure A.4 compares maximum P-wave amplitudes between the vertical and radial components, for both observed and synthetic seismograms. This figure combines measurements from all 63 events in this study. Synthetic seismograms are obtained from the inversions with the halfspace model and weights V01 R01 S01. The observed histograms are skewed toward positive values, which shows vertical amplitudes are larger than radial amplitudes. The synthetic seismograms are skewed toward negative values, which shows vertical amplitudes are smaller than radial amplitudes. The scatter plot summarizes these results.

Figure A.5 shows amplitude ratios between maximum observed and synthetic P-wave amplitudes at each station. Synthetic amplitudes are now obtained from the inversions with the halfspace model and weights V01 R01 S01. Amplitude ratios for the vertical components are skewed toward positive, and amplitude ratios for the radial components are near zero.

Figure A.6 is same as Figure A.5, but for the weights used in our final catalog (V10 R01 S10). As expected, amplitude ratios for the vertical components are now near zero, while amplitude ratios for the radial components are skewed toward negative.

Figure A.7 shows mean P-wave amplitude ratios at each station and interpolated between stations. Figures A.7a-b show large amplitude differences for the vertical component when using weights V01 R01 S01. Figures A.7c-d show better amplitude match for the vertical component when using weights V10 R01 S01.

Table A.2: [SEPARATE FILE] Text file of our moment tensor catalog of 63 events. Details can be found within the header lines, which also refer to Kanamori (1977); Silver & Jordan (1982); Tape & Tape (2012).

Table A.3: Discretized grid for full moment tensor grid search. NPTS is the number of search points for each interval. M_{KW} is the magnitude listed in the catalog of Keyson & West (2013) (Table 2.4). By using the cosine of lune colatitude β we achieve uniform spacing on the lune (see also Tape & Tape (2015)). By using the cosine of dip θ we achieve uniform orientations.

parameter		min	max	interval	NPTS
magnitude	M_{w}	$M_{\mathrm{KW}} - 0.5$	$M_{\mathrm{KW}} + 0.5$	0.1	11
lune longitude	γ	-30°	30°	5	13
sin(lune latitude)	$b = \cos\beta = \sin\delta$	-1	1	0.05	35
strike	κ	0°	360°	5	73
rake	σ	-90°	90°	5	37
cos(dip)	$h = \cos\theta$	0	1	5	18
			total number of points (magnitude fixed)		22,121,190
			total number of points (magnitude varies)		243,333,090

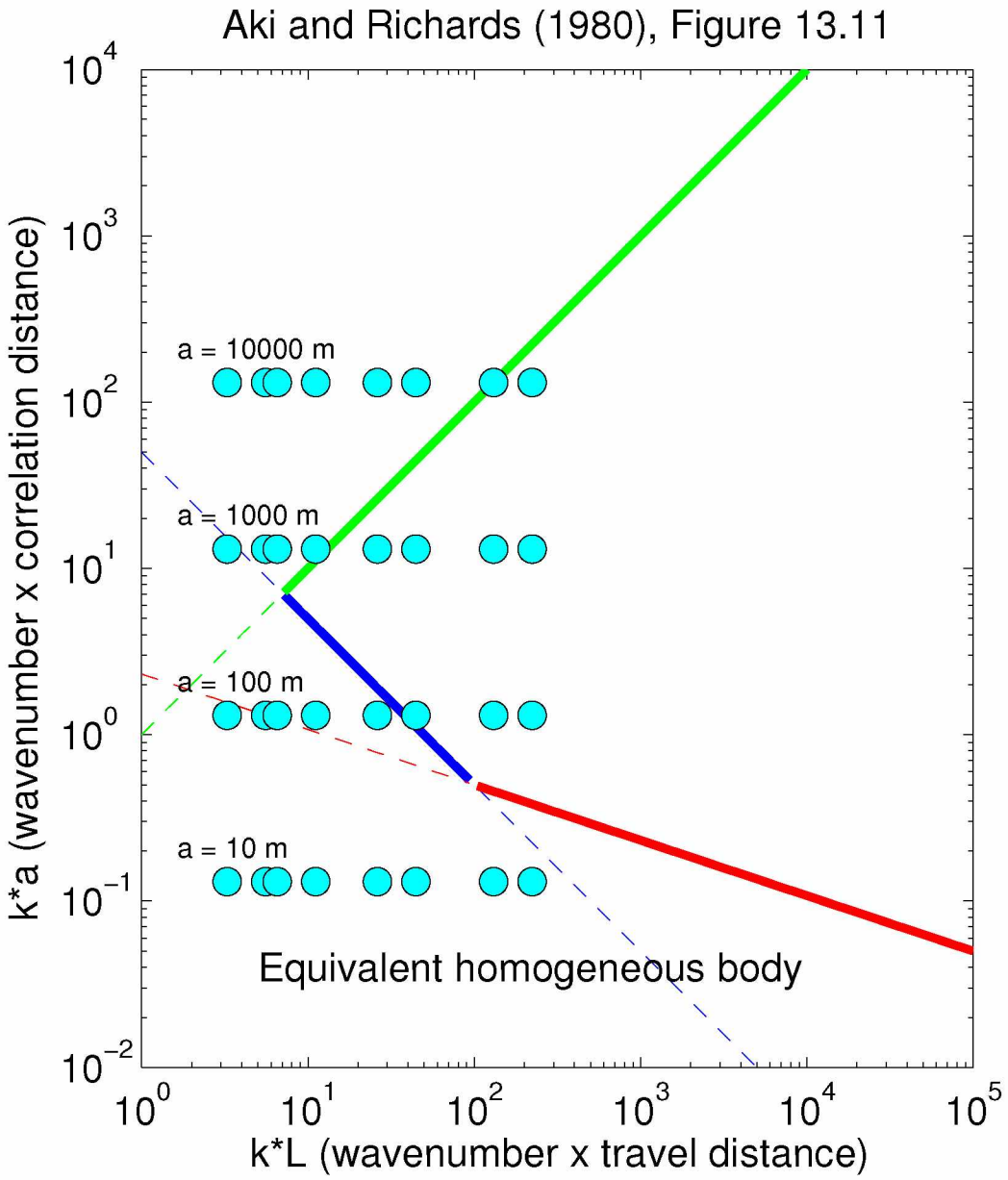

Figure A.1: *ka* versus *kL* plot after Aki & Richards (1980, Figure 13.11). The cyan dots correspond to the *kL* values for our study (Table A.1); the *ka* values are for *a* values of 10, 100, 1000, and 10000 meters.

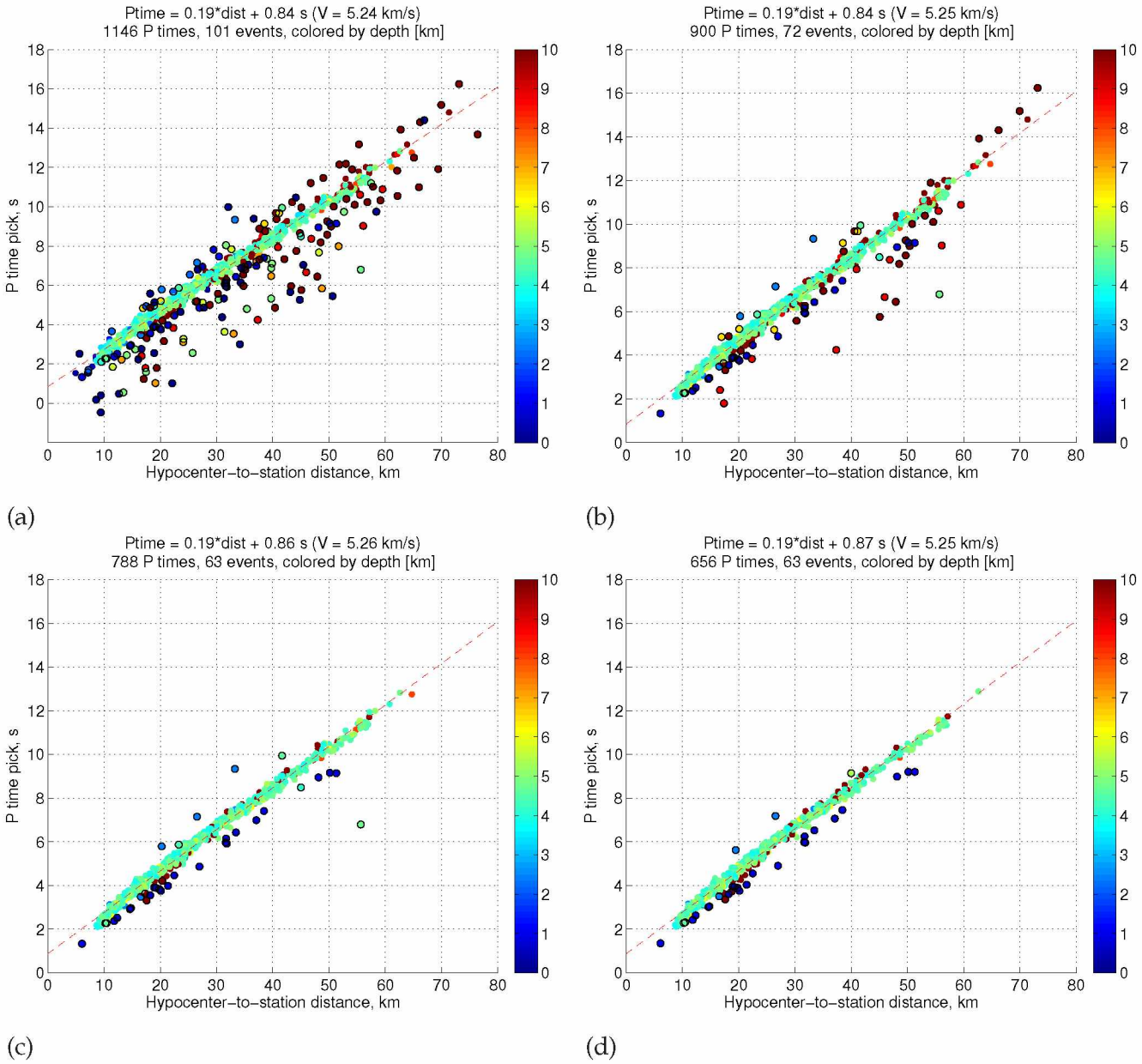

Figure A.2: Scatterplot of P travel time vs hypocentral distance for 63 events. These data are used to identify possible source parameter errors in the seismicity catalog of Keyson & West (2013) (see Section 2.3.1). (a) All 101 events $M_{KW} \geq 0$ and $\geq$20 stations OR $M_{KW} \geq 1$. There are 1146 P arrival time picks in the catalog. (b) All 72 events with $\geq$5 first-motion polarity picks. There are 900 P arrival time picks. (c) All 63 events in the catalog, after excluding 9 events that are assumed to be slab events that were mislocated to shallower depths. There are 788 P arrival time picks. (d) Same as (c), but excluding any arrival time that does not have a first-motion polarity measurement. There are 656 P arrival time picks. Most events with depths of 5 km (below sea level) are well fit by a uniform velocity (5.25 km/s).

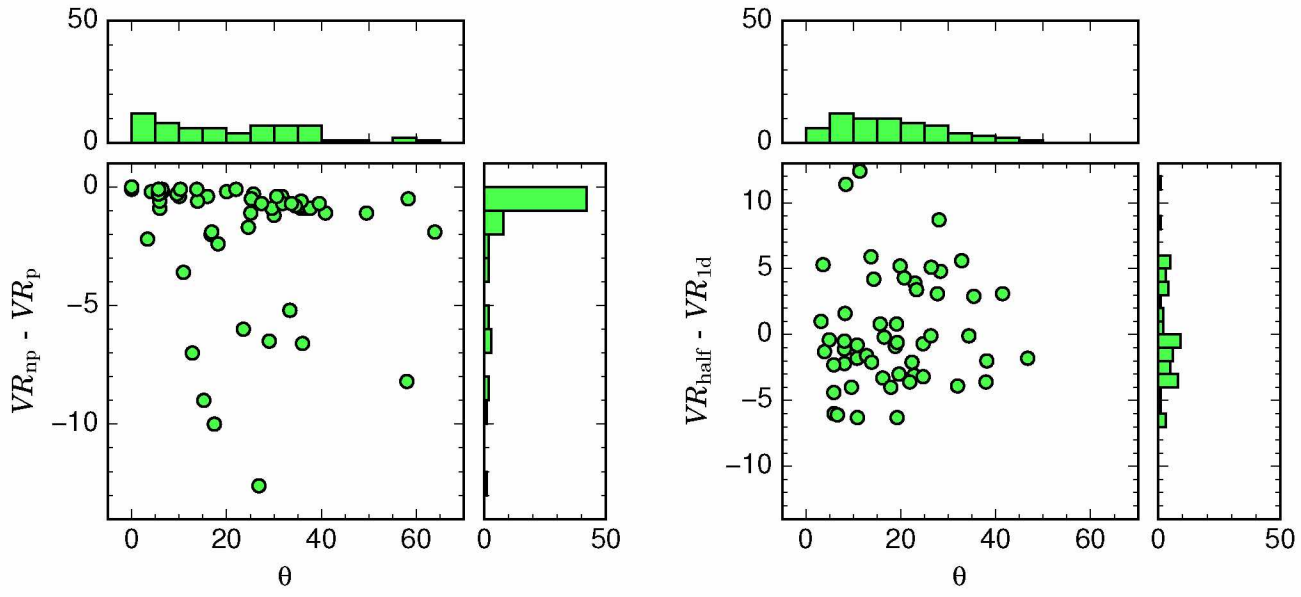

(a) (b)

Figure A.3: The influence of structural model (1D or halfspace) and first-motion polarities on moment tensor solutions. (a) Same as Figure 2.9, but for the 1D model instead of the halfspace model. Although the values of $VR_{np} - VR_p$ peak at <1%, the spread in θ is much broader than the corresponding results for the halfspace model. Moment tensor solutions for the 1D model in (a) show differences in θ of up to 60°, while in the halfspace the majority of the solutions are within 5° (Figure 2.9). (b) Differences between moment tensor solutions for the halfspace model and the 1D model, each performed using first-motion polarities. $VR_{half} - VR_{1D}$ is the difference in variance reduction; a positive value means that the halfspace model provides a better variance reduction. The spread in θ shows that solutions can vary by as much as 50°. We attribute these large difference to problems associated with the inversions using the 1D model.

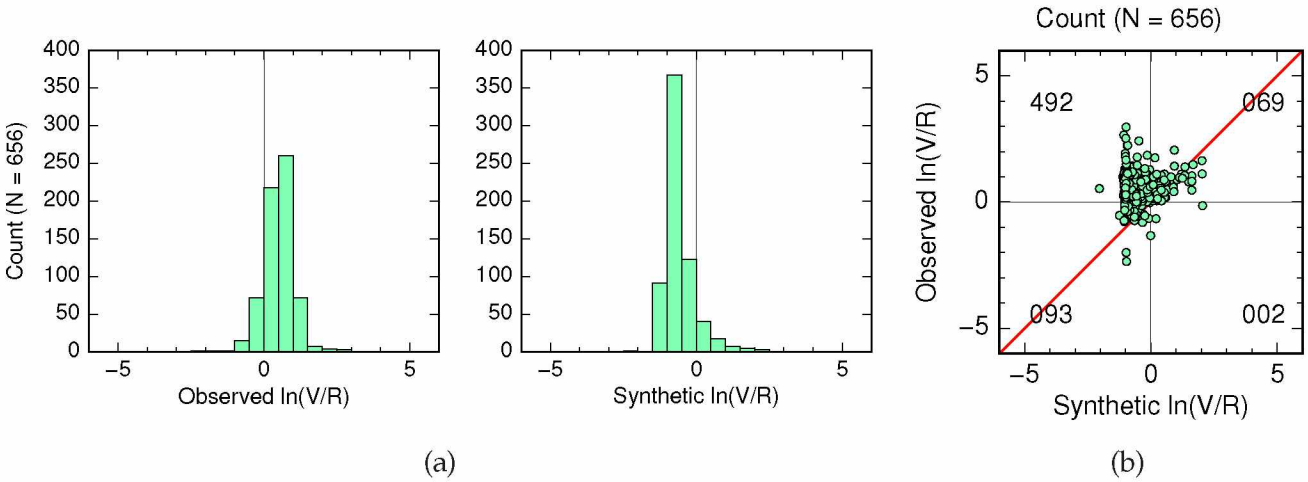

Figure A.4: Amplitude ratios between the vertical and radial components for observed and synthetic P waves. The amplitude ratio is $\ln(V/R)$, where V is the amplitude of the vertical component and R is the amplitude of the radial component. (a) Observed amplitude ratios (left) and synthetic amplitude ratios (right) based on a halfspace model. The observed histograms are skewed toward positive values, indicating that vertical observed amplitudes are larger than radial amplitudes. The synthetic seismograms are skewed toward negative values, indicating that vertical synthetic amplitudes are smaller than radial amplitudes. (b) Combination of the results plotted in the histograms. A large portion (492/656) of P wave measurements have synthetic amplitude ratios that are negative while observed amplitude ratios are positive.

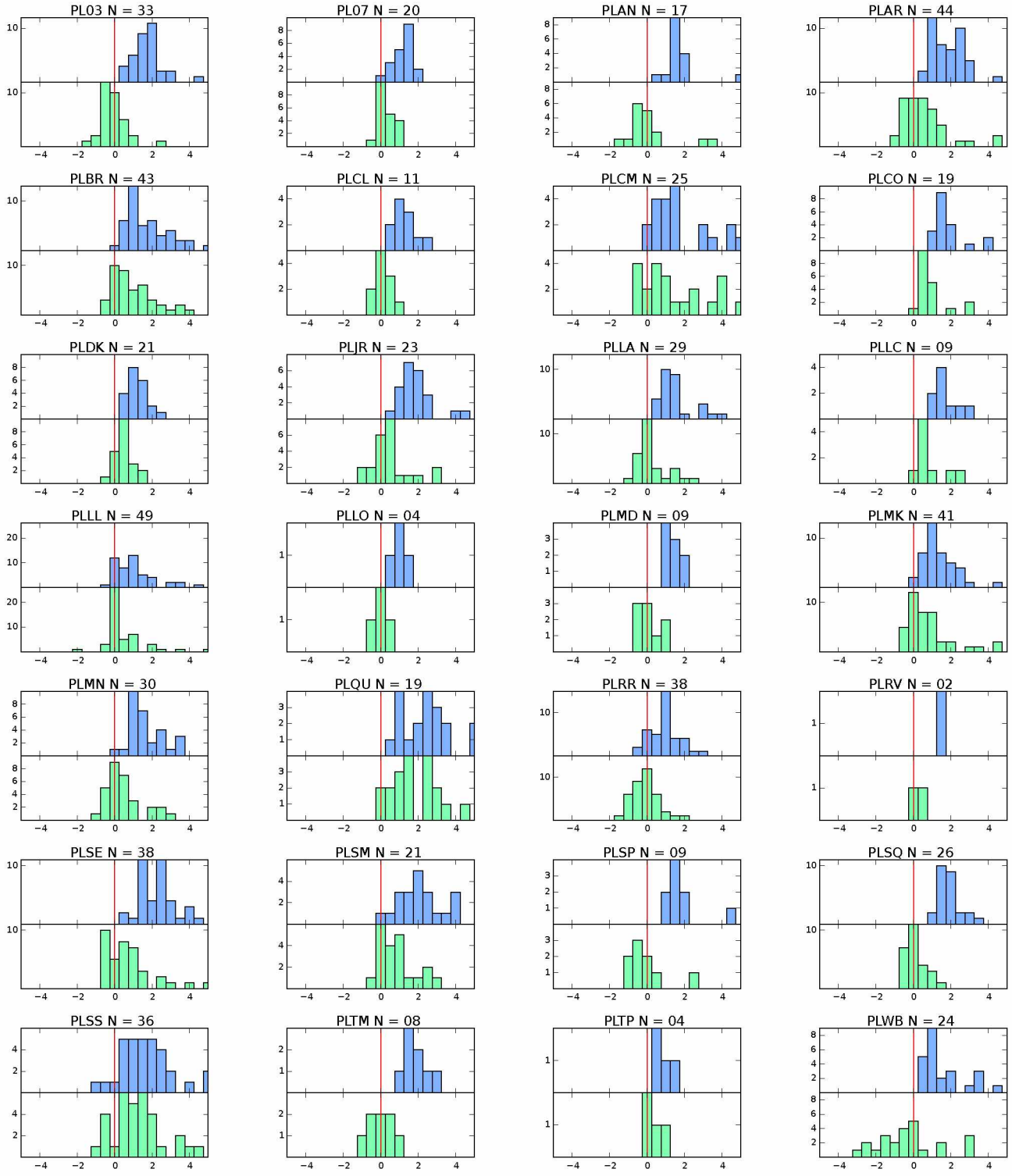

Figure A.5: P wave amplitude ratios $\ln(A_{obs}/A_{syn})$ between observed and synthetic waveforms. Amplitudes are obtained from inversion weights P01 V01 R01 for the homogeneous halfspace model. Blue histograms are for vertical amplitude ratios $\ln(V_{obs}/V_{syn})$, green are for radial amplitude ratios $\ln(R_{obs}/R_{syn})$. Note that the histograms for the vertical components are skewed toward positive values, and the histograms for the radial components peak near zero.

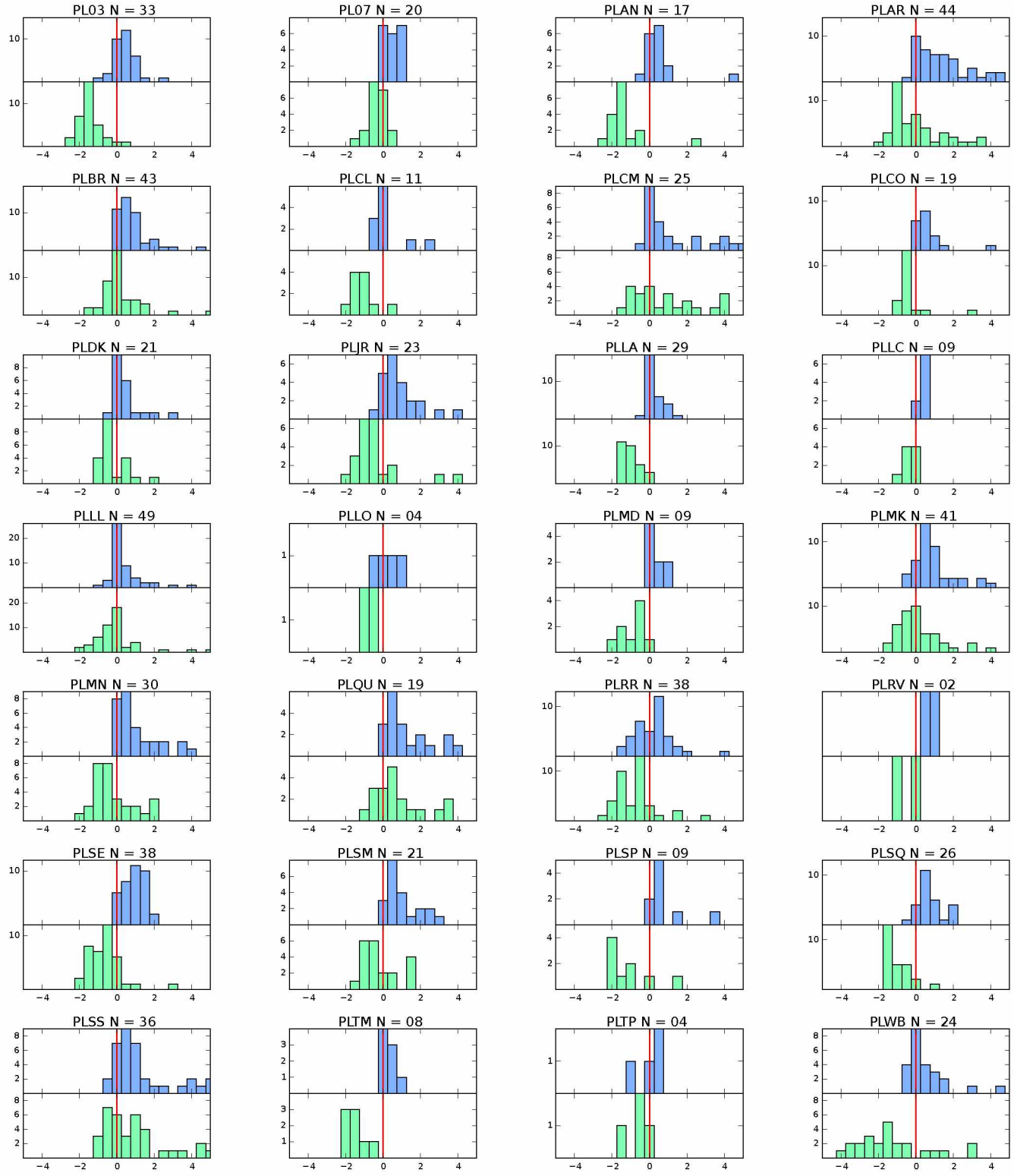

Figure A.6: Same as Figure A.5, but for the weights used in our final catalog (V10 R01 S10); here the P wave radial component is down-weighted relative to the P-wave vertical component and surface waves. The histograms for the vertical components (blue) now peak near zero, and the histograms for the radial components (green) are skewed toward negative values.

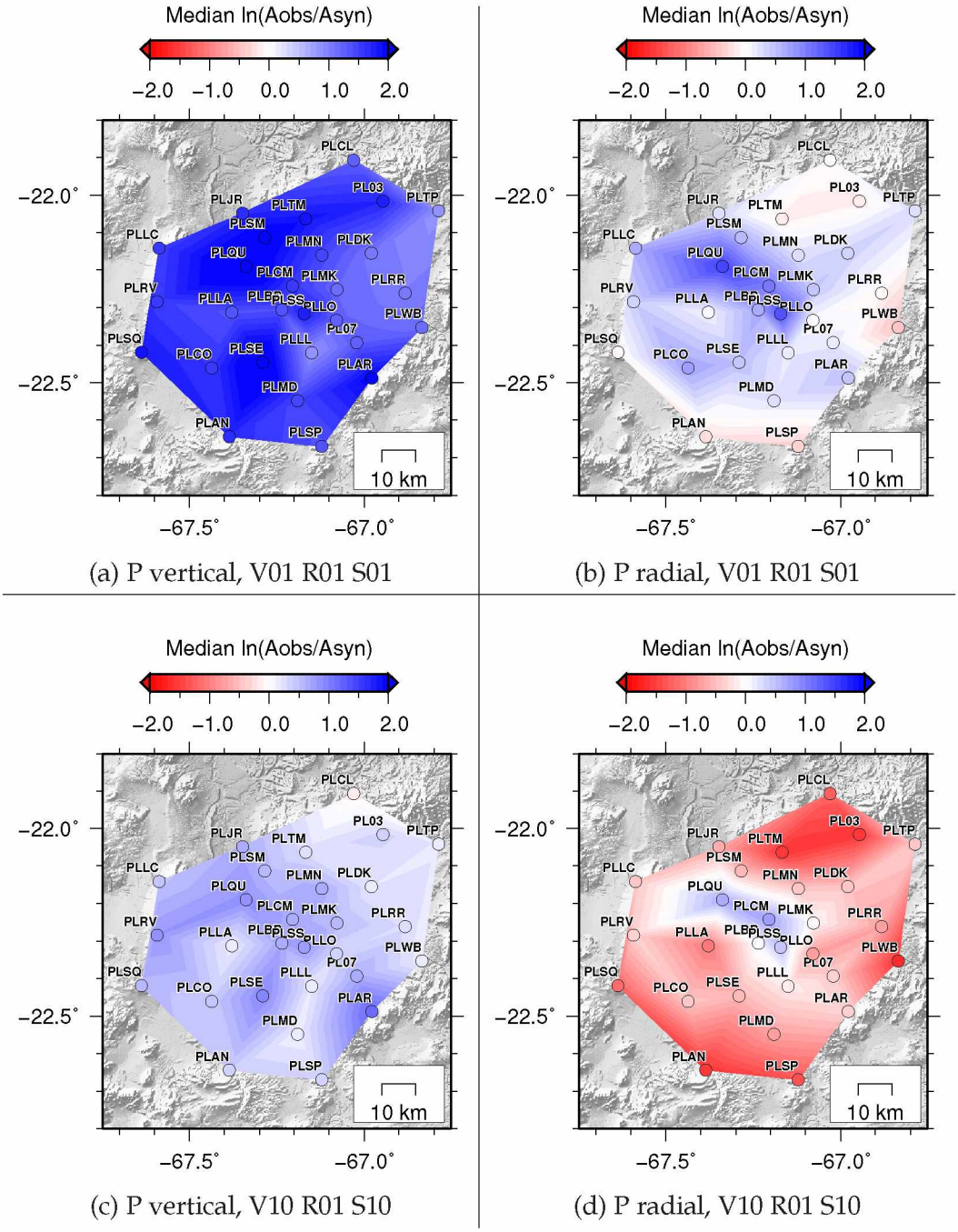

(a) P vertical, V01 R01 S01

(b) P radial, V01 R01 S01

(c) P vertical, V10 R01 S10

(d) P radial, V10 R01 S10

Figure A.7: Map of median amplitude ratios at each station from Figure A.6. We have interpolated among stations to highlight the spatial patterns. (a) Median ratios for vertical component P wave, weights V01 R01 S01. (b) Median ratios for radial component P wave, weights V01 R01 S01. (c)-(d) Same as (a)-(b) but for weights V10 R01 S10. The relative upweighting of the vertical component results in a shift from the deeper blues in (a), representing larger positive anomalies, to the lighter blues in (c). Meanwhile the radial component anomalies shift from lighter colors in (b) to red colors in (d). We also see some spatial correlation among the amplitude anomalies, suggesting that the amplitude anomalies arise from structural complexity near each station ('site effects').

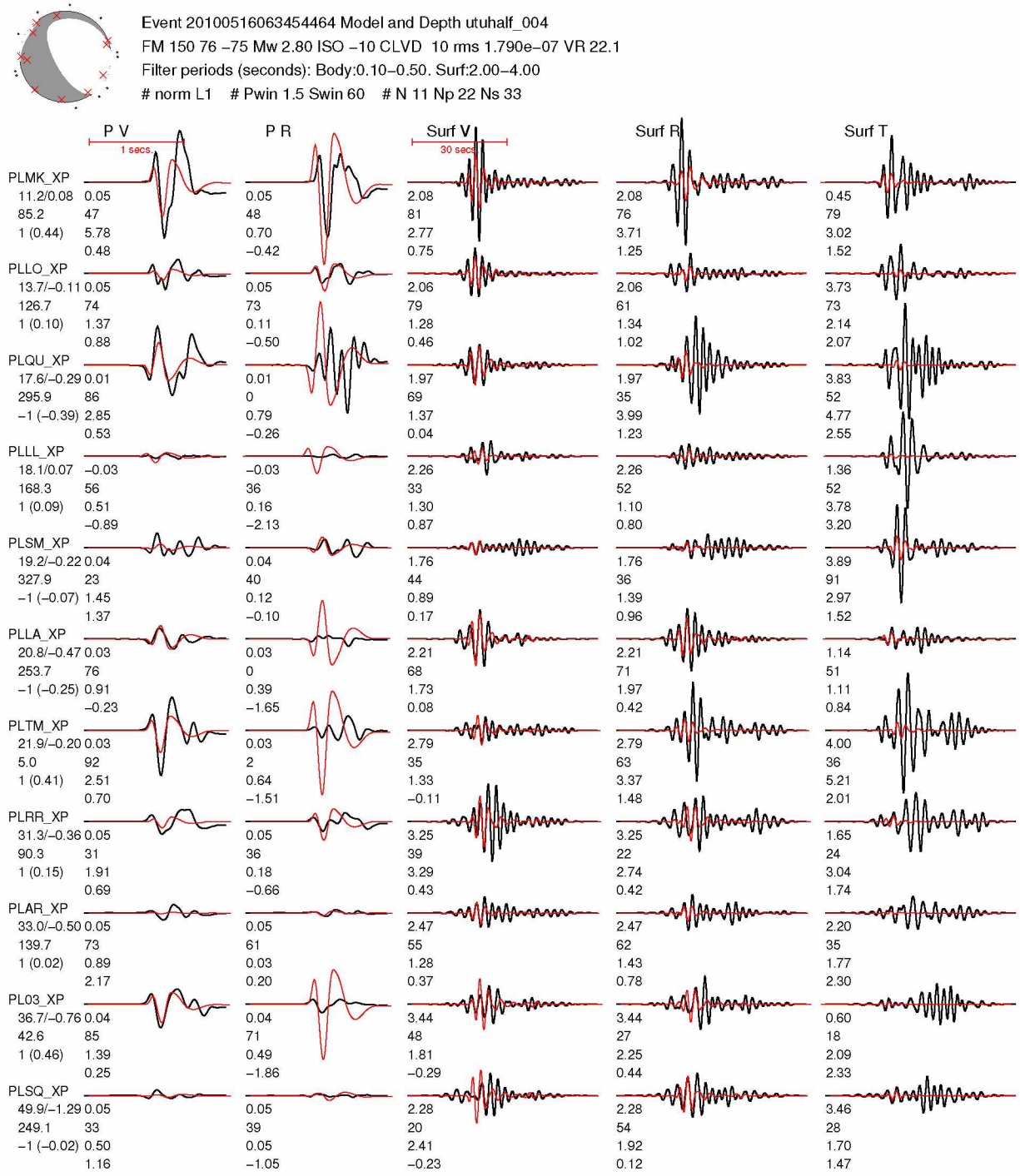

Figure A.8: Same as Figure 2.4, but here we use a different plotting scale for the waveforms. All body waves (left two columns) are scaled to the largest among all waveforms in the set. All surface waves (right three columns) are scaled to the largest among all waveforms in the set. In Figure 2.4, each segmented waveform (data or synthetic) is scaled to the same size, so that the shapes of the data and synthetic waveforms can be easily compared.

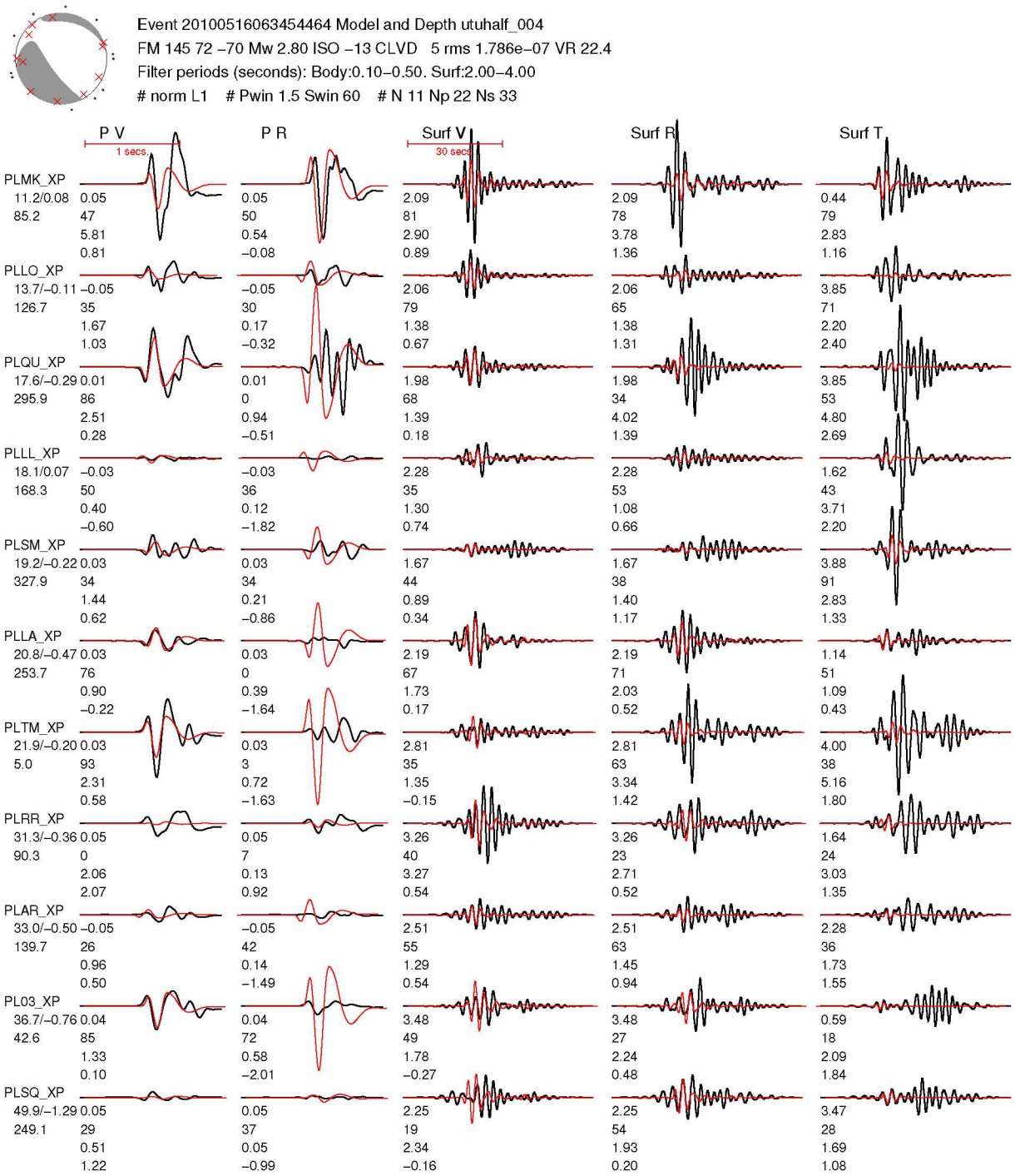

Figure A.9: Waveform fits for the example event, weights V10 R01 S10, no polarities. Misfit summary in Figure A.15. See summary in Table 2.3.

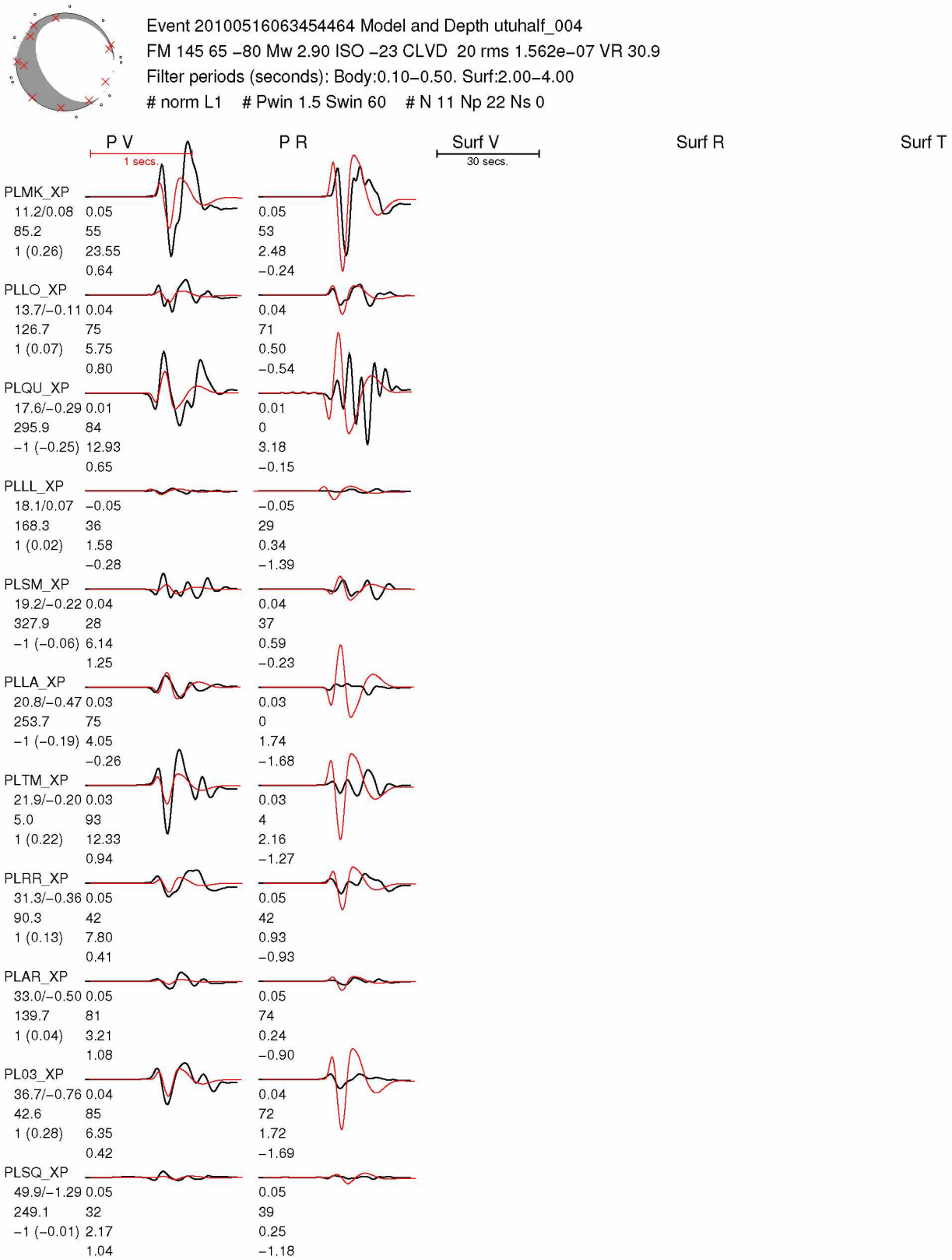

Figure A.10: Waveform fits for the example event, weights V10 R01 S00. Misfit summary in Figure A.17. See summary in Table 2.3.

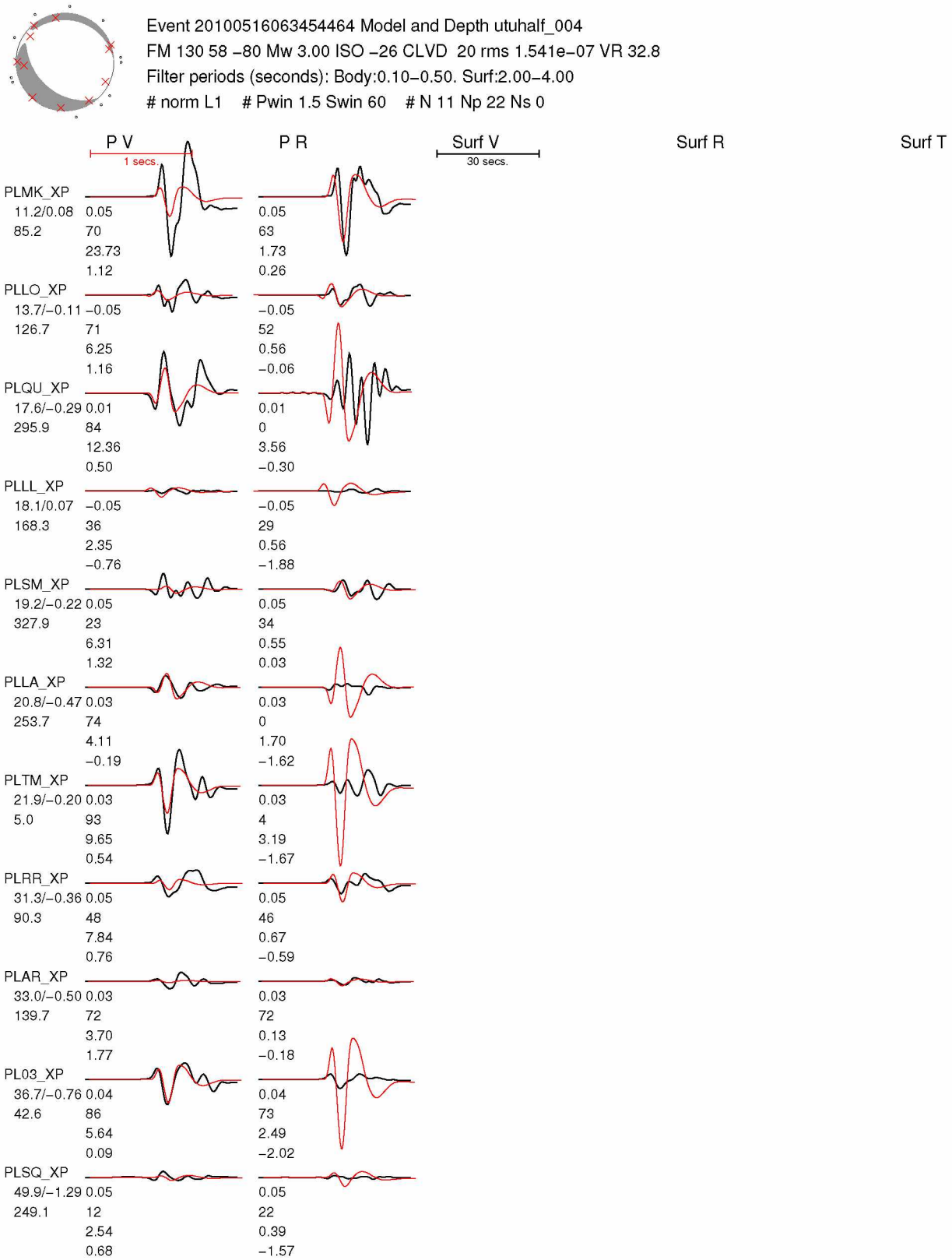

Figure A.11: Waveform fits for the example event, weights V10 R01 S00, no polarities. Misfit summary in Figure A.16. See summary in Table 2.3.

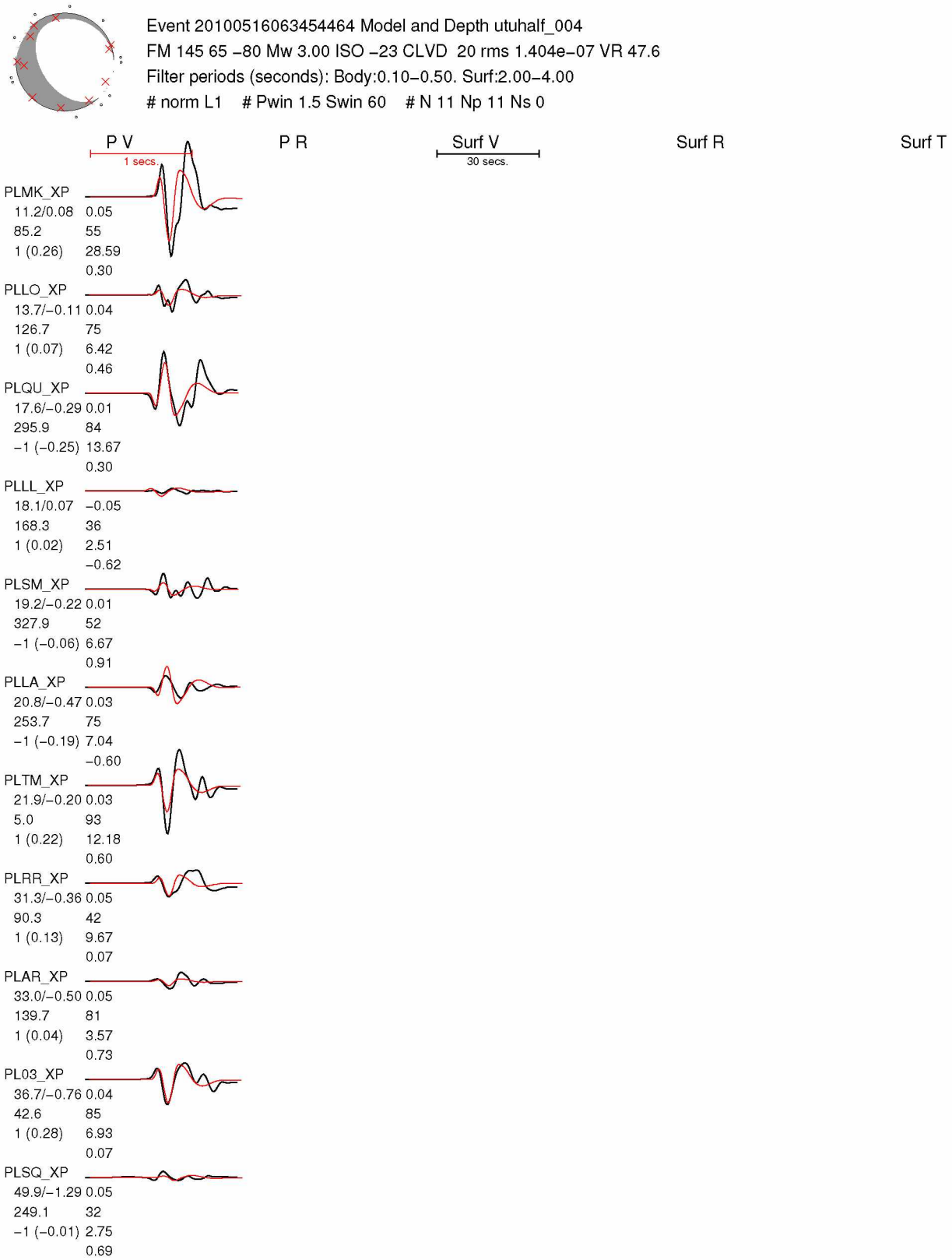

Figure A.12: Waveform fits for the example event, weights V10 R00 S00. Misfit summaries in Figures 2.8a and A.18. See summary in Table 2.3.

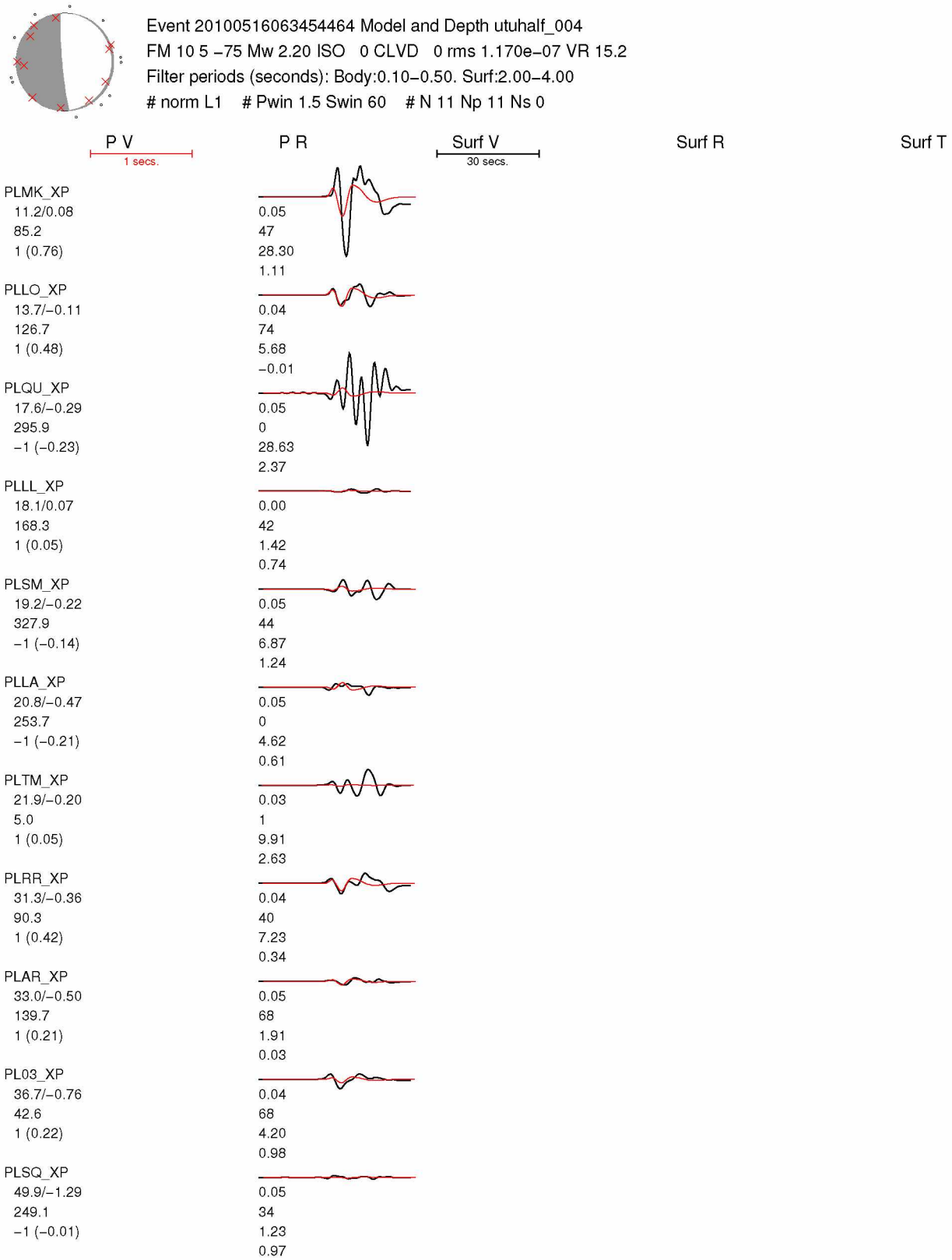

Figure A.13: Waveform fits for the example event, weights V00 R01 S00. Misfit summaries in Figure 2.8b and Figure A.19. See summary in Table 2.3.

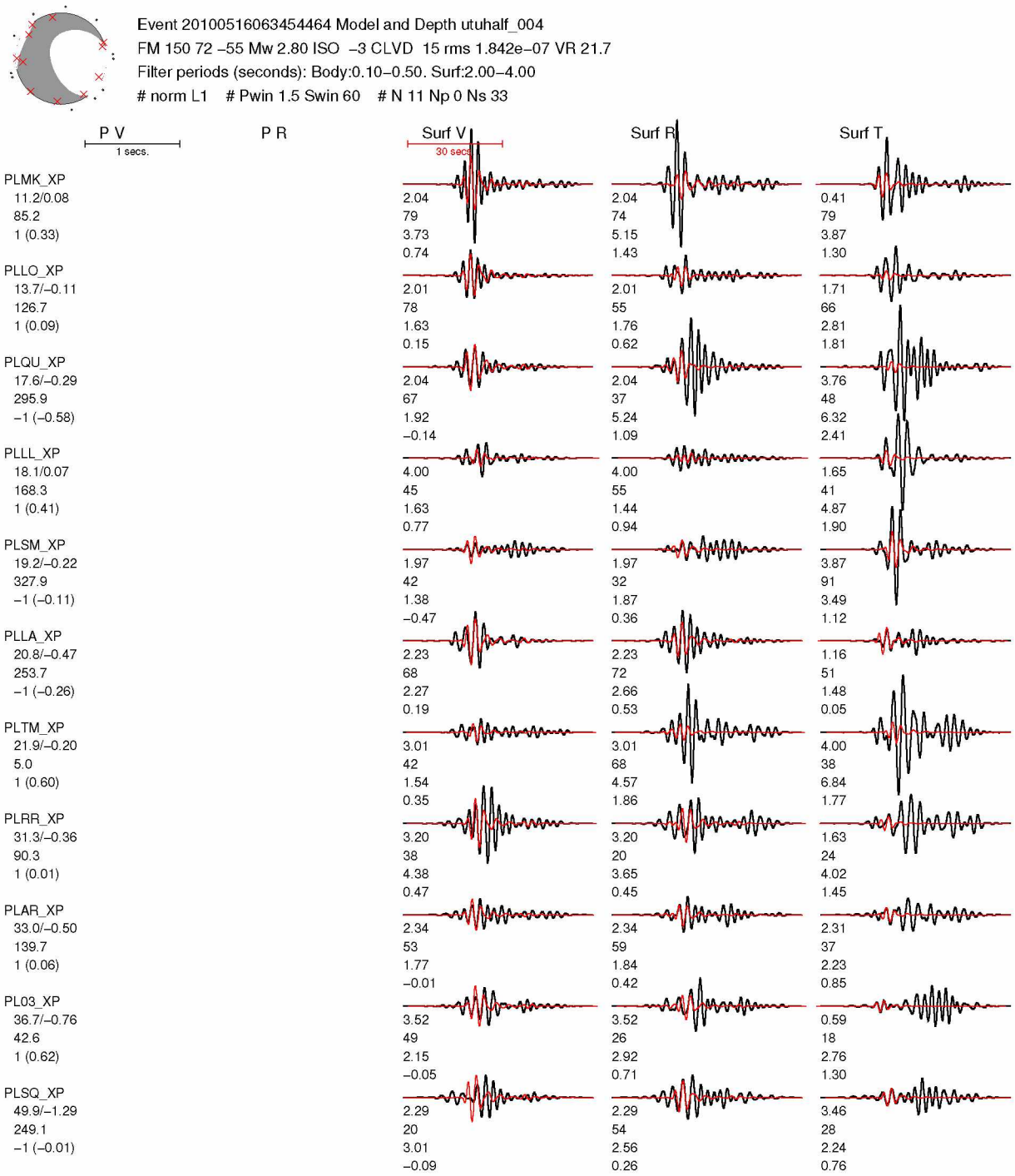

Figure A.14: Waveform fits for the example event, weights V00 R00 S10. Misfit summaries in Figure 2.8c and Figure A.20. See summary in Table 2.3.

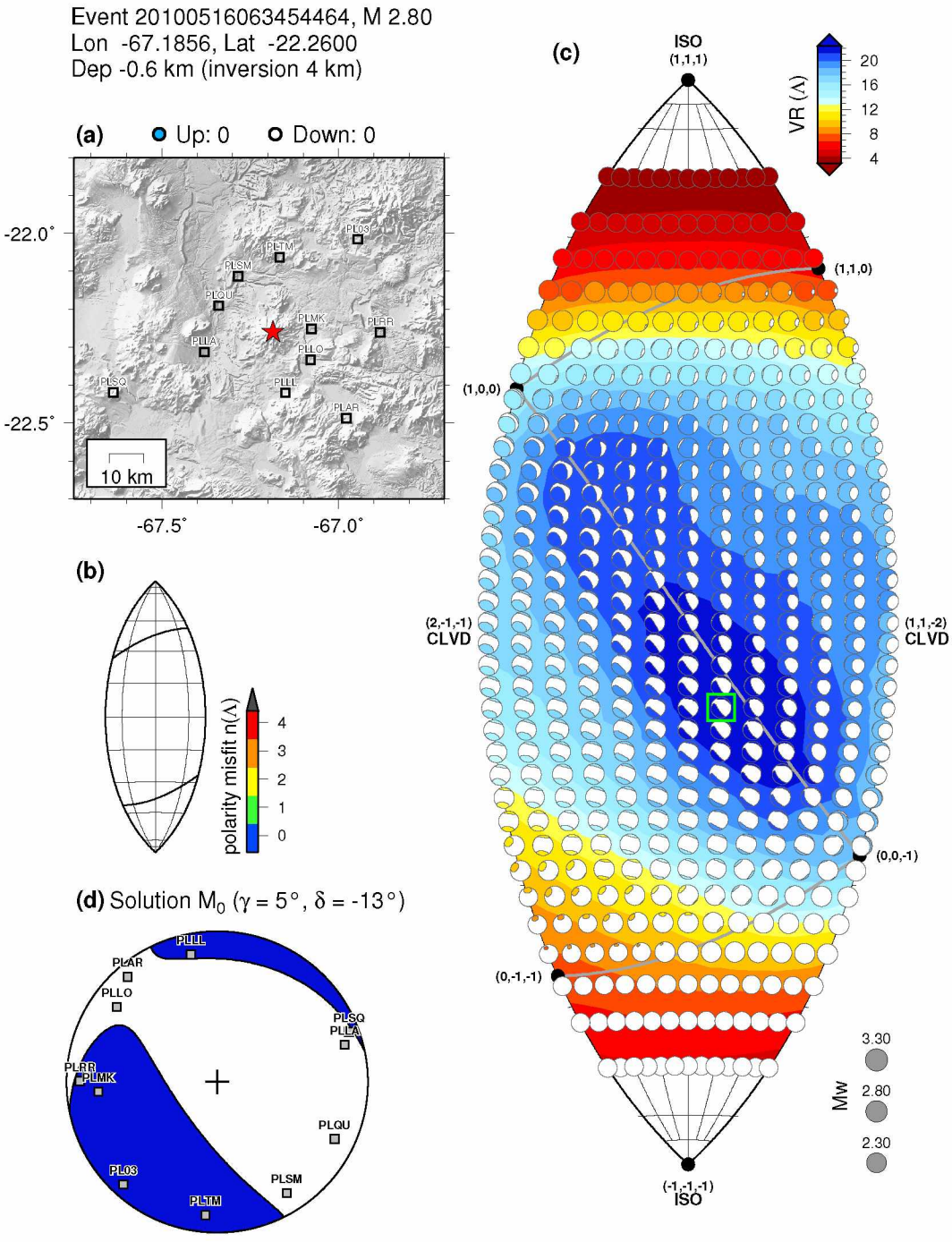

Figure A.15: Misfit summary for the example event, weights V10 R01 S10, no polarities. See caption of Figure 2.6 for details. Waveform fits in Figure A.9. See summary in Table 2.3.

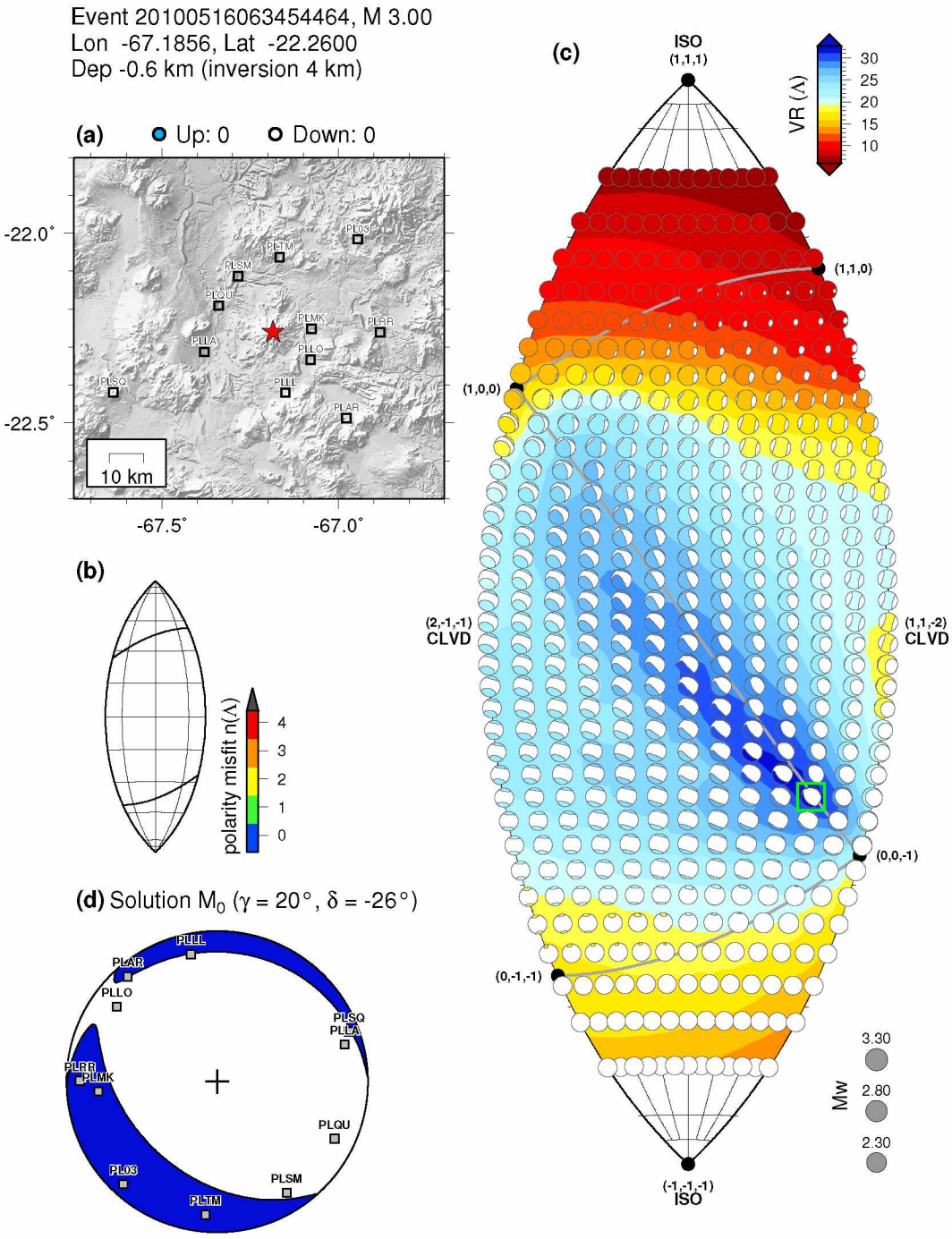

Figure A.16: Misfit summary for the example event, weights V10 R01 S00, no polarities. See caption of Figure 2.6 for details. Waveform fits in Figure A.11. See summary in Table 2.3.

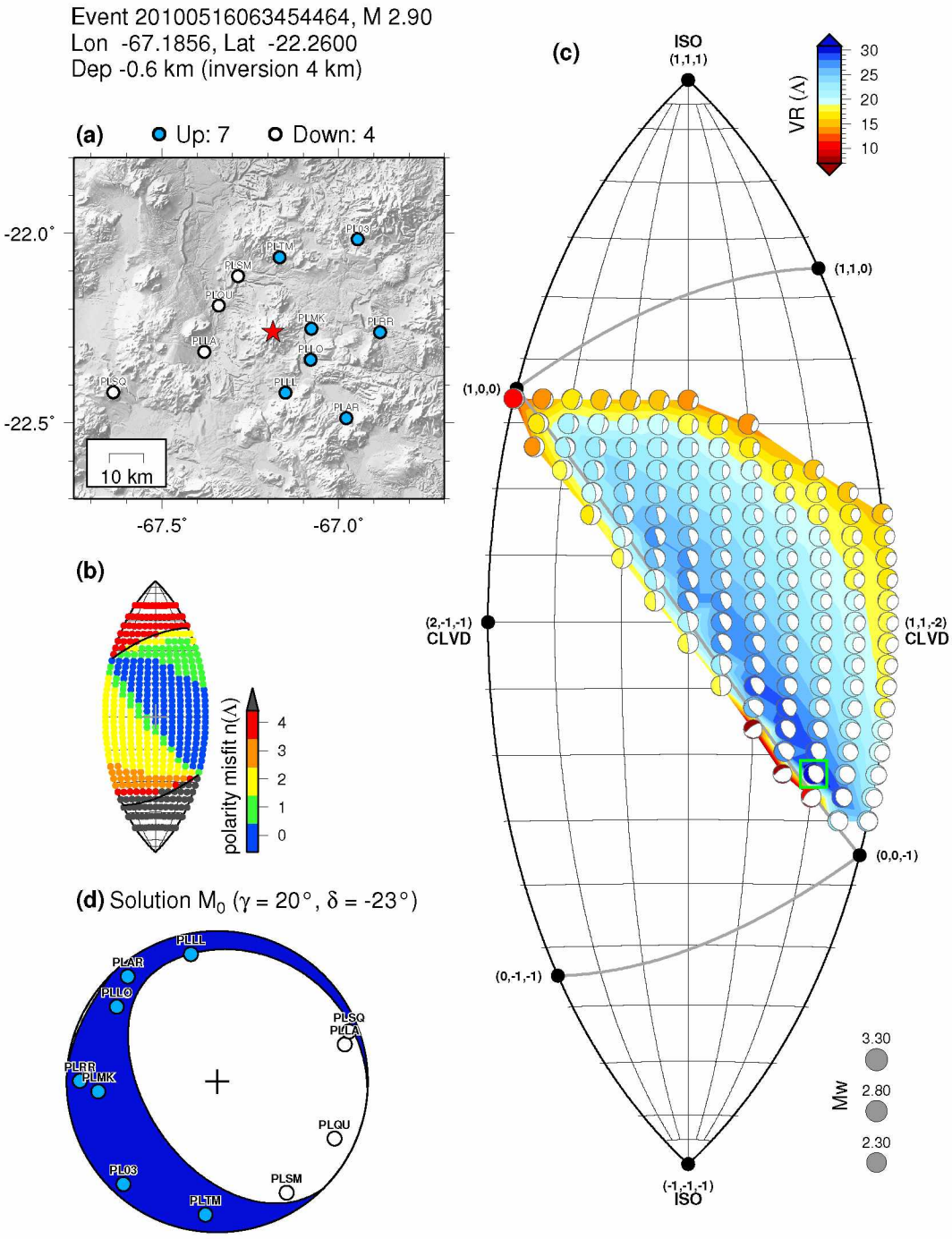

Figure A.17: Misfit summary for the example event, weights V10 R01 S00. See caption of Figure 2.6 for details. Waveform fits in Figure A.10. See summary in Table 2.3.

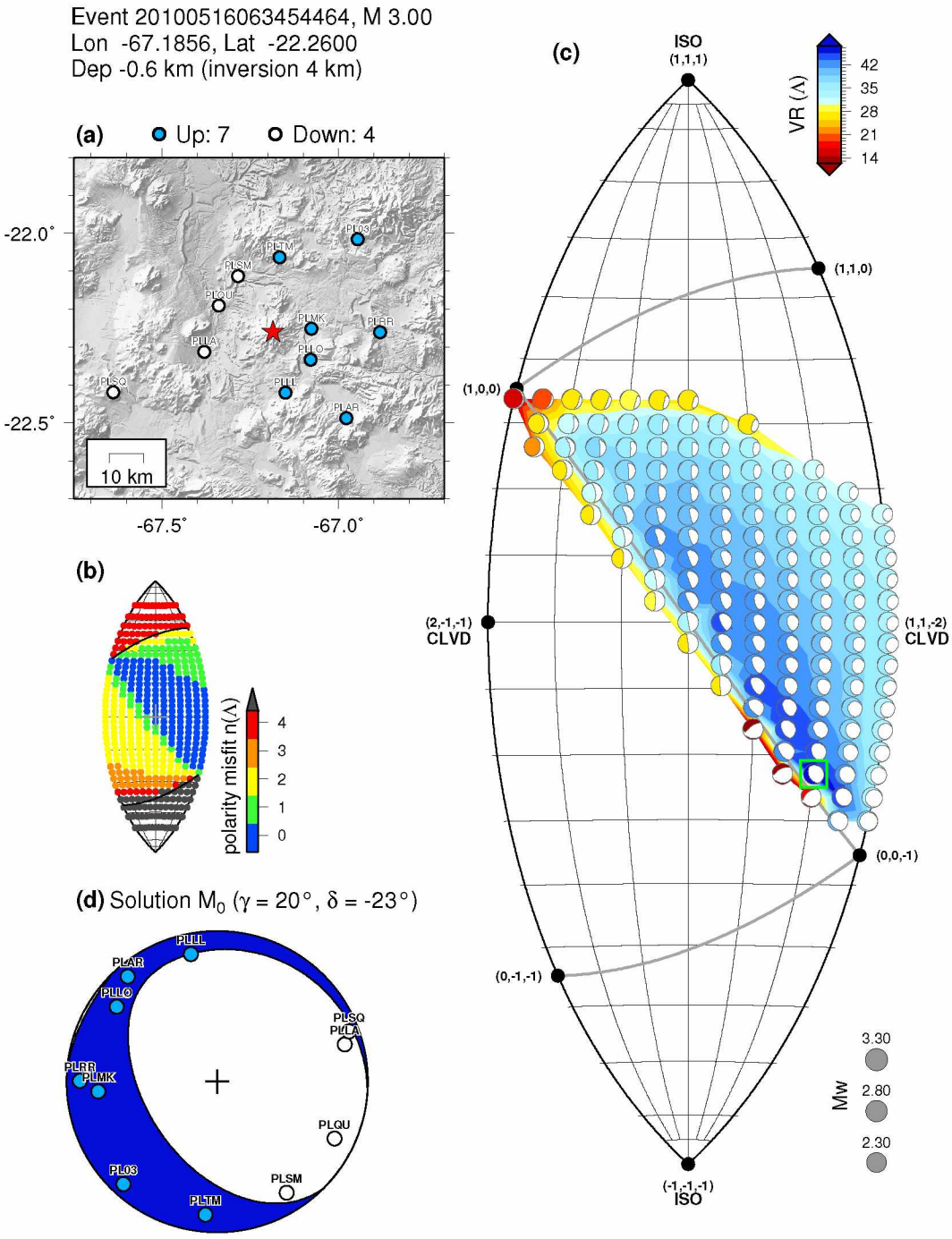

Figure A.18: Misfit summary for the example event, weights V10 R00 S00. Waveform fits in Figure A.12. See summary in Table 2.3.

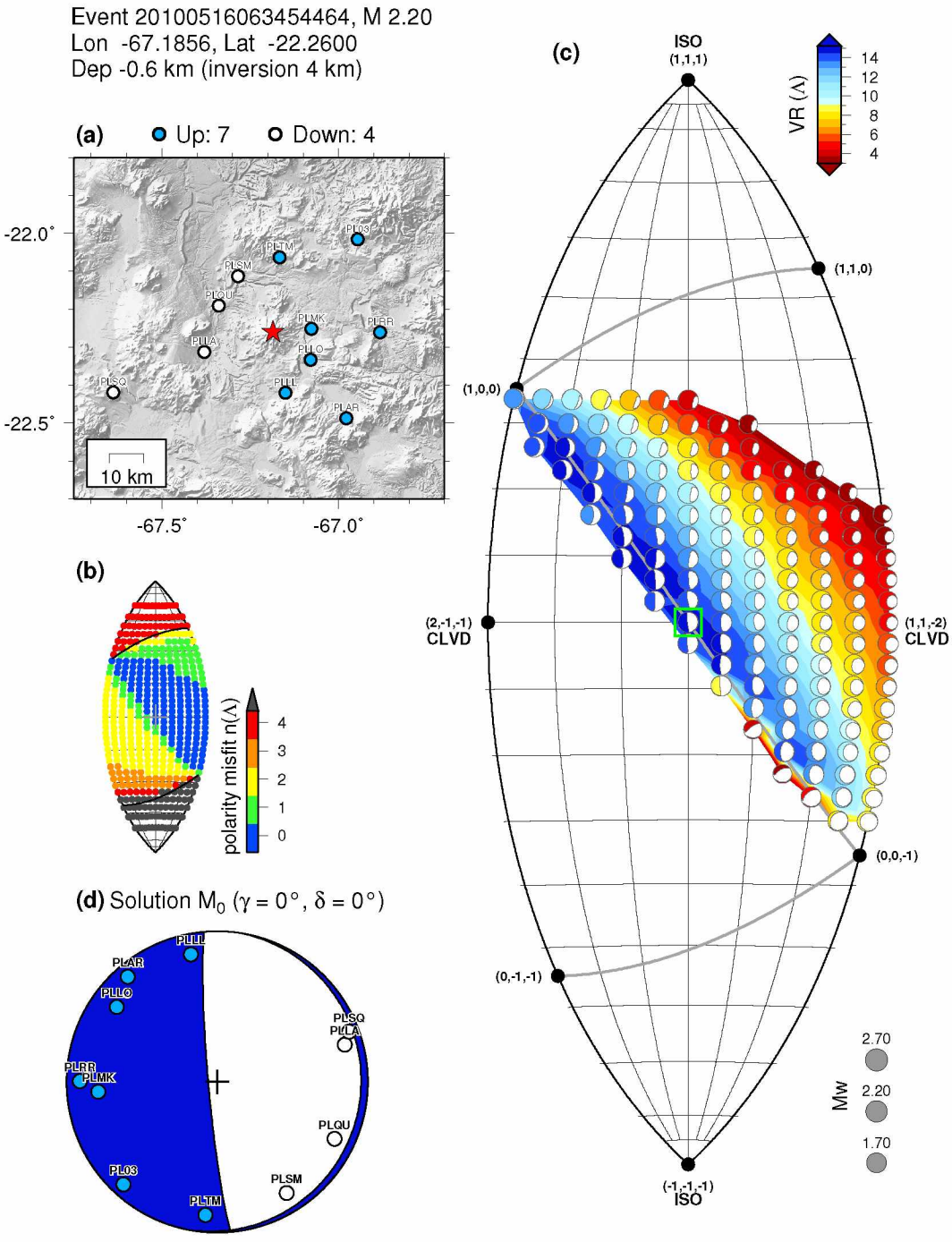

Figure A.19: Misfit summary for the example event, weights V00 R01 S00. See caption of Figure 2.6 for details. Waveform fits in Figure A.13. See summary in Table 2.3.

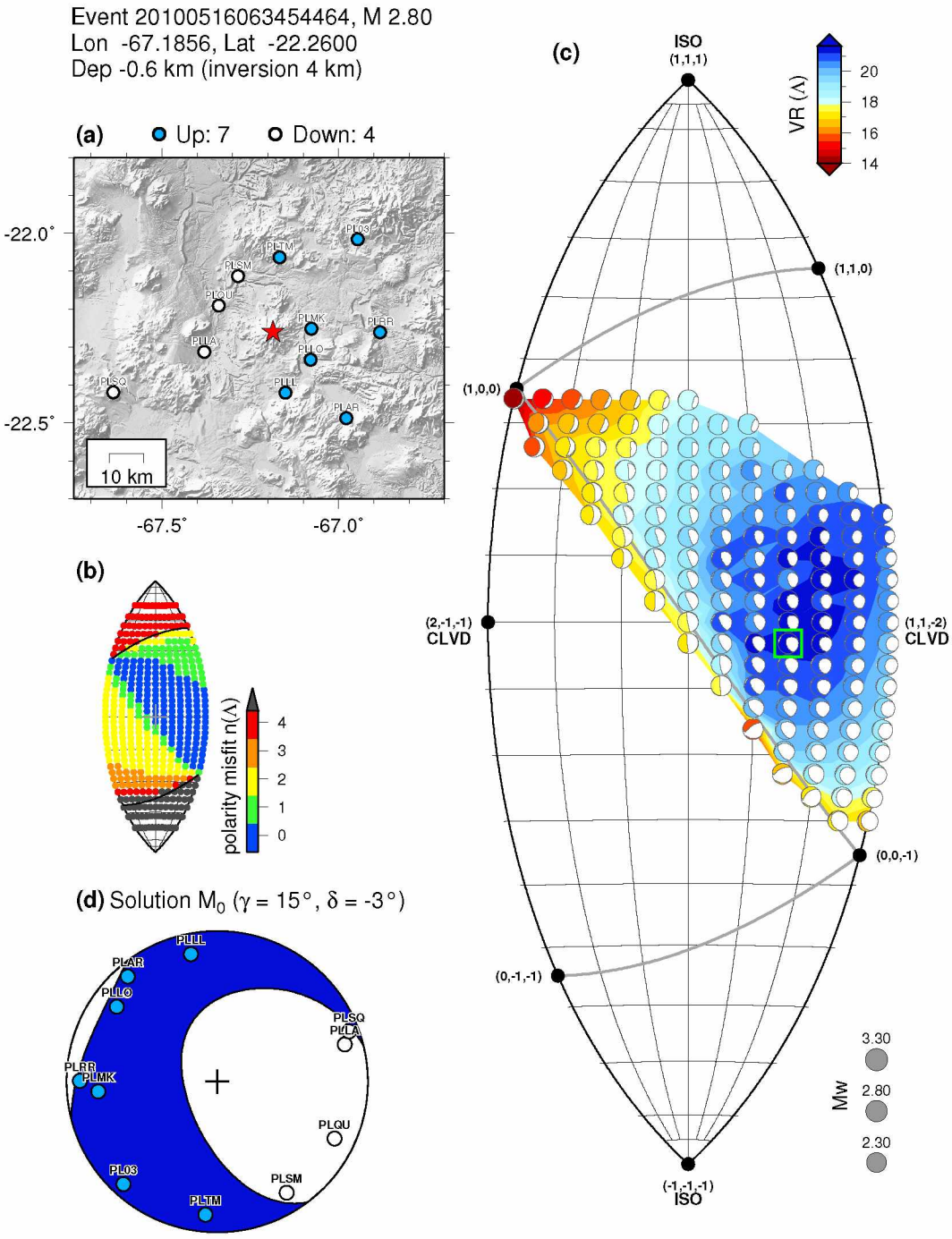

Figure A.20: Misfit summary for the example event, weights V00 R00 S10. See caption of Figure 2.6 for details. Waveform fits in Figure A.14. See summary in Table 2.3.

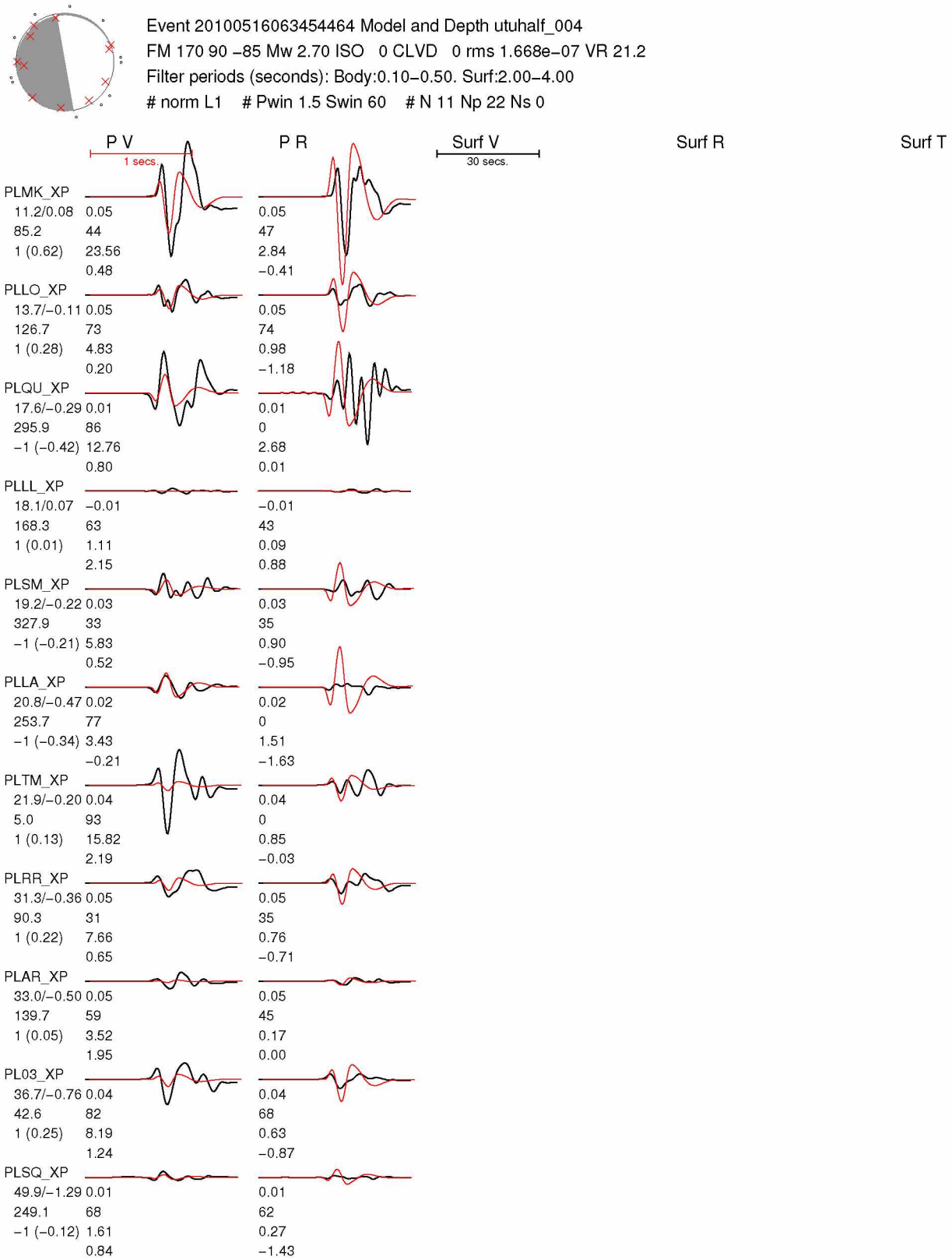

Figure A.21: Waveform fits for the example event, weights V10 R01 S00, double couple ($\gamma = 0°$, $\delta = 0°$). Misfit summary in Figure A.24b. See summary in Table 2.3.

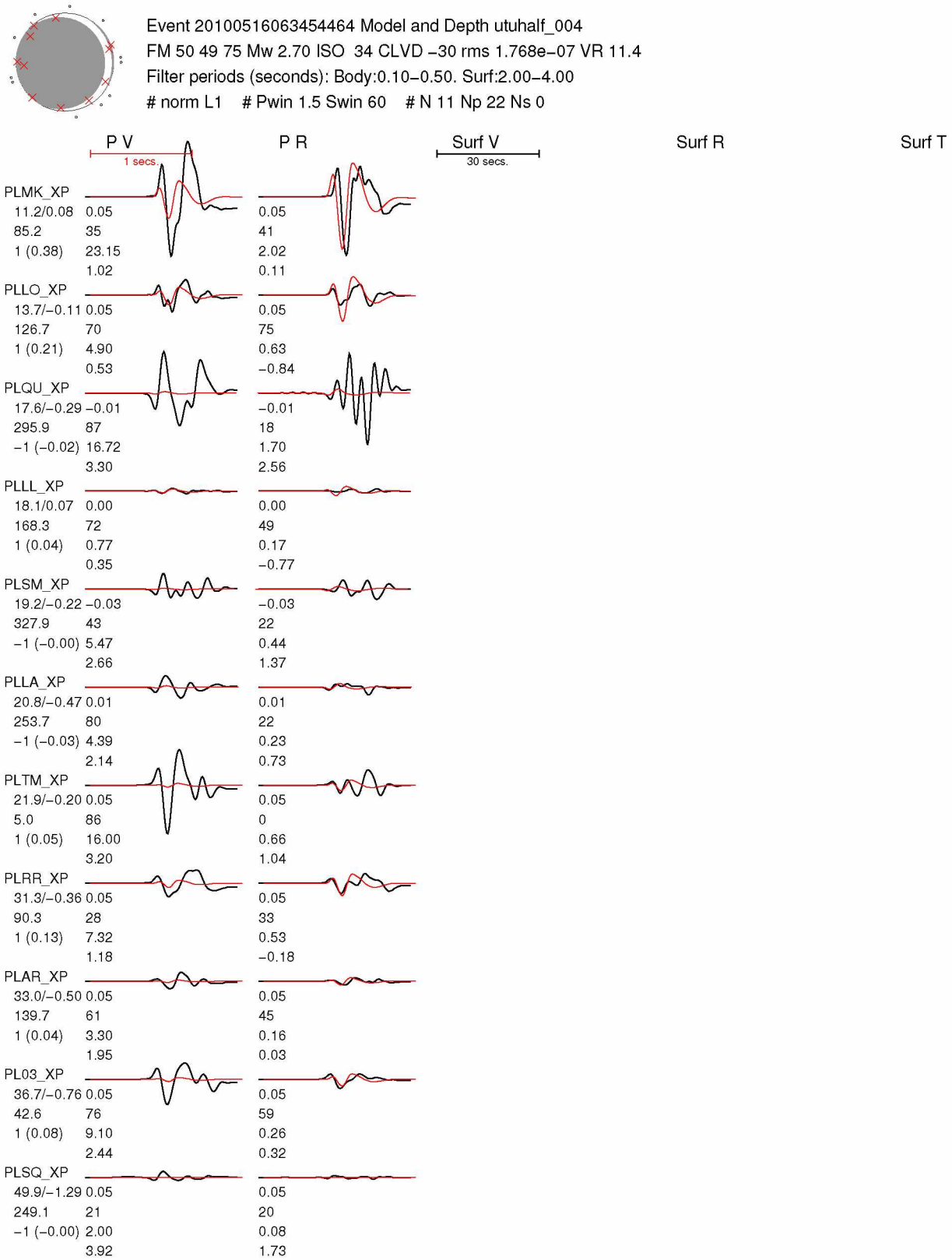

Figure A.22: Waveform fits for the example event, weights V10 R01 S00, tensile crack ($\gamma = -30^\circ$). Misfit summary in Figure A.24c. See summary in Table 2.3.

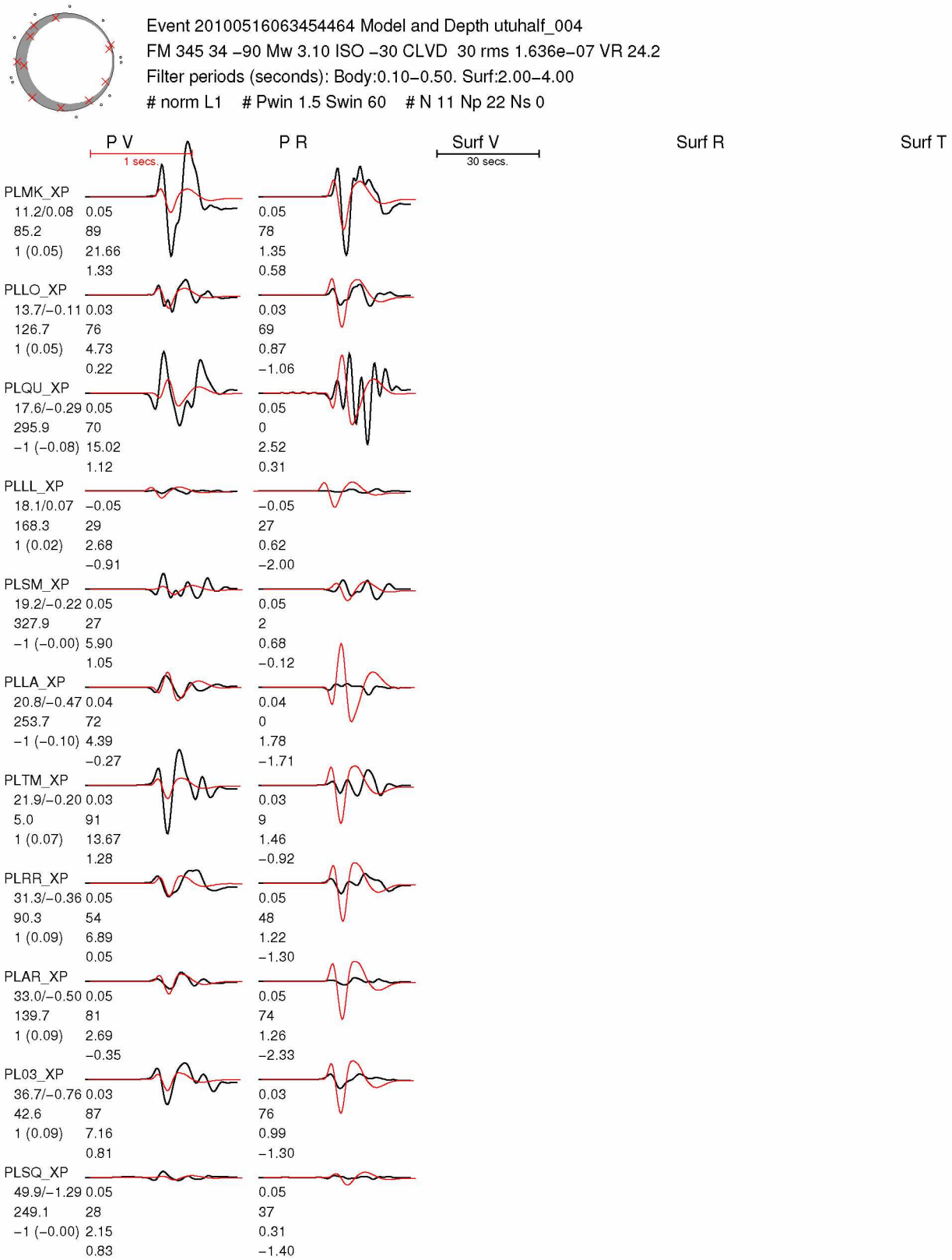

Figure A.23: Waveform fits for the example event, weights V10 R01 S00, compression crack ($\gamma = 30°$). Misfit summary in Figure A.24d. See summary in Table 2.3.

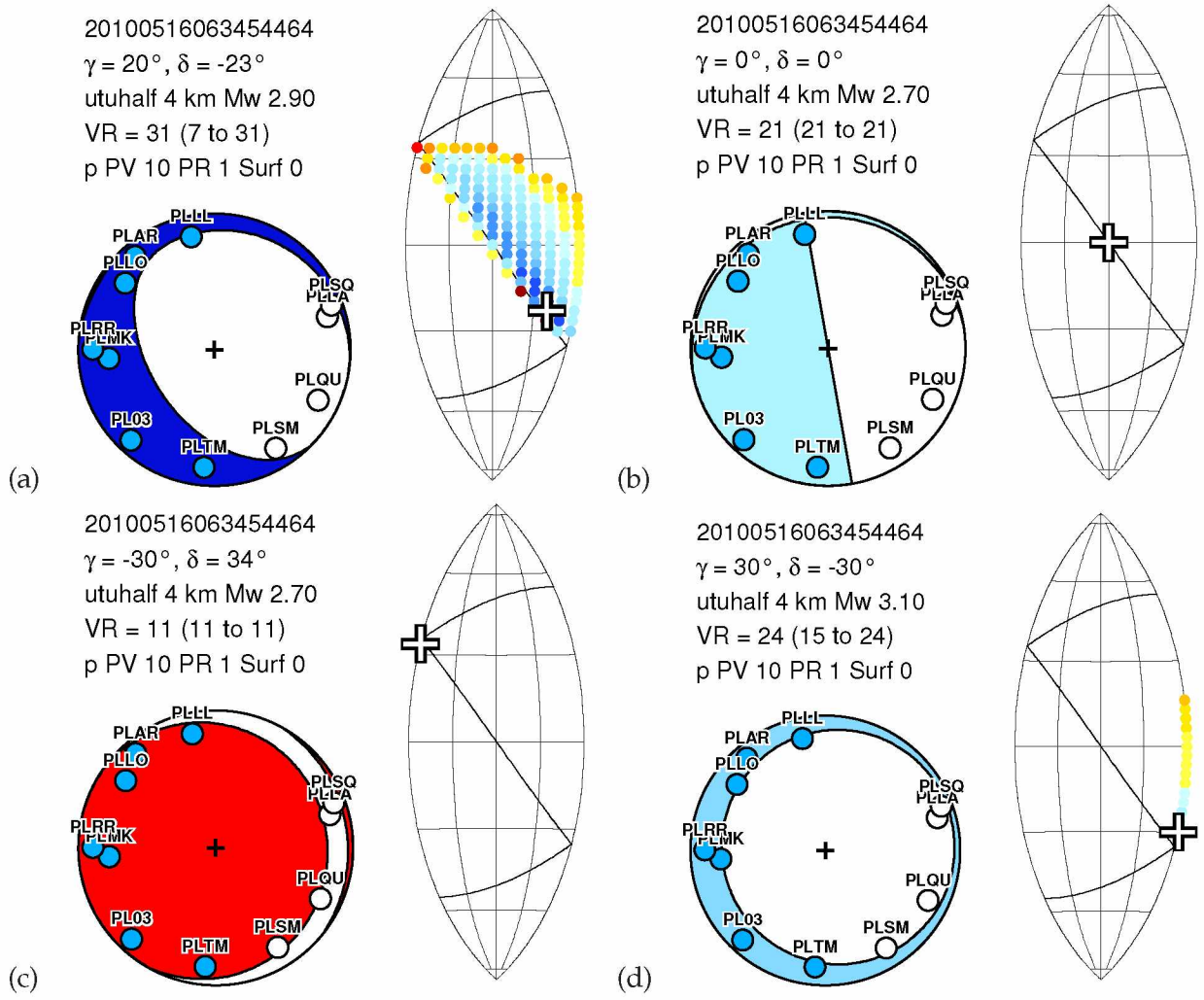

Figure A.24: Best solutions for different physical models represented by subsets of moment tensor space. See summary in Table 2.3. (a) Full moment tensor inversion (same as Figure 2.7c), waveform fits in Figure 2.4. (b) Inversion constrained to shear faulting (double couple: $\gamma = 0°, \delta = 0°$), waveform fits in Figure A.21;. (c) Inversion constrained to tensile crack ($\gamma = -30°$), waveform fits in Figure A.22. (d) Inversion constrained to compression crack ($\gamma = 30°$), waveform fits in Figure A.23.

A.4 References

Aki, K. & Richards, P. G., 1980. *Quantitative Seismology, Theory and Methods*, W. H. Freeman, San Francisco, Calif., USA.

Alvizuri, C., 2015. Seismic moment tensor catalog for Uturuncu volcano, Bolivia, ScholarWorks@UA at http://hdl.handle.net/11122/6266 (last accessed 2016/01/22): descriptor file, text file of catalog, and composite figures of waveform fits and misfit analyses.

Kanamori, H., 1977. The energy release in great earthquakes, *J. Geophys. Res.*, **82**, 2981–2987.

Keyson, L. & West, M. E., 2013. Earthquake sources near Uturuncu Volcano, Abstract V13B-2603 presented at 2013 Fall Meeting, AGU, San Francisco, Calif., 9-13 Dec.

Silver, P. G. & Jordan, T. H., 1982. Optimal estimation of scalar seismic moment, *Geophys. J. R. Astron. Soc.*, **70**, 755–787.

Takemura, S., Furumura, T., & Maeda, T., 2015. Scattering of high-frequency seismic waves caused by irregular surface topography and small-scale velocity inhomogeneity, *Geophys. J. Int.*, **201**, 459–474.

Tape, W. & Tape, C., 2012. A geometric setting for moment tensors, *Geophys. J. Int.*, **190**, 476–498, doi:10.1111/j.1365-246X.2012.05491.x.

Tape, W. & Tape, C., 2015. A uniform parameterization of moment tensors, *Geophys. J. Int.*, **202**, 2074–2081, doi:10.1093/gji/ggv262.

Tarantola, A., 2006. Popper, Bayes and the inverse problem, *Nature Physics*, **2**, 10.1038/nphys375.

Appendix B

Text Supplement for ScholarWorks@UA collection

Seismic moment tensor catalog for Uturuncu volcano, Bolivia

Celso Alvizuri

December 7, 2015

Attribution: If you use these files, please cite Alvizuri & Tape (2016) and Alvizuri (2015).

B.1 Description of files

The files here are part of the PhD thesis work by Celso Alvizuri. This supplement is cited in Alvizuri & Tape (2016).

A seismic moment tensor catalog of 63 events was generated using first-motion polarities, body waves and surface waves. The best solution (M_0) was obtained through a grid-search in the moment tensor space using the 'cut-and-paste' (CAP) approach of Zhu & Helmberger (1996); Zhu & Ben-Zion (2013). Figures are listed in Section B.2. The waveform fits for the 63 events in the catalog are shown in Figure A1. The waveform misfit on the source-type plot for these events are shown in Figure B1.

A second seismic moment tensor catalog for the same 63 events was generated using body waves and surface waves but without first-motion polarities. This second set of figures is listed in Section B.2.

B.2 Inversions using first-motion polarities

B.2.1 Figure A1: Waveform fits (Catalog events)

[File name: `utuhalf_P01_V10_R01_S10_waveform_fits.pdf`]

Waveform fits for 63 moment tensor inversions for which waveform misfit is plotted on the source-type plot. (Figure B). Black are observed waveforms; red are synthetic waveforms computed using a frequency-wavenumber method (Zhu & Rivera, 2002) that assumes a (1D) layered model. We use a homogeneous halfspace model `utuhalf`. The waveforms are fit separately within five time windows: P wave vertical component (PV), P wave radial component (PR), Rayleigh wave vertical component (SurfV), Rayleigh wave horizontal component (SurfR), and Love wave transverse component (SurfT). At far left in each row is the station name, source-station distance in km, and station azimuth in degrees. Below each pair of waveforms are four numbers:

the cross-correlation time shift between data and synthetics, the cross-correlation value, the percent of the misfit function represented by the waveform pair, and the amplitude ratio between waveforms, $\ln(A_{obs}/A_{syn})$, where A is the max value of the waveform within the time window.

The beachball represents the best solution M_0 (i.e., the global minimum of the misfit function). The beachball is plotted as a lower-hemisphere projection (standard seismological convention) of the moment tensor. The surrounding black dots denote the azimuthal location of the stations used, and the red crosses denote the lower hemisphere piercing points of the ray paths to the stations.

Here is a description of the four header lines:

1. `Event 20100516063454464 Model and Depth utuhalf_004`
   The event ID is derived from the origin time of 2010-05-16 06:34:54.464.
   The halfspace model used is `utuhalf`, and the event depth is 4 km.

2. `FM 150 76 -75 Mw 2.80 ISO -10 CLVD 10 rms 1.790e-07 VR 22.1`
   The orientation of the moment tensor solution M_0 is strike 150°, dip 76°, rake −75°. The estimated magnitude is M_w 2.8. The ISOtropic coordinate is $\delta = -10°$ and the CLVD coordinate is $\gamma = 10°$. The waveform difference between data and synthetics is 1.790×10^{-7}, and the variance reduction is $VR = 22.1\%$.

3. `Filter periods (seconds): Body:0.10--0.50. Surf:2.00--4.00`
   The body waves were filtered 0.10–0.50 s, the surface waves were filtered 2.00–4.00 s.

4. `# norm L1 # Pwin 1.5 Swin 60 # N 11 Np 22 Ns 33`
   An L1 norm was used for the misfit function. The (reference) P-window is 1.5 s long, the surface wave window is 60 s long, there are 11 stations with at least one waveform, 22 is the number of P windows used, and 33 is the number of surface wave windows used.

The numbers below each station are

1. source–station epicentral distance, km
2. station azimuth, in degrees
3. sign of the observed first-motion polarity, which is either 1 (up or compression) or −1 (down or dilatation). The number in parentheses is the predicted amplitude, which ranges between $\pm\sqrt{2}$; numbers close to zero indicate that the station is near a nodal surface of the radiation pattern for the assumed mechanism.

The four numbers below each pair of waveforms are

1. the cross-correlation time shift $\Delta T = T_{\text{obs}} - T_{\text{syn}}$ required for matching the synthetics $s(t)$ with the data $u(t)$ (a positive time-shift means that the synthetics arrive earlier than the data)

2. the maximum cross-correlation percentage between $u(t)$ and $s(t - \Delta T)$

3. the percentage of the total misfit

4. the amplitude ratio $\ln(A_{\text{obs}}/A_{\text{syn}})$ in each time window

B.2.2 Figure B1: Summary misfit plots for all 63 events

[File name: `utuhalf_P01_V10_R01_S10_misfit.pdf`]

Alvizuri & Tape (2016), Figure 2.6, caption:

Full moment tensor misfit summary for the example event. For details, see Section 2.4. (a) Map of source location (red star) and stations used in the inversion for this event. The station is colored blue if the observed first-motion polarity on the vertical component is up (compression) and white if it is down (dilatation). (b) Contour plot of the polarity misfit on the lune. Not to be confused with the waveform misfit, the polarity misfit $n(M)$ (Eq. 2.5) for a moment tensor M is the number of stations where the observed first-motion polarity differs from the polarity predicted from M. The polarity misfit $n(\Lambda)$ (Eq. 2.6) at a point Λ on the lune is then the minimum of $n(M)$ for moment tensors M having source type Λ. At each point Λ in the region where $n(\Lambda) = 0$ (blue), there is therefore a moment tensor M with source type Λ that has correct polarities, that is, polarities that match the observed polarities at all 11 stations. (c) Contour plot of the variance reduction $VR(\Lambda)$. The variance reduction $VR(\Lambda)$ at a point Λ is the maximum variance reduction $VR(M)$ for moment tensors M that have source type Λ and that have correct polarities. (Compare Eq. 2.7, which is the analog of $VR(\Lambda)$ for misfit.) Large values (blue) of VR represent better fit between observed and synthetic waveforms. Since M is required to have correct polarities, the plot of $VR(\Lambda)$ is only defined on the region $n(\Lambda) = 0$. The beachball plotted at each point Λ of this region is the moment tensor $M(\Lambda)$ that maximizes $VR(M)$ with Λ fixed. Of the beachballs $M(\Lambda)$, our desired solution M_0 (green box) is the one with largest VR. The gray arcs on the lune are the great circle arcs $\lambda_1 = 0$, $\lambda_2 = 0$, and $\lambda_3 = 0$ (white, green, and red in Figure 2.1). Selected eigenvalue triples (black dots) on the boundary of the lune are indicated, with the understanding that the triples need to be normalized. The positive isotropic source $(1, 1, 1)$ is at the top, the negative isotropic source $(-1, -1, -1)$ is at the bottom, and the double couple $(1, 0, -1)$, not shown, would be at the center of the lune. (d) The moment tensor M_0, the same as in (c) but plotted in a lower-hemisphere projection. For this event, all ray paths travel upward from the source to the stations, so the stations to the east, having upward (compressional) first motions, are plotted on the left of the beachball at the antipode of the ray path direction.

B.2.3 Text file table for moment tensor catalog

[File name: `utuhalf_P01_V10_R01_S10_mecha.txt`]

Seismic moment tensor catalog of 63 events. Details can be found within the header lines, which also refer to Kanamori (1977); Silver & Jordan (1982); Tape & Tape (2012).

B.2.4 Input text files used in the moment tensor inversion

[File name: `weights_utuhalf_P01_V10_R01_S10.zip`]

We provide a text file for each of the 63 events in this study. These files show which stations and which time windows were used (or not) in each moment tensor inversion. It also shows the first-motion polarity observations that were used.

B.3 Inversions without using first-motion polarities

B.3.1 Figure A2: Waveform fits (Catalog events)

[File name: `utuhalf_P00_V10_R01_S10_waveform_fits.pdf`]

Same as in Figure A1 except polarities are not listed under each station label.

B.3.2 Figure B2: Summary misfit plots for all 63 events

[File name: `utuhalf_P00_V10_R01_S10_misfit.pdf`]

Same as in Figure B1 except that since first-motion polarities are not used, there is no $n(\Lambda)$ plotted in (b). Beachballs with $VR < 0$ are considered least likely; we do not plot a beachball at Λ if $VR(\Lambda) < 0$.

B.3.3 Text file table for moment tensor catalog

[File name: `utuhalf_P00_V10_R01_S10_mecha.txt`]

B.3.4 Input text files used in the moment tensor inversion

[File name: `weights_utuhalf_P00_V10_R01_S10.zip`]

B.4 References

Alvizuri, C., 2015. Seismic moment tensor catalog for Uturuncu volcano, Bolivia, ScholarWorks@UA at http://hdl.handle.net/11122/6266 (last accessed 2016/01/22): descriptor file, text file of catalog, and composite figures of waveform fits and misfit analyses.

Alvizuri, C. & Tape, C., 2016. Full moment tensors for small events ($M_w < 3$) at Uturuncu volcano, Bolivia, *Geophys. J. Int.*, **206**, 1761–1783, doi:10.1093/gji/ggw247.

Kanamori, H., 1977. The energy release in great earthquakes, *J. Geophys. Res.*, **82**, 2981–2987.

Silver, P. G. & Jordan, T. H., 1982. Optimal estimation of scalar seismic moment, *Geophys. J. R. Astron. Soc.*, **70**, 755–787.

Tape, W. & Tape, C., 2012. A geometric setting for moment tensors, *Geophys. J. Int.*, **190**, 476–498, doi:10.1111/j.1365-246X.2012.05491.x.

Zhu, L. & Ben-Zion, Y., 2013. Parameterization of general seismic potency and moment tensors for source inversion of seismic waveform data, *Geophys. J. Int.*, **194**, 839–843, doi:10.1093/gji/ggt137.

Zhu, L. & Helmberger, D., 1996. Advancement in source estimation techniques using broadband regional seismograms, *Bull. Seis. Soc. Am.*, **86**(5), 1634–1641.

Zhu, L. & Rivera, L. A., 2002. A note on the dynamic and static displacements from a point source in multilayered media, *Geophys. J. Int.*, **148**, 619–627, doi:10.1046/j.1365-246X.2002.01610.x.